

Optical and Electrical Diagnosis of Atmospheric Pressure Plasma Jets

Andrew Thomas West

Doctor of Philosophy

University of York

Physics

April 2016

Abstract

Radio frequency atmospheric-pressure plasma jets have gained popularity in recent years, both in academia and industry, due to their ability to produce reactive chemical species at relatively cold gas temperatures. Operating at atmospheric-pressure allows for greater scalability than low-pressure plasma discharges, that are confined to operate in a vacuum chamber, offering advantages over current manufacturing techniques. Operation at atmospheric-pressure has also resulted in growing research into use of plasmas for therapeutic applications in biomedicine. Atmospheric-pressure plasma devices are beginning to be certified as medical devices in clinical settings, utilising their efficient production of reactive species in a cold, dry environment.

The underlying mechanisms behind these processes are poorly understood, especially in the highly complex chemical conditions surrounding biomedical applications. Researchers require knowledge of the plasma chemistry to infer what subsequent interactions are taking place. Once a particular mechanism has been established, the plasma chemistry in atmospheric-pressure plasma devices can be tailored and optimised for a particular application. To achieve this, investigators require not only identification of which species are present, but also their concentrations, and how species can be maximised or minimised to yield the best therapeutic effect. Diagnostics are required which can measure reactive species in ambient air, but also identify the underlying plasma dynamics responsible.

To this end, novel picosecond two-photon absorption laser induced fluorescence is implemented, allowing for the first time, spatially resolved measurement of plasma produced atomic species in ambient air. Production of atomic nitrogen and atomic oxygen is linked to various plasma parameters such as: molecular admixture, voltage, and operating frequency. A new methodology for measuring plasma power in small radio frequency atmospheric-pressure plasma devices is presented, and has allowed for better understanding of the plasma dynamics. This has identified how reactive species can be maximised through increased plasma electron density, but also how they can be produced most efficiently. Furthermore, this methodology has allowed for the confirmation of different operating modes inside the plasma, in agreement with phase resolved optical emission spectroscopy. With the knowledge gained from how plasma dynamics and plasma chemistry changes with input parameter variations, it has been possible to identify key reactive species in industrial scenarios, such as the case study of photoresist removal at atmospheric-pressure.

Contents

Abstract	2
Contents	3
List of Tables	6
List of Figures	7
Acknowledgements	10
Declaration	11
1 Introduction	12
1.1 Motivation	12
1.2 Thesis Outline	14
2 Fundamentals of Plasmas and the μ-APPJ	15
2.1 What is a Plasma?	15
2.1.1 Quasi-neutrality	15
2.1.2 Debye length	16
2.1.3 Plasma parameter	16
2.2 Plasma Frequency	18
2.3 Radio Frequency Plasmas	19
2.3.1 Atmospheric pressure plasma jets	21
2.4 The micro-Atmospheric Pressure Plasma Jet	22
2.4.1 EU COST reference microplasma jet	26
3 Two-Photon Absorption Laser Induced Fluorescence of Atomic Nitrogen	27
3.1 Why use laser fluorescence?	28
3.2 Two-Photon Absorption Laser Induced Fluorescence	29
3.2.1 Excitation	30
3.2.2 De-excitation	31

3.2.3	Fluorescence Detection	34
3.2.4	Calibration	35
3.3	Considerations for atmospheric TALIF	36
3.4	Experimental procedure	37
3.4.1	Excitation schemes	40
3.4.2	Measuring lifetime and total fluorescence	45
3.5	Error estimation	48
3.5.1	Quantum efficiency and optical transmission	48
3.5.2	Natural lifetime, branching ratio, and two-photon absorption excitation cross section	49
3.5.3	Stochastic errors	49
3.5.4	Total error estimation	52
3.6	Results	53
3.6.1	Variation in N ₂ admixture	53
3.6.2	Variation in applied voltage	54
3.6.3	Comparison of measured lifetimes to predicted values	55
3.6.4	Atomic nitrogen density in complex chemical environments	56
3.7	Summary	60
4	Measuring Plasma Power and Operating Modes	61
4.1	Measuring power in AC circuits	62
4.1.1	Impedance	63
4.2	Approximating plasmas as circuits	64
4.3	Strategies for measuring plasma power	67
4.3.1	Treatment of phase angle	69
4.4	A method to measure plasma power in the μ -APPJ	70
4.4.1	Plasma on	71
4.4.2	Plasma off	71
4.4.3	Calibration	72
4.4.4	Calculation	73
4.4.5	Error estimation	73
4.4.6	Proof of concept	77
4.4.7	Advantages of measuring phase angle directly	81
4.5	Results	83
4.5.1	Variations in N ₂ and O ₂ admixture	83
4.5.2	Diagnosis of plasma operating modes	85
4.6	Comparison to PROES	89
4.6.1	Sheath dynamics and operating modes	90
4.7	Summary	93

5	Characteristics of the μ-APPJ under driving frequency variation	94
5.1	Power Dissipation	95
5.2	Reactive Species Production	97
5.2.1	Absolute N and O densities	98
5.2.2	Efficiency in reactive species production	100
5.3	Operating modes	101
5.3.1	Comparison to PROES	103
5.4	Summary	106
6	Using the Effluent of the μ-APPJ to Etch Photoresist	107
6.1	Removing photoresist	108
6.1.1	Plasma ashing at atmospheric-pressure	109
6.2	Measuring etching rate of photoresist	109
6.3	Preliminary optimisation	111
6.3.1	Influence of UV emission	112
6.4	Results	113
6.4.1	Etch quality	115
6.5	Reactive species responsible for atmospheric ashing	116
6.5.1	Comparison to low-pressure ashing of photoresist	118
6.6	Summary	118
7	Conclusions	119
	List of References	123

List of Tables

2.1	Properties of typical plasmas	20
2.2	Typical operating parameters of the μ -APPJ	24
3.1	Decay rates for N(3p $^4S_{3/2}$) excited state	42
3.2	Error estimation for TALIF	52

List of Figures

2.1	Electron and ion density in the sheath and bulk plasma	17
2.2	Plasma oscillation as a result of electron perturbation	18
2.3	Paschen curves for common gases	21
2.4	Diagram and photograph of the μ -APPJ	23
3.1	Diagram of three level TALIF processes	29
3.2	Saturation curve for Kr	33
3.3	Schematic of TALIF experiment	38
3.4	Schematic of variable attenuation stage	38
3.5	Photographs of TALIF beamline, jet, and image acquisition	39
3.6	Sample TALIF signals	40
3.7	Spatial calibration of iCCD	41
3.8	Excitation Schemes for atomic nitrogen and krypton	41
3.9	Filter Transmission for N TALIF	42
3.10	Filter Transmission for Kr TALIF	43
3.11	ASE observed during Kr TALIF	44
3.12	Kr TALIF with no ASE	45
3.13	Schematic of moving gate width during TALIF measurements	46
3.14	Comparison of decay rates for a true exponential and a simulated TALIF signal	46
3.15	Secondary TALIF measurement captures the total fluorescence decay	47
3.16	Gaussian fit to TALIF signal as a function of wavelength	51
3.17	Absolute N density with changing N ₂ admixture	53
3.18	Absolute N density with applied voltage	54
3.19	Measured and predicted lifetime of the N(3p ⁴ S _{3/2}) state	55
3.20	Absolute N density with synthetic air admixtures	56
3.21	Density and lifetime measurements in the far effluent region	58
3.22	Axial slice of lifetime and density in the effluent	59
4.1	Sample voltage and current waveforms, identifying amplitude and phase	62
4.2	Argand diagram demonstrating impedance of different components	64

4.3	Plasma and losses described by electrical components	65
4.4	Schematic of power measurement	70
4.5	Photograph of V and I probes	70
4.6	Argand diagram of error in FFT	74
4.7	Example FFT of voltage with the distribution of noise magnitudes	75
4.8	Demonstration of error in phase from an FFT due to uncorrelated noise	77
4.9	Schematic of the Large APPJ	77
4.10	Measured power for plasma on, off, and net plasma power in the Large APPJ	78
4.11	Comparison of separate VI probes to commercial co-located probes	79
4.12	Large APPJ comparison to μ -APPJ	80
4.13	Phase angle for the Large APPJ for plasma on and off cases	81
4.14	Resistance and reactance in the Large APPJ	82
4.15	Plasma power against voltage for different nitrogen admixtures	83
4.16	Plasma power against voltage for different oxygen admixtures	84
4.17	Plasma power and phase angle in the μ -APPJ for 0.5% O ₂ admixture	86
4.18	Resistance and reactance for the μ -APPJ with 0.5% O ₂	87
4.19	Diagram of PROES aquisition	89
4.20	Time integrated emission at 844 nm for a He plasma with 0.5 % O ₂ admixture	90
4.21	PROES images of 844 nm in a He plasma with 0.5 % O ₂ admixture	91
5.1	Plasma power for varying driving frequency for oxygen and nitrogen admixtures	95
5.2	Time-averaged emission at 844 nm for 27.12 MHz and 40.68 MHz	96
5.3	Excitation Schemes for atomic oxygen and xenon	97
5.4	TALIF measurements of nitrogen and oxygen for varying driving frequency	98
5.5	N and O densities against plasma power for varying driving frequency	99
5.6	Number of reactive atomic species produced per Joule for N and O	100
5.7	Plasma Power for helium only with varying frequency	101
5.8	Calculated resistance and reactance for helium only plasma at 27.12 MHz	102
5.9	Calculated resistance and reactance for helium only plasma at 40.68 MHz	103
5.10	Time integrated emission at 706 nm for He only plasma at 27.12 MHz	104
5.11	PROES images of 706 nm in a He plasma 27.12 MHz	105
6.1	The use of photoresist in semiconductor manufacture	108
6.2	Photograph of APPJ etching photoresist from SI wafer sample	110
6.3	Etch rate of photoresist with frequency variation	111
6.4	Optical emission spectra of a 13.56 MHz 0.5 % O ₂ discharge	112
6.5	Etch rate of photoresist with variation in input power	113
6.6	Etch rate of photoresist with varying flow rate	114
6.7	Image of etch area after treatment at 7slm and 13slm	114

6.8	ATR-FTIR absorption spectra for Si wafers after plasma removal	115
6.9	TALIF measurements of relative O density with varying flow rate	117

Acknowledgments

My heartfelt thanks goes to my supervisor Erik Wagenaars. He has been forever patient, supportive, and I do not think there is any other supervisor who is as punctual, or accommodating. Erik, thank you for the opportunity to study in York under your tutelage, and I hope this is not the last time we will work together in our careers.

I must also thank my colleagues Martin Blake and David Shaw for keeping me smiling and appropriately distracted from my work. Sandra Schröter and Jérôme Bredin make up the remainder of team TALIF. It has been a privilege working with you, and I have enjoyed every minute. Andrew Gibson you are the font of all knowledge and a world-class researcher. Adam Hirst, Alex Foote, Apiwat Wijaikhum, Joe Branson, Scott Doyle, Dave Meehan, Frederik Riedel, Sudha Rajendiran, Yury Gorbanev, Angela Privat Maldonado, and the other members of the low temperature plasma group past and present at the YPI, thank you for your advice and support. A special thanks goes to Andrew Hurlbatt, who has been a close friend and writing buddy. I hope we will always be looking out for one another.

The staff and students of the York Plasma Institute have made my time here enjoyable and memorable, thank you to you all. Ellie Tubman, thank you for being a great housemate when I moved to York. Brendan Shanahan and Sophia Henneberg, your company during the final weeks of writing up has been greatly appreciated. My deepest gratitude to Kari Niemi and Richard Armitage for their skill and expertise in the lab. Chris Bowman, to the man who showed me the light of Bayes theorem, thank you for your advice and many interesting conversations. The Games Night Crew also deserve a very special mention, Jarrod Leddy, Gaby Leddy, James Davey, Kirsty Davey, and David Blackman. Thank you for what I am sure will be lifelong friendship and understanding - Good Hustle Blues!

The PhD couldn't have been physically possible without the 2341 cups of coffee consumed.

Finally, my greatest thanks goes to Kristie. You have supported me emotionally, cheering me on throughout this journey, and helped pick me up when I fell down. You have sacrificed so many things to allow me to fulfil this dream, and for that I am forever in your debt.

To all of you I say, thank you for believing in me.

Declaration

This thesis has not previously been accepted for any degree and is not being concurrently submitted in candidature for any degree other than Doctor of Philosophy of the University of York. This thesis is the result of my own investigations, except where otherwise stated. All other sources are acknowledged by explicit references.

Chapter 6 contains data collected in collaboration with Marc van der Schans of Department of Applied Physics, Eindhoven University of Technology, Eindhoven, The Netherlands. The results have been published in the article A. West, M. van der Schans, C. Xu, M. Cooke, and E. Wagenaars. Fast, downstream removal of photoresist using reactive oxygen species from the effluent of an atmospheric pressure plasma jet. *Plasma Sources Science and Technology*, 25(2):02LT01, 2016.

Chapter 1

Introduction

1.1 Motivation

Many of the modern technologies we take for granted in our everyday lives are made possible because of plasmas. However plasmas have shaped humanity for billions of years, perhaps most importantly our sun, which has been driving the solar system long before we as a species began to directly harness the most abundant form of matter in the observable universe. The spectacular aurora, formed in the upper atmosphere, has captivated human beings for millennia, but using the plasma of the ionosphere to realise over-the-horizon radio communication is one of the earliest examples of how plasmas have enabled the modern age. Plasmas are used for lighting, manufacturing, sterilisation, entertainment, and much more. In modern nano-fabrication of semiconductor materials, an estimated one third of all manufacturing steps are performed using plasmas [1].

In recent years there has been growing interest in utilising plasmas at atmospheric-pressure for industrial processing and biomedical treatments. Non-thermal atmospheric-pressure plasmas are an efficient source of dry reactive chemistry, however do not suffer from the common restrictions that are associated with operating plasmas at low-pressure such as scalability. Determining this crucial plasma chemistry in collisional ambient air presents a challenge because of greater interaction with unknown chemical species, unlike the controlled environments in more established low-pressure systems. Presently, the plasma dynamics and plasma chemistry when operating plasmas in open air are poorly understood. Current and future devices for new and existing applications rely on characterisation of this chemistry to understand the underlying treatment processes, but also require knowledge of the fundamental plasma dynamics to design, control, and optimise devices for specific roles.

Currently, measurement of plasma produced reactive species has been confined to the core plasma [2], or in unrealistic carefully controlled environments [3,4]. At the application side, measurements have been made at target sites, such as in liquids [5] or the response of cells *in vitro* [6]. Research into chemistry linking these two regions is sparse, and reactive

species interacting with ambient air before reaching a target offers opportunity for modification of the chemistry that could help or hinder the ultimate processing goal. To tailor applications, techniques are required to gain more information about this crucial region in ambient atmospheric plasma-surface interactions.

This work aims to address the requirement to measure complex plasma chemistry in open atmosphere. Moreover, it examines how input parameters such as power and frequency effect the plasma dynamics and ultimately plasma chemistry. Previously, nanosecond pulse laser induced fluorescence has been utilised to measure atomic species at atmosphere pressure. Due to the length of the laser pulse, assumptions about the chemistry conditions are required to estimate reactive species densities. These assumptions have large errors, and quickly breakdown outside the core plasma or when the plasma gas mixture is complex.

A novel picosecond laser induced fluorescence system has been designed and constructed to perform measurements of atomic species in highly collisional systems, such as those at atmospheric-pressure, to measure reactive atomic species in ambient air. Using a shorter laser pulse length allows for direct measurement of the fluorescence signal decay, which removes the need for the assumptions typically made with nanosecond pulse laser systems. Never before has it been possible to measure atomic species densities accurately in the chemically complex region between the core plasma and a target site.

Lack of estimations of plasma power is a known barrier for fundamental research in the atmospheric-pressure plasma community [7–9]. It inhibits true comparison and benchmarking between different devices, experiments, and modelling. Plasma power can also reveal information about the electron dynamics and how factors such as density and temperature may be affected by different operating parameters. Changing the electron density and temperature has been sought after as a means with which to control plasma chemistry [10].

Estimation of plasma power in small atmospheric-pressure radio frequency capacitively coupled discharges is very sensitive to measurement conditions, as the fraction of power in the plasma is smaller than the power lost into other systems. Existing techniques either only work in very niche operating conditions [11], or rely on assumptions that may mask the true plasma behaviour [12]. New procedures of best practice are proposed and tested for measuring power in small radio frequency atmospheric-pressure plasmas to enable more accurate and reliable estimations of plasma power.

To highlight the benefits gained from the investigations performed in this thesis, a case study is undertaken to optimise the removal of photoresist, a common plasma process. This case study explicitly demonstrates how proper measurement of reactive species densities, with respect to operating parameters, can ultimately achieve the highest processing speeds found for chemical only removal of photoresist. Future practitioners wanting to develop reactive species sources will be able to utilise the observations and conclusions of this work.

1.2 Thesis Outline

This thesis is set out in the following manner:

Chapter 2 provides an overview of the atmospheric-pressure plasma device used in this study, including basic plasma theory.

Chapter 3 investigates the measurement of atomic nitrogen using picosecond laser absorption and monitoring fluorescence. These measurements are undertaken for various operating parameters, and a comparison is drawn to previous investigations. Fundamental theory behind laser induced fluorescence is presented, with details of the experimental design.

Chapter 4 introduces the concept of measuring plasma power and limitations that are present for different approaches. By considering the possible error, a method is proposed that can minimise and appropriately report error in measurement of plasma power. The methodology is then implemented to offer more information about the underlying plasma dynamics, through use of a simple circuit approximation.

Chapter 5 compares measurement of reactive species and plasma power across different driving frequencies of the plasma device. Relationships between plasma dynamics and plasma chemistry are drawn. Furthermore, previously unobserved operating modes in the plasma device are investigated at these different frequencies.

Chapter 6 offers an example of how the industrial application of removing photoresist at atmospheric-pressure can be understood, and tailored, with the knowledge gained from the previous chapters.

Chapter 7 summarises the key conclusions from this study, and presents an outlook for future investigations.

Chapter 2

Fundamentals of Plasmas and the Micro Atmospheric Pressure Plasma Jet

2.1 What is a Plasma?

Changes of state occur with the addition of energy into a system, this is how a solid can become a liquid, to a gas, and if the energy input is increased, eventually the electrons will begin to detach from their parent nucleus. This ionisation forms a soup of ions and electrons, which can respond to electromagnetic fields that are applied unlike ordinary neutral gas. Plasmas are an ionised gas, however not all ionised gases are plasmas. The formal definition requires three criteria to be met for an ionised gas to be classed as a plasma, the so-called “Fourth state of matter” [13].

2.1.1 Quasi-neutrality

Firstly and most importantly, the gas must be “quasi-neutral”. Though the ionised gas is in reality a collection of discrete charges on the microscopic scale, on the macroscopic scale the density of negative charges (n_-) and the density of positive charges (n_+) must balance, resulting in a zero net charge in the system. A second parameter now logically forms as a result of this definition, how big must be system be for it to be classed as quasi-neutral, i.e. can it hide small scale perturbations in charge density, so it is seemingly neutral on the macro-scale?

2.1.2 Debye length

The ‘‘Debye Length’’ is a measure of how large the plasma must be to screen perturbations in charge density [13] and appear charge neutral on a macroscopic scale. Consider a quasi-neutral plasma where the electrons, due to their small mass are very mobile, whereas the heavy ions are sluggish, and barely react to external forces compared to electrons. A point source of positive charge is lowered into the plasma, and the electrons are attracted towards it through the Coulomb force which is proportional to $1/r^2$. A cloud of electrons surround the charge, screening it from the rest of the plasma. The electrons are not entirely at the mercy of the electrostatic potential, as their thermal motion can counteract it. At the edge of the electron cloud, where the positive charge is mostly screened by the other electrons, some electrons have enough thermal energy to resist the already weak electrostatic force. Consequently, the charge is not as efficiently screened, and an observer needs to be at a further distance away to no longer perceive the perturbation. This distance is known as the Debye length, λ_D , given as:

$$\lambda_D = \sqrt{\frac{\epsilon_0 k_B T_e}{n_e e^2}} \quad (2.1)$$

As the electrons are far more mobile, the ions can be approximated as static and only the electron temperature (T_e) and the electron number density (n_e) are considered. As ions and electrons have the same charge, e is merely the fundamental electron charge. The permittivity of free space (ϵ_0) and the Boltzmann constant (k_B) are as expected. The Debye length shows that the more energy the electrons have, $k_B T_e$, the larger the plasma must be to screen charges. Conversely, if there are more charge carriers (n_e is greater), then the more effective the plasma is at screening charge, and the Debye scale is smaller.

2.1.3 Plasma parameter

Finally there is the ‘‘Plasma Parameter’’; the number of charge carriers inside the Debye sphere that are available to screen charge. The plasma parameter gives an indication of whether a plasma is dominated by electrostatic forces, or by traditional collisional kinetics. The plasma parameter is a function of the charge carrier density, approximated as the electron density n_e , and the Debye length λ_D :

$$N_D = \frac{4\pi}{3} n_e \lambda_D^3 \quad (2.2)$$

In the case that $N_D \gg 1$, collisional kinetics are larger than electrostatic forces, and the plasma can be approximated as an ideal gas (treated statistically like a fluid [14]). This also means that the plasma can effectively screen charge, which is fundamental for maintaining quasi-neutrality.

2.1.3.1 Sheaths

When introducing the concept of the Debye sphere, the condition of quasineutrality was broken near where the positive potential was introduced. Considering ions and electrons with the same temperature $T_e = T_i$ in a finite volume of quasineutral plasma contained in a box of scale length many times greater than the Debye length. Due to their smaller mass, and therefore larger thermal velocity, electrons are able to leave the system faster than ions to the walls of the box, leaving a net positive charge behind near the edge of the plasma. The region of net positive charge compared to the grounded wall results in a potential gradient, and as electrons enter this region from the bulk plasma, they are repelled back into the centre. The resultant effect of this imbalance of charge, as shown in Figure 2.1, is that a region forms with very small electron density, and a clear departure from quasineutrality of the plasma bulk.

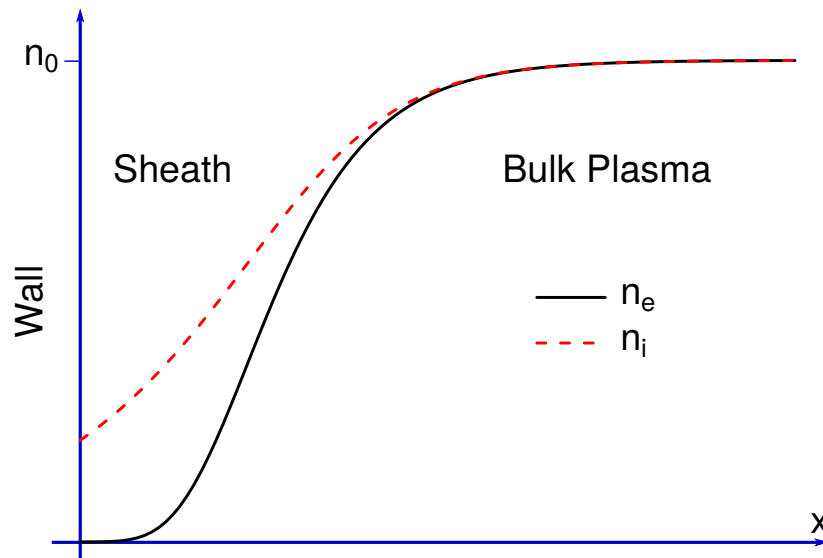


Figure 2.1: Electron density n_e , and ion density n_i as a function of position from a wall interface to the plasma centre of density n_0 . In the bulk plasma, quasineutrality is held. When entering the sheath region, there are fewer electrons, and quasineutrality is no longer held.

This region is known as the sheath. An equilibrium for sheath formation is found when the ion current and electron current to the wall is equal, and therefore no net change in charge in the system occurs. There are many definitions of where the bulk ends and the sheath begins, however a common definition is the position where the integrated electron density from the wall towards the centre is equal to the integrated net charge density from the centre outwards [15]. As a general rule, the sheath is roughly ten times greater than the Debye length [1].

2.2 Plasma Frequency

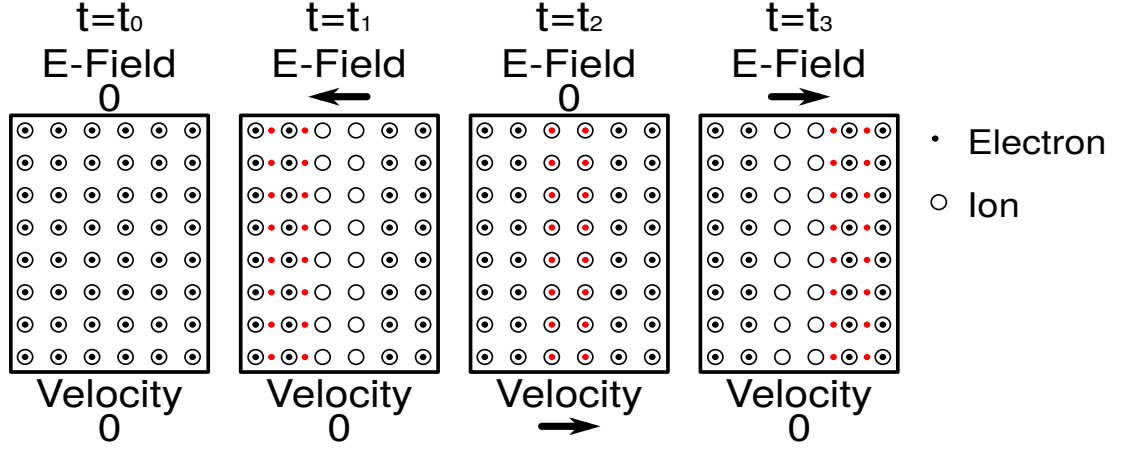


Figure 2.2: Plasma inside each rectangle is quasi-neutral, and at $t = t_0$ the plasma is static. If some electrons (red) are displaced in a particular region of space at $t = t_1$, this invokes an electric field that draws the electrons back to the centre. At $t = t_2$ the electrons have returned to the static position and there is no longer a charge imbalance. However the electrons have sufficient kinetic energy imparted by the electric field that they continue past this point and overshoot, resulting in a new but opposite electric field at $t = t_3$ and cycle repeats. The rate of this oscillation is the plasma frequency.

As mentioned previously, the ions in a plasma are usually thought of as slow moving compared to electrons due to their greater mass. Consider a plasma with uniform charge density, then instantaneously all the electrons are displaced, leaving two adjacent regions of positive and negative charge. The electrons rush to meet the ions due to the electric field, but as they pass, their momentum means they overshoot. The electrons are now displaced on the opposite side, and the electric field now set up in the opposite direction pulls them back the way they came, again overshooting. This oscillating movement continues indefinitely if there are no dampening processes. This oscillation has a characteristic frequency known as the “Plasma Frequency” in rad s^{-1} . This phenomena is demonstrated in Figure 2.2. The plasma frequency indicates how quickly the plasma can respond to external electric fields. Moreover, different species have different oscillating frequencies.

$$\omega_p = \sqrt{\frac{n_e e^2}{m \epsilon_0}} \quad (2.3)$$

Plasma frequency, as shown in Equation 2.3 is a function of the species density (in most cases the ion density is equal to the electron density, hence the use of n_e), and the mass, m . This results in the ions and electrons having different plasma frequencies, with heavier species having lower plasma frequencies. The plasma frequency for a given species is usually denoted with a subscript, for example, the electron plasma frequency is given as ω_{pe} .

If an external electric field oscillates faster than the frequency of a particular species, then the charges simply can not keep up, and are not greatly effected. Conversely, if an external oscillating electric field is slower than the plasma frequency for a given species, then the charges can easily respond [16].

2.3 Radio Frequency Plasmas

Maintaining a plasma using Radio Frequency (RF), means there is the ability to selectively act upon electrons with their high plasma frequency, whereas the ions are too slow to react and stay relatively immobile [16]. Researchers in plasma physics often use the term RF as a synonym for the High Frequency (HF) portion of the RF range, defined as frequencies between 3 MHz to 30 MHz [17]. The energy imparted to the electrons from the oscillating electric field means their energy is much higher than that of the ions, which in turn have more energy than the neutral gas, because they are still imparted some energy from the oscillating electric field.

The energy these species have is usually referred to as the temperature, therefore this can be expressed as ($T_g < T_i \ll T_e$), where T_g refers to the background gas temperature. As the electron temperature is on the order of 30 000 K compared to the ions and neutral at around room temperature (300 K), the electron temperature is typically expressed in electronvolts, eV, where $1 \text{ eV} \sim 11\,600 \text{ K}$. This disparity in the temperatures of the neutral gas, ions and electrons leads to the term ‘non-thermal plasmas’, as the plasma species are not in thermal equilibrium with each other. This characteristic low neutral gas temperature in non-thermal equilibrium plasmas means they are sometimes labelled as ‘cold’ or ‘low-temperature’ plasmas (note that not all low temperature plasmas are radio frequency driven, nor are all radio frequency plasmas low-temperature [7, 18, 19]).

Radio frequency non-thermal plasmas are sought after for their efficient production of reactive chemistry while maintaining low gas temperatures. Electrons in the plasma have sufficient energy that during impact with neutral species they can cause processes such as dissociation. This electron impact is what drives the plasma chemistry, and unsurprisingly is connected to the electron density as well as the electron energy distribution function (EEDF). An RF plasma will usually operate with a noble gas to aid in plasma break down, with a given percentage of admixed precursor gas. A fraction of the gas mixture will be ionised to form the plasma, and the neutral species can dissociate to form chemical products that continue to react to form other reactive species of interest. Though the ratio of charged species density to neutral gas density is small at around 10^{-6} (referred to as the ionisation fraction) the electrons are still able to adequately produce concentrations of reactive species (10^{19} m^{-3} to 10^{22} m^{-3}).

Gases such as O_2 , N_2 , CF_4 , SF_6 , are often mixed into these plasmas as a precursor, which are subsequently broken down into more reactive components. Fluorine (from CF_4 and SF_6) is an obvious example of a highly reactive species that is commonly utilised during low-pressure etching [20, 21]. Atomic oxygen and nitrogen have found uses not only in low-pressure industrial processes, but also at higher pressure. Reactive Oxygen Nitrogen Species (RONS) have been implicated in many applications, most markedly in biomedical applications. As radio frequency plasmas can produce radical chemistry at low gas temperatures required when working with biological material, they have been rapidly established as a prospective complimentary treatment.

The motivation behind using plasmas as reactive chemistry sources is to remove the need for traditional wet chemistry. The incentive may be logistical, where the transport, disposal, and environmental impact of some wet chemicals may be a burden, or for some applications the use of plasmas is superior to traditional wet chemistry. The archetypal example of this comes from low-pressure etching of semiconductor materials. The plasma chemistry and the plasma surface interaction itself produces a synergy [22], resulting in tunable fast anisotropic etching of semiconductor substrates, enabling the rapid rate of innovation in semiconductor technologies [20].

Table 2.1 offers a comparison between different plasmas (such as those for semiconductor manufacturing) and their characteristic electron density (n_e), electron temperature (T_e), Debye length (λ_D), plasma parameter (N_D), and electron plasma frequency (ω_{pe}).

Plasma	n_e (m^{-3})	T_e (eV)	λ_D (m)	N_D	ω_{pe} ($rad\ s^{-1}$)	Ref.
Solar Corona	10^{12}	10^2	10^{-1}	10^9	10^7	[14]
Ionosphere (F-layer)	10^{11}	10^{-1}	10^{-3}	10^4	10^7	[23]
Semiconductor Manufacture	10^{17}	10	10^{-6}	10^3	10^{10}	[1]
Thermal Plasma Cutter	10^{24}	1	10^{-8}	10	10^{14}	[19]
Tokamak Fusion (Core)	10^{20}	10^5	10^{-5}	10^6	10^{12}	[24]

Table 2.1: Properties of typical plasmas.

Radio frequency plasmas are considered ideal plasmas, whereas some plasmas, for example thermal plasmas used for cutting sheet materials, border on being classed as ideal plasmas due to their small plasma parameter. Despite this disparity, these two classes of plasma share similar electron temperatures. RF plasmas share similar Debye lengths to those found in magnetically confined fusion, but the high temperature in fusion devices that would result in a larger Debye length is offset by the greater plasma density. Each plasma, naturally occurring or man-made, is distinct and behaves on its own spatiotemporal scale.

2.3.1 Atmospheric pressure plasma jets

Atmospheric Pressure Plasma Jets (APPJs) are a particular class of plasma device, not surprisingly named after their ability to operate at atmospheric-pressure. Plasmas at high pressure are strongly restricted in size due to the ability to breakdown gases at elevated pressures. Figure 2.3 demonstrates how the breakdown voltage for a gas is a function of the pressure length product, pd , according to Paschen's law. To maintain a similar reasonable breakdown voltage used at low-pressure for an electrode gap on the order of cm [25], at elevated pressures a smaller interelectrode distance is required on the order of mm. The length scale of the plasma must be large enough however to still maintain quasi-neutrality, with a length scale much greater than that of the Debye length.

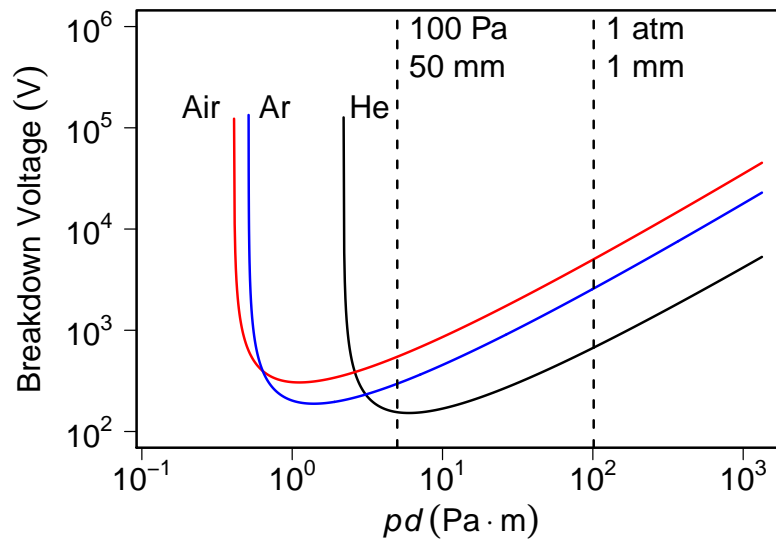


Figure 2.3: Breakdown voltage as a function of the pressure-length product (pd) for helium, argon, and air. Highlighted by vertical dashed lines is the pressure-length product for a device at atmospheric-pressure and an electrode spacing of 1 mm, compared to a low-pressure 100 Pa device with a 50 mm electrode spacing. Values taken from [26].

The first example of an RF atmospheric-pressure plasma jet was reported in 1998 [27,28] for the application of etching (though DC atmospheric-pressure plasma devices had been demonstrated before this [7]). By operating at atmospheric-pressure, many of the issues associated with low-pressure systems can be avoided. Firstly, there is no costly vacuum equipment to install or operate. Secondly, the restrictions on size that come with using vacuum equipment can be mitigated, as the larger the working volume the more costly in terms of time and resources it becomes to operate [20]. Working at atmospheric-pressure allows the plasma to be easily scaled to larger working areas, something of interest to Selwyn and Hicks in 1998 [27,28].

This scalability has allowed for plasma treatment of large areas, such as flat panel displays [29,30], and almost continuous treatment utilising roll-to-roll treatment of polymers, fabrics, and even solar cells [31,32]. Many applications have instead embraced the small size of these devices to provide more focal treatment of substrates at atmospheric-pressure. These smaller devices have found roles in deposition [33,34], etching [28,35], treatment of biofilms [36], treatment of cancer [8,37,38], and wound healing [39,40] to name but a few applications.

2.4 The micro-Atmospheric Pressure Plasma Jet

The recent review by Winter *et al.* [7] discusses the various designs of atmospheric-pressure plasma jets, and the nomenclature surrounding them. A subset of these APPJs are the ‘micro’-APPJ or μ -APPJ because of their small size. The particular design shown in Figure 2.4a, and the focus of this work, is based on the designs of Schulz-von der Gathen *et al.* [41,42]. Primarily it is designed to offer good optical access to the plasma core, allowing measurement of phenomena while remaining compact, and does not require active cooling.

The parallel symmetrical electrodes are bare stainless steel, separated by 1 mm, and 1 mm thick. The gap between the electrodes is enclosed between two quartz windows, producing a square cross section of metal electrodes and quartz walls, offering excellent optical access from the infrared through to the ultraviolet (UV) portion of the electromagnetic spectrum. Working gas consisting mainly of helium is fed in through stainless steel and some short flexible pipework to the rear of the device at a rate on the order of litres per minute, regulated using mass flow controllers. The gas is driven into a plasma using RF voltages from a fixed frequency RF generator, coupled into the device electrodes via a matching network, and a short length of RG58 ($50\ \Omega$ impedance) cable as shown in Figure 2.4b. The shielding of the coaxial cables are used as the ground termination for the device.

The plasma volume is $1\ \text{mm} \times 1\ \text{mm}$ in cross section, and a length of 30 mm as shown in Figure 2.4a. The electrodes and windows are held in place with a PEEK plastic housing, and whole device can fit comfortably in the palm of the hand, and is easily mounted using mounts typically used for optics. Plasma diagnostics for this device rely mainly on optical techniques, since the small dimensions of the plasma channel prevent the use of physical probes, as they would introduce an unacceptable disturbance in the plasma. This is compounded with the difficulties of probe theory in collisional systems, hence the design considerations rely on optical diagnostics.

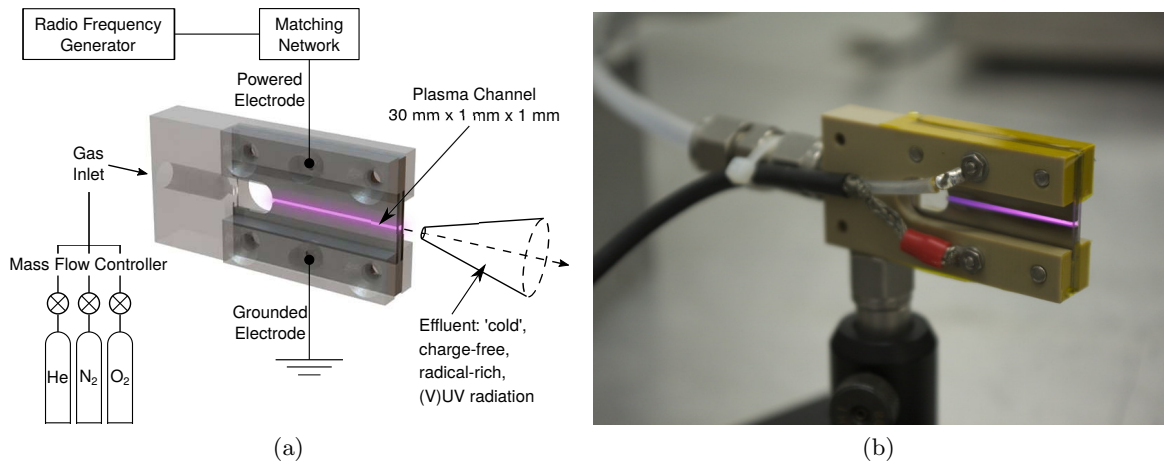


Figure 2.4: (a) Diagram of the μ -APPJ. (b) Photograph of the μ -APPJ in operation.

According to Winter *et al.* [7] the μ -APPJ would be classed as a cross field device, i.e. the electric field between the parallel electrodes is perpendicular to the gas flow. This has consequences on how the device interacts with substrates after the gas exits the plasma channel. A cross field design results in the plasma promptly recombining at the exit of the plasma channel (on the order of microseconds [43]), leaving only neutral species. This region after the plasma channel has many names such as: plasma effluent, plasma plume, plasma flame, and afterglow. In linear or parallel field jets where the electric field is parallel to the gas flow, the active plasma often extends (in some cases, centimetres in length [44]) beyond the plasma channel into open air towards the substrate, sometimes bridging the two by using the substrate as a grounding point for the core plasma. In these conditions there is clear optical emission from the plasma in this open air regime and is often referred to as the afterglow [7]. Other terms such as plasma flame or plasma plume are used for this active plasma that extends beyond the core discharge and often interacts with a substrate. For the cross field μ -APPJ device, this region does not contain a plasma, and is referred to as the plasma effluent [3, 45–49]. It can be seen in Figure 2.4b that no visible emission can be seen after the exit of the plasma channel, however UV and VUV radiation are still able to propagate from the plasma core due to the flow of helium leaving the device. This lack of an active plasma effluent results in the μ -APPJ being able to supply reactive species without charged plasma species interacting with a substrate, for example forming a sheath at the surface which can lead to unwanted ion bombardment. Table 2.2 highlights the normal operating conditions for the μ -APPJ.

The μ -APPJ is operated in a non-thermal homogeneous glow mode [41, 42] and considered a “cold” device because the neutral gas temperature is considerably lower than that of the other plasma species, typically below 100 °C [12]. For some applications, the gas temperature of the effluent must be low enough to maintain the integrity of the substrate. Treatment of

Parameter	Typical value
Voltage amplitude	200 V to 500 V
Frequency	13.56 MHz
Helium flow rate	1 slm
Molecular admixture	$\leq 1\%$
Gas temperature	$< 100\text{ }^\circ\text{C}^*$

Table 2.2: Typical operating parameters of the μ -APPJ. * gas temperature is regulated to be lower during temperature sensitive applications.

plastics which may soften or melt, or treatment of biological material are two examples of substrates that are negatively effected by high temperatures, and therefore power from the RF generator is typically limited to an empirically determined value to avoid this.

The μ -APPJ provides a unique combination of radical chemical species, without plasma interaction at the treatment surface, a gas temperature comparable to that of ambient room temperature, and a simple geometry. The design of bare electrodes driving the plasma allows for simpler modelling, rather than say a Dielectric Barrier Discharge (DBD) device where the electrodes have an intermediate dielectric material between them and the plasma channel. The quartz windows allow for superior optical access of the plasma channel, with the rectangular plasma channel also being more convenient to model than say previous cylindrically symmetric discharges. These characteristics are desirable for both applications and understanding the underlying plasma physics of the μ -APPJ [41, 42].

The operating frequency of 13.56 MHz is designated by the International Telecommunications Union (ITU) as an open (non-licensed) frequency available for use with industrial, scientific or medical purposes (referred to as ISM bands). This non-licensed region also covers the harmonics of 13.56 MHz, including 2.45 GHz used for microwave ovens and WiFi routers. The second and third harmonic (27.12 MHz and 40.68 MHz respectively) are also ISM bands as set out by the ITU under Radio Regulation 5.150 [50].

The μ -APPJ (along with most RF plasma reactors) resembles a capacitor in its design, two parallel plates separated by a gap. This poses a problem for radio frequency generators which are designed to couple into a purely resistive $50\ \Omega$ load to give the optimum power transfer [51]. For a generator to operate effectively to power the plasma device, the capacitive load of the jet must be offset to appear to the generator as $50\ \Omega$. This is achieved by installing an impedance matching network between the generator and the load, which presents the RF generator with a load near to $50\ \Omega$. This need for impedance matching is a problem for nearly all RF plasma devices, and even in traditional radio systems in general. Impedance matching also avoids power being reflected at a load mis-match back to the RF generator and possibly causing damage [17, 51].

Continuous radio frequency voltage applied at the electrodes through the matching network from the generator is around 250 V to 500 V in amplitude, high enough to break down the helium gas with any additional molecular species via capacitive coupling. The plasma forms a homogeneous glow discharge that fills the entire plasma channel. If the voltage is increased too much, local thermal instabilities can drive additional ionisation and greater electron densities from that of a normal glow mode [26]. This has a positive feedback effect, where additional electron densities further increase the local gas temperature, and the ionisation increases further. This positive feedback loop results in an arc to form, which can damage the μ -APPJ. This undesired mode is referred to as an arcing or constricted mode in the μ -APPJ [42]. Arc plasmas are also associated with high gas temperatures, which are to be avoided when treating thermosensitive substrates.

The gas flow rate of 1 standard litre per minute (slm) results in a residence time of 1.8 ms along the 30 mm channel. Admixtures are usually limited to 1% in the main helium gas, as higher molecular admixtures lead to higher required operating voltages. Eventually at high enough molecular admixture the plasma jet is no longer able to operate in a glow mode at a reasonable driving voltage. For the production of RONS, molecular oxygen and molecular nitrogen are typical admixed gases either exclusively or sometimes in a mix of 1:4 as synthetic air. Water vapour or molecular hydrogen may also be added to form hydrogen containing species.

For the μ -APPJ, expected values of electron density and temperature are on the order of $1 \times 10^{17} \text{ m}^{-3}$ and 2.5 eV respectively. The estimated Debye length using Equation 2.1 is $\sim 30 \mu\text{m}$, meaning that the scale length of the plasma at 1 mm is much greater, and quasi-neutrality is held. Using these values in Equation 2.2, the calculated plasma parameter $\gg 1$, and it can be assumed that the plasma species individually behave as an ideal gas [14].

The electron plasma frequency calculated using Equation 2.3 is 2.8 GHz, whereas the ion plasma frequency for helium ions (atomic mass 4) is 33 MHz. The ion plasma frequency is on the order of the driving frequency (13.56 MHz), and it would appear the assumption that the electrons are selectively heated is no longer held.

The electron-neutral collision frequency at 300 K and atmospheric-pressure (101.3 kPa) is found to be orders of magnitude greater than the plasma frequency ($\nu_m = 10^{12} \text{ Hz}$) [26, 43, 52]. Electron motion is retarded by collisions, becoming no longer oscillatory and the conceptual picture of plasma frequency breaks down. Instead the electrons are considered to perform drift oscillations, at a drift velocity (v_d) given by

$$v_d = \mu_e E = \frac{eE}{m\nu_m} \quad (2.4)$$

where μ_e is referred to as the mobility, e is the fundamental electron charge, ν_m is the electron-neutral collision frequency, m is the electron mass, and E is the electric field. The maximum displacement over one RF period at this drift velocity is three orders of magnitude

smaller than the total electrode spacing. This effect is also present for ions in the plasma as they collide with neutrals (rate of 10^9 Hz) [16, 20]. The mobility for ions is two orders of magnitude smaller than that for the electrons and their associated displacement motion can be ignored [26]. Though the approximations of plasma frequency are no longer held for highly collisional plasmas, the concept that $\omega_{pi} < \omega < \omega_{pe}$ is valid when describing the charged species dynamics in the μ -APPJ.

2.4.1 EU COST reference microplasma jet

The μ -APPJ has undergone some iterations to arrive at the current design, and continues to undergo modifications for various investigations [45, 47]. Part of a multi-institutional collaboration that has formed under the European Cooperation in Science and Technology (EU COST) framework, COST Action MP1101 “Biomedical Applications of Atmospheric Pressure Plasma Technology”, is to deliver a reference atmospheric-pressure plasma device for use in fields such as biomedicine [12]. This APPJ will be mechanically and electrically engineered to offer a user-friendly plasma device for those who do not have a background in plasma physics, allowing investigators to concentrate on applications, confident that the response is shared across identical devices. It will be of a standardised design that is freely available to all, that will be adopted as a reference source for future investigations at many institutions, much like the Gaseous Electronics Conference reference cell for low pressure investigations [53].

As plasma devices approach the general public, such as the already established kINPen medical plasma device for wound healing [40], their design needs to be carefully considered not only for tailoring to applications but also ease of use by practitioners. The main design is centred around the core design of the μ -APPJ, with 1 mm electrode separation, with an electrode area of 1 mm \times 30 mm. It is driven using RF voltages, and supplied with typically 1 slm helium with admixtures of other gases for particular applications.

Operating best practices is another outcome from the COST Action, allowing investigators to easy benchmark results to those from other researchers and institutions effectively. This includes deciding what are the best operating parameters to use as a metric when comparing devices, for example driving voltage, or plasma power, and how adjustments to other parameters such as molecular admixture or driving frequency may change those dependencies. Investigations made of the μ -APPJ already inform the construction and operation of the COST reference microplasma jet [11, 12, 54–56], and this study will contribute to this goal, not only for the COST reference jet, but also future standardised design iterations that may exist.

Chapter 3

Two-Photon Absorption Laser Induced Fluorescence of Atomic Nitrogen

The μ -APPJ offers a test bed to characterise performance in application relevant scenarios, allowing for more accurate modelling of the device chemistry through the use of global chemistry models [57], but also to build a comprehensive picture of how the plasma chemistry is expected to behave. Oxygen based reactive species such as atomic oxygen, singlet delta oxygen, and ozone, have been well investigated through experiments [2,3,38,46–48,58–62] and modelling [43,57,63–66], yet nitrogen species have been somewhat neglected [57,58,67,68].

Atomic nitrogen is an important reactive species for industrial plasma processes such as treatment of polymers [69] to reduce surface energy, but also the production and deposition of nitride compounds [30,70,71] which are important for manufacture of semiconductor components such as light emitting diodes (LEDs) [72,73].

In biomedical applications, atomic nitrogen may act as a precursor to form other compounds. One of these compounds is nitric oxide (NO), which is considered the most important nitrogen based radical species for biomedical use [6,74,75]. Nitric oxide plays a role in signalling [75,76], wound healing [77–79], and cancer treatment [37,80].

Very recently, nitric oxide has been measured in the effluent of the μ -APPJ [4], however, in biological environments additional molecules are formed in the liquid media that surround the biological material, and atomic nitrogen that enters into the liquid media may then be able to form NO and other relevant reactive species. By understanding the characteristics of atomic nitrogen production, researchers can draw correlations between reactive species and biological indicators, as has been the case with atomic oxygen [38]. Identifying N is important in characterising the μ -APPJ, but in biological systems the dose of reactive species can drastically alter how a plasma treatment behaves [8,74]. Hirst *et al.* [44] demonstrate

how during cancer treatment insufficient dose of reactive species can in fact promote cell proliferation, rather than cell death. Clearly for the treatment of prostate cancer this is undesirable, but for wound healing is a desired consequence. In detection of atomic nitrogen, or any relevant chemical species, it is crucial to know the absolute density that reaches a treatment site so that more accurate modelling and experiments can identify causal links between reactive species and application.

For these reasons, a diagnostic is required that can offer spatial resolution of absolute atomic nitrogen density, in the highly collisional environment of the μ -APPJ effluent in open atmospheric conditions.

3.1 Why use laser fluorescence?

To quote Richard Engeln, “All diagnostics are complementary”, and when used together can reveal rich information about a plasma system. There are many techniques to measure reactive species densities in a plasma, each with advantages and disadvantages. The μ APPJ is too small to allow physical probes inside the plasma, leaving optical techniques as the de facto method for determining plasma properties.

There are two main classes of optical diagnostic: *Active*, where the plasma is interacted with to gain knowledge of the system, and *Passive*, where the plasma is not interacted with and existing emissions are collected from outside the system. Within these two classes are two further broad subgroups: *Direct* and *Indirect*. Direct methods can measure quantities directly from the signal detected, whereas Indirect measurements require calibration or comparison against a known source. An ideal diagnostic would be passive and direct, offering no need for calibration and no perturbation of the plasma, but there are always other considerations. These may include needs such spatial resolution, temporal resolution, as well as physical limitations in detection, amongst many other requirements and limitations.

Laser induced fluorescence (LIF) is just one set of optical diagnostics that are active and indirect, but holds advantages over other common diagnostics in that it can spatially resolve ground state densities. Optical Emission Spectroscopy (OES) for comparison, though a passive technique and often very simple to implement, utilises emission from excited states which are only a small fraction of the total population. Without many assumptions it is difficult to use optical emission spectroscopy to obtain absolute densities of ground state species. Typical active absorption spectroscopy techniques can directly measure ground state species by assessing the light they absorb, but these measurements are often line integrated, offering little spatial resolution. Laser induced fluorescence is an absorption technique, but how it exploits the absorption of photons by ground state species is what gives it the possibility for spatial resolution.

In LIF, ground state species are excited using laser photons, and the induced excited state then falls into a lower state, emitting a photon in the visible or infrared (IR) region. The photons emitted, known as fluorescence photons, only come from the region in which the reactive species and laser interact, offering spatial resolution. It is these fluorescence photons which are detected, and subsequently information on species densities can be inferred.

LIF has been used extensively to measure OH (hydroxyl) radicals [81–83] particularly for medical applications, as well as nitric oxide [84].

Unfortunately for atomic species, the photon energy required to make the transition into an excited state can be large enough that the photon is not only in the UV part of the electromagnetic spectrum, but into the Vacuum-UV (VUV) portion of the spectrum. Wavelengths <194 nm are absorbed by atmospheric species such as oxygen and therefore are unsuitable. By using two photons, the energy requirement is halved, and consequently the radiation required is of a long enough wavelength that it is no longer in the VUV range, and is now practical to utilise. Experimental practicality gained in this respect means costs in others. For example the probability of two photons being absorbed is much smaller than that for a single photon, which means greater laser intensities are required to compensate. Despite its sometimes demanding technical requirements, TALIF has been used to measure atomic species such as Cl, F, H, N, and O [2, 59, 85–91].

3.2 Two-Photon Absorption Laser Induced Fluorescence

In Laser Induced Fluorescence, the ground state density of a molecule or atom can be probed by the conceptually simple process of exciting from the ground state to an upper state, and that excited state then decaying to give a fluorescence photon which is subsequently detected. Let us consider a simple three level system in Figure 3.1 to follow the two main steps in LIF: excitation, and de-excitation.

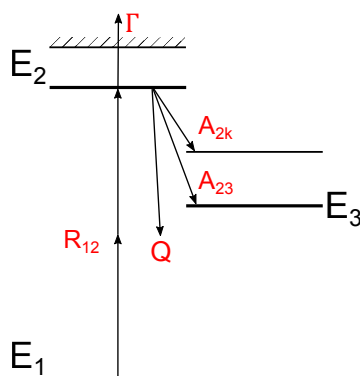


Figure 3.1: Diagram of processes in TALIF. The Ground state E_1 is excited into E_2 using two photons. The excited state E_2 has multiple paths for de-excitation, including radiative decay (A_{2k}), ionisation (Γ), and collisional quenching (Q).

3.2.1 Excitation

First, the atom is excited from the ground state, E_1 , to an excited state E_2 using a laser pulse. Using the weak-field approximation [92], in single photon LIF, the rate of excitation is linearly proportional to laser intensity. However, in TALIF, the excitation rate is proportional to the square of the intensity, as there are two photons which are required to be absorbed. To distinguish two-photon processes from single photon processes, the superscript (2) is used. The rate of this transition in TALIF is given by:

$$R(t) = G^{(2)} \sigma^{(2)} g(\nu) \left(\frac{I_0(t)}{h\nu} \right)^2 \quad (3.1)$$

The so-called photon statistic factor $G^{(2)}$ [93] is 2, twice that of normal LIF. It is a consequence of the increased probability of absorbing off resonance photons which together still match the transition. A treatment of this can be found in [94]. The generalised two-photon excitation cross section, $\sigma^{(2)}$, is the probability of the energy level transition being made. This value is smaller than traditional one photon LIF, and subsequently it must be counteracted using higher laser intensities. This value for TALIF is usually found empirically, rather than relying on approximated values from quantum mechanical models.

The laser intensity I_0 is divided by the photon energy $h\nu$ to give a photon flux, which is squared due to the requirement of two photons to make the transition. The normalised line profile which is a function of frequency, $g(\nu)$, is the convolution of the natural line profile of the transition, which is pressure broadened due to collisions, and Doppler broadened. This broadened line profile also is convoluted with the laser spectral profile. Both the natural line width, and the pressure broadened width are described by Lorentzian distributions. The Doppler broadening and laser line profile are Gaussian in nature, and the result is a Voigt distribution, the convolution of a Gaussian and a Lorentzian. A Voigt profile is similar in shape to a Gaussian, however the tails are more exaggerated.

For very broadband lasers, it can be assumed that this normalised line profile is a Gaussian, as laser width dominates, making fitting much simpler. Usually, the entire normalised profile is scanned over during a measurement, and when integrated reduces to unity.

The excitation rate $R(t)$ is only considered valid if the coherence time of the laser is much less than the time scale of the laser pulse [95]. After the coherence time, it can be assumed that the electric fields of the laser pulse are not in phase, and therefore excitation will be dominated by photon absorption. The coherence time Δt is a function of the bandwidth of the laser [92], which is commonly expressed in wavenumbers ($\tilde{\nu}$), however can also be expressed as wavelength (λ) or frequency (ν) using Equation 3.2.

$$\Delta t = \frac{1}{c\Delta\tilde{\nu}} = \frac{\lambda^2}{c\Delta\lambda} = \frac{1}{\Delta\nu} \quad (3.2)$$

Based on a bandwidth from the manufacturer of $\Delta\tilde{\nu} \sim 4 \text{ cm}^{-1}$, the laser used can be

considered broadband, with a pulse length many times longer than the coherence length. Using this rate equation, it is possible to connect the ground state density to the excited state density.

With state density n , the rate of population into the excited state (E_2) is given by

$$\frac{d}{dt}n_2(t) = R(t)n_1(t) - An_2(t) \quad (3.3)$$

with the excited state density n_2 being populated by the first term, which describes excitation from ground state with density n_1 , and the state being depopulated by the second term on the right hand side at a rate A which will be covered in section 3.2.2.

Consequently the population rate of E_1 will be negative,

$$\frac{d}{dt}n_1(t) = -R(t)n_1(t) \quad (3.4)$$

However, as the ground state density is large, it remains relatively unchanged, and it can be assumed constant, $n_1(t) \sim n_1(0)$. For sake of simplicity, the constant ground state density will be referred to as n_1 . The upper excited state is populated only during the laser pulse (i.e. $I^2 > 0$), and so it can be assumed that the rate of promotion into the excited state is governed only by the laser dynamics, when $n_1(t)$ is constant.

3.2.2 De-excitation

In Equation 3.3, it is shown that excited state population is proportional to ground state density through excitation rate $R(t)$. The depopulation happens at an effective rate, A , and consists of three factors: radiative decay, collisional losses, and losses through ionisation.

3.2.2.1 Fluorescence

The first and most obvious factor is through de-excitation into the fluorescence channel and the atom emitting a photon. This fluorescence photon is how the ground state density can be measured, as it has been shown that the excited state density is directly proportional to the ground state density.

The rate of total decay from the upper state is given by A_2 , and is the sum of all decay rates into all possible lower states, k .

$$A_2 = \sum_k A_{2k} \quad (3.5)$$

The reciprocal is referred to as the natural lifetime, $\tau = 1/A_2$, and henceforth values for decay rate will be given with respect to the lifetime in nanoseconds rather than the actual rate in s^{-1} . The transition into the fluorescence channel that is of interest and detected is denoted as A_{23} to signify the rate of decay from E_2 to E_3 .

3.2.2.2 Collisional Quenching

In a collisional system, loss of energy from the excited state is not limited to radiative processes. Other plasma species can collide with the excited species and steal away the energy before it has a chance to fluoresce. If this is unaccounted for, then an observer would underestimate the density of the species being measured, as there is less signal. This phenomena is called Collisional Quenching.

Collisional quenching acts to reduce the lifetime of the upper state by providing another loss channel at a given rate, Q . The effective excited state loss rate is now $A = A_2 + Q$. Different species in the plasma quench different excited states at different rates, and that rate is given by $n_q k_q$, where n_q is the density of a given quenching species and k_q is the quenching coefficient. To properly account for collisional quenching, the sum of all these rates are taken over all possible partners q :

$$Q = \sum_q n_q k_q \quad (3.6)$$

The quenching rate of some excited states, for a small selection of chemical species, has been measured with the use of a Stern-Volmer plot [59, 88, 96–98]. By plotting the measured decay rate against the partial pressure of an interacting gas, the coefficient can be estimated, as well as the natural lifetime of the excited state by extrapolating to zero partial pressure. At atmospheric-pressure, collisional quenching is the more dominant loss process for most excited state species, i.e. $Q > A_2$, which has significant implications for TALIF.

Let us consider a typical helium working gas with 0.3% N_2 admixture at atmospheric-pressure, which has been measured as the optimal N_2 admixture for N production [67], and calculate the effective lifetime of the atomic nitrogen $N(3p \ ^4S_{3/2})$ state assuming only helium and molecular nitrogen as quenching partners. The natural lifetime is taken as 26.9 ns, from the NIST atomic database [99], in very good agreement with [70, 89, 96, 97, 100]. The quenching coefficients are taken from [88], and the rates calculated assuming a gas temperature of 300 K. The effective lifetime of the excited state is reduced to 3.2 ns.

When collecting light over the whole fluorescence signal, assuming a exponential decay, the loss in signal would suggest a ground state density over an order of magnitude less than in reality. Clearly then, collisional quenching is one of the largest possible sources of error when performing TALIF at elevated pressures, and must be accounted for with care.

Unfortunately, not all quenching coefficients are known for all excited states and interacting species. This often limits the utility of TALIF of highly collisional systems to gas mixtures where the quenching coefficients are known, and even then the uncertainty of those coefficients can be large. This is twinned with the problem that for species where quenching coefficients are known, densities of interacting species, especially in chemically rich plasmas, or in an uncontrolled environment such as in open air, may be unknown. The quenching

rate in these situations is usually approximated by assuming the only interacting species take the form of the feedstock gases when TALIF is confined to the core plasma, or those in a controlled atmosphere which is unrepresentative of open air operation.

3.2.2.3 Ionisation

Fluorescence and collisional quenching are not the only loss mechanisms that can occur. It is possible in the system to have a third photon absorbed, causing species to become ionised (with rate given as Γ_2). In this case there is no fluorescence, but the excited state density becomes altered, along with the effective decay rate Equation 3.7. This phenomena can be seen as a saturation in detected iCCD signal with increasing laser energy as measured by an Ophir Optronics laser energy meter, as shown in Figure 3.2 for krypton.

$$A = A_2 + Q + \Gamma_2(t) \quad (3.7)$$

In this study, measurements such as those in Figure 3.2 are made regularly, and the laser energy is deliberately kept low to minimise photoionisation, and therefore $\Gamma_2(t) \simeq 0$. Laser energies used are well below where saturation begins (for Figure 3.2 a typical value would be less than $40 \mu\text{J}^2$), and the fluorescence signal remains proportional to I^2 with negligible photoionisation, and the effective decay rate can be simplified to Equation 3.8.

$$A = A_2 + Q \quad (3.8)$$

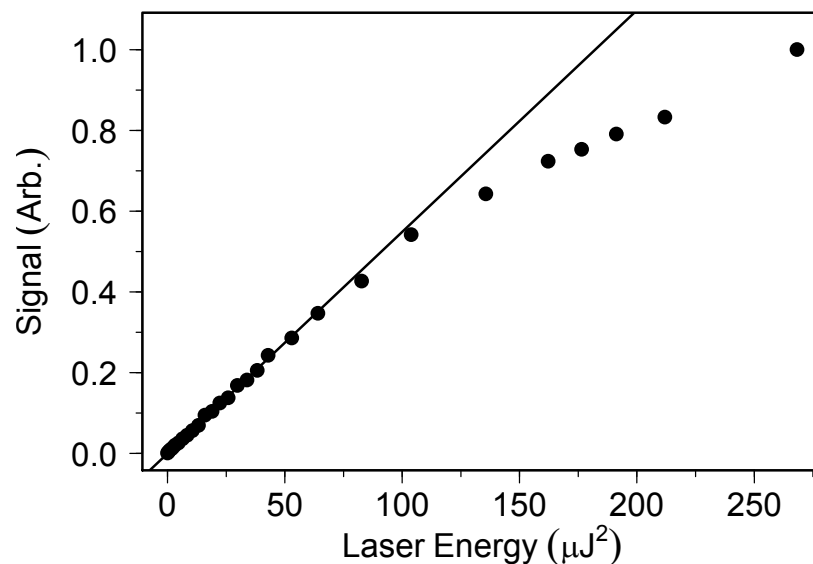


Figure 3.2: Sample krypton TALIF signal with increasing laser energy shows a linear response (to I^2) up to $70 \mu\text{J}^2$. TALIF signal begins to saturate, indicating significant photoionisation.

3.2.3 Fluorescence Detection

With negligible ionisation, the decay from the upper state is given by $A_2 + Q$. If the upper state is no longer being filled, then the recorded signal will be an exponential decay with lifetime $\tau = 1/A$. The detection system is usually tailored to record a particular wavelength, with $h\nu = E_2 - E_3$.

The reduced optical branching ratio a_{23} , is the Einstein coefficient for the fluorescence transition of interest A_{23} , divided by the total decay of the excited state A defined in Equation 3.8. In real terms, it gives the fraction in which the excited state will decay into the fluorescence channel which is being monitored, compared to the fraction that will be lost to other states and through collisional quenching.

$$a_{23} = \frac{A_{23}}{A_2 + Q} = \frac{A_{23}}{A} \quad (3.9)$$

In the limit that $Q \rightarrow 0$ the optical branching ratio, Equation 3.9 reduces to $a_{23} = A_{23}/A_2$, which is merely the ratio between the Einstein coefficient of the fluorescence channel decay, and the sum of all possible radiative decay channels. For some TALIF species, when there is no collisional quenching, the fluorescence channel is the only radiative de-excitation path allowed and therefore $A_2 = A_{23}$ and $a_{23} = 1$, however this is not the case for all species. A good example of this is when performing TALIF of xenon, a common gas used when performing TALIF. The $\text{Xe}(6p'[3/2]_2)$ excited state has many lower states that it can decay in to. Fluorescence into the $\text{Xe}(6s'[1/2]_1)$ final state is utilised in TALIF [59], and it is predicted that there is only a 0.733:1 chance of this particular transition [98] when assuming no other losses such as quenching. The remaining 26.7% will decay into other states, and the emitted photons (being at a different wavelength to that being detected) are not recorded. This would lead an investigator to once again underestimate the ground state density due to this lack of signal. Not only is the effective decay rate of the excited state A required, but also the natural radiative decay rate of the fluorescence state A_{23} .

Finally, it is possible to express detected fluorescence signal in terms of the ground state density, laser intensity, and detection sensitivity. The signal detected S , will be dependant on the sensitivity of the detector at a given fluorescence wavelength $\eta(\nu)$, and transmission of the various optics $T(\nu)$. The photons that are emitted are isotropic [59], and consequently the number of captured photons will be a fraction of the total $n_{h\nu}$, based on the solid angle of detection $\Delta\Omega$. This results in the expression in Equation 3.10,

$$S = \eta T \frac{\Delta\Omega}{4\pi} n_{h\nu} \quad (3.10)$$

but this expression still requires information regarding $n_{h\nu}$. The number of photons is the product of the optical branching ratio a_{23} , and the excited state density n_2 .

$$S = \eta T \frac{\Delta\Omega}{4\pi} a_{23} n_2 \quad (3.11)$$

Still more information is required as the excited state density is a function of ground state density, the laser intensity, and time as shown in Equation 3.3. By substituting in for $R(t)$ from Equation 3.1, and integrating Equation 3.3 in space and in time between 0 and ∞ , the detected signal is given as,

$$S = \eta T \frac{\Delta\Omega}{4\pi} a_{23} n_1 G^{(2)} \sigma^{(2)} g(\nu) \left(\frac{E}{h\nu} \right)^2 \quad (3.12)$$

where E is the laser pulse energy, and when divided by the photon energy $h\nu$ yields a photon count. This can be rewritten in terms of the laser wavelength instead, which is conceptually easier to interpret when considering different excitation schemes.

Rearranging Equation 3.12 can yield the ground state density n_1 , however it requires knowledge of the spatio temporal characteristics of the laser pulse, as well as the spectral profile for the normalised laser profile. This is coupled with the prospect of no calculated or measured two-photon excitation cross section available in the literature.

3.2.4 Calibration

To allow an absolute measurement of species, the fluorescence signal can be normalised against a known concentration of the species in question. Unfortunately for atomic species that are unstable, such as N that prefers to be diatomic, having a set stable density to sample against is difficult. One solution is to produce the species of interest using a chemical reaction. This can be done for example using a flow tube reactor [101]. In these cases the whole system including the response of the detection system is calibrated directly in one measurement. As the density of the detection species is changed, a relationship between acquired signal and density is made directly. This removes the required knowledge of the detection system losses, laser pulse characteristics, and two-photon excitation cross section.

Unfortunately containing the species of interest or producing it using a flow reactor is not always possible, or reliable [102], and as a result it is sometimes a more convenient solution to use a noble gas reference as first used by Goelich *et al.* [95]. These gases offer an inert, stable source of atoms with which to utilise, with electronic structures somewhat similar to the species of interest.

For calibration gas to be useful, it is vitally important for it to have an excitation transition spectrally close to that of the species of interest. This allows for the laser system to share the same spatial, spectral, and temporal shape [103], which is an important assumption when using a noble gas calibration. For example, atomic nitrogen shares a similar electronic structure to krypton. The excitation wavelengths are around 207 nm and 204 nm respectively. This allows the laser to share the same operating paradigms in both cases, meaning

that the spatial, spectral, and temporal distributions are approximately the same. It is for that reason why krypton will be used in this work as the noble gas calibration to N.

To calibrate the TALIF signal of the noble gas reference (in this case krypton) to the signal from the species of interest (atomic nitrogen), the ratio between the two is taken. Fluorescence signal is measured for both the reference species S_R , and the species of interest S_X , the unknown ground state density n_X can be found by taking ratios of the signals.

$$n_X = \frac{\eta_R T_R}{\eta_X T_X} \left(\frac{\lambda_R}{\lambda_X} \right)^2 \frac{\sigma_R^{(2)}}{\sigma_X^{(2)}} \frac{a_{23R}}{a_{23X}} \left(\frac{E_R}{E_X} \right)^2 \frac{S_X}{S_R} n_R = \chi \frac{A_X}{A_R} \frac{S_X}{S_R} n_R \quad (3.13)$$

The detection sensitivity η and optical transmission T are known or can be found experimentally to a good precision. The squared ratio of the laser photon wavelengths λ , are also known. The ratio of two-photon excitation cross sections $\sigma_R^{(2)}/\sigma_X^{(2)}$ is taken from literature. The explicit cross sections are not known for either krypton or atomic nitrogen, meaning that it is not possible to use values and forgo calibration. However from carefully made measurements using known densities of both N and Kr, the ratio between the two has been estimated to $\pm 50\%$ precision [88], and it is this value that is used.

The laser pulse energy needs to be known for both cases, and the ratio is given by $(E_R/E_X)^2$. As the laser spatial profile is assumed to be the same for both cases, by using similar excitation wavelengths, only the total energy is required, rather than the time integrated intensity. Optical branching ratios are known from the natural radiative decay rates and the measured effective decay rates.

The ground state density n_X reduces down to known ratios from literature or are invariant over the experiment given as χ , the ratios of measured effective decay rate (A for that species and quenching partners), detected signal S_X/S_R , and the reference gas density n_R .

3.3 Considerations for atmospheric TALIF

Traditionally, due to their small bandwidth, reasonable degree of tunability with dyes and crystals, and of course their general ubiquity, nanosecond pulsed lasers have been the conventional choice for performing TALIF.

If the laser pulse width is much smaller than $1/A$, then it can be considered that excitation happens very quickly on time scales of the excited state decay. At low-pressure there is very little collisional quenching, and a typical 5 ns laser pulse width is small compared to natural lifetime τ on the order of tens of nanoseconds. Excitation happens instantly in comparison to the decay of the excited state. The unperturbed fluorescence decay can therefore be monitored, and A can be measured directly.

Atmospheric-pressure plasma jets are utilised because of their operation in open air environments. As mentioned previously in 3.2.2.2, collisional quenching substantially reduces

the effective lifetime of the excited state. Use of nanosecond lasers as used in previous investigations [3, 59] is not tenable as the pulse length of ~ 5 ns is on the same order as τ . The decay of the excited state is convoluted with the interacting laser pulse, and it is not always trivial to deconvolve the two. The decay rate then must be estimated, to correct for the loss of signal, using available quenching coefficients in literature. Previous studies have been limited to scenarios where quenching coefficients can be known to a good accuracy.

Quenching in the core plasma can be approximated to contributions by the feedstock gas only. The contribution from chemical products made in the plasma is negligible when considering their low density. TALIF in the core plasma has been performed previously utilising this method [2, 67]. When interested in the effluent or afterglow of a plasma, the device is kept under a controlled atmosphere that matches that of the feedstock gas, or a known density of a gas with a well known quenching coefficient [3, 90, 104]. This method allows for estimates of species densities beyond the core plasma to a reasonable degree.

When operating in an environment of unknown species, perhaps in a plasma with many feedstock gases or in humid ambient air, the estimation of the quenching contribution becomes almost impossible. It is difficult to know the densities of all quenching partners, especially when considering fluid mixing and diffusion. Furthermore, a concern is that the quenching coefficients may not be known, or are not known to a reasonable precision for these species. There is a solution that overcomes this need to accurately estimate the decay rate, and that is to measure the decay directly. This can be achieved using an intensified charge coupled device (iCCD) capable of resolving the decay rate at the nanosecond level, but more importantly using a laser pulse width on the order of picoseconds or femtoseconds [105] which is much shorter than the decay time of the excited state, analogous to the low-pressure case.

3.4 Experimental procedure

To offer a short laser pulse width for performing TALIF at atmospheric-pressure, the laser system used is an EKSPLA PL2251 series Nd:YAG pump laser, capable of pulse widths ~ 32 ps. This is then fed into an amplifier and harmonic generator (EKSPLA APL2100 and H400) before finally being fed into a solid state optical parametric generator (EKSPLA PG411) capable of wavelengths between 193-2300 nm. With a pulse width two orders of magnitude smaller than that of the decay rate, it can be assumed the decay rate is unperturbed. It is now possible to measure both the decay rate A , and the total fluorescence signal S as per Equation 3.13. For the first time there is the capability to measure reactive atomic species under atmospheric conditions without assumptions about quenching rates.

Figure 3.3 shows the basic components for performing TALIF. The laser pulse is created by the laser system at a given wavelength, and passes through a variable attenuation stage.

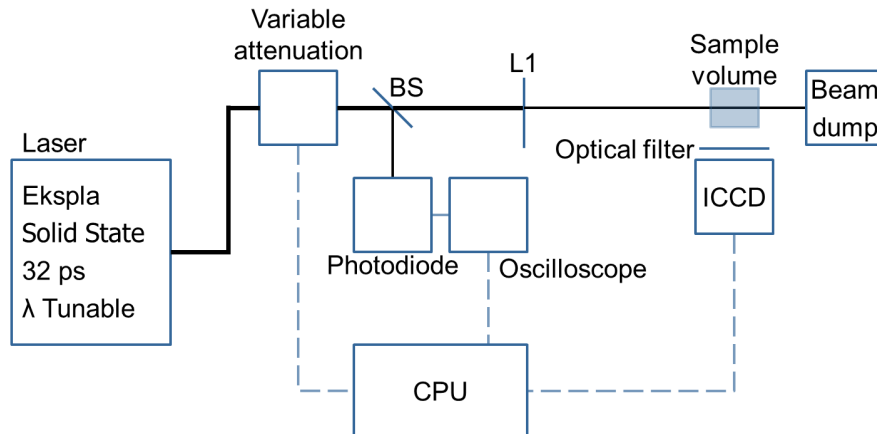


Figure 3.3: Schematic of TALIF experiment.

This consists of two calcium fluoride windows at congruent opposite angles. The first surface of the first window has a variable reflective dielectric coating designed to change reflectivity dependant on angle of incidence. This angle controls the proportion of the beam which is reflected out of the beam path, and manages the laser pulse energy for the experiment. The first window is referred to as the Attenuator. All subsequent downstream window surfaces have an anti-reflective coating to minimise losses. Using the second window acts to negate the change in beam path that comes from the transmission through the Attenuator as demonstrated in Figure 3.4. This second optic is referred to as the Compensator. The Compensator removes the possibility of the beam line moving in space with respect to the camera focus, which is experimentally less demanding. Both the Attenuator and Compensator are on rotational mounts, locked at equal and opposite angles through gearing, and both simultaneously controlled through a Zaber T-NM17A04 stepper motor. The coatings have been specially produced by Layertec Optical Coatings GmbH to operate at a centre wavelength of around 205 nm, allowing their use for both N and Kr TALIF.

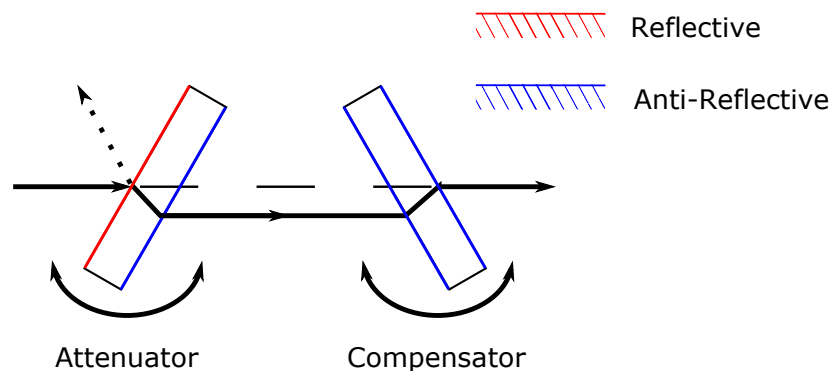


Figure 3.4: Schematic of the variable attenuation stage. The variable attenuator reflects a portion of the incoming laser pulse out of the beam line. The compensator then negates the induced diversion from the beam path.

After the attenuation stage, the laser pulse encounters a beam splitter, constructed from a simple quartz window. This window is placed at 45° to the beam path, leading to 10% being reflected back onto a fast photodiode (Thorlabs DET 10A/M). This reflected signal is further attenuated using a scatterplate, which can move closer or further away with respect to the photodiode to offer more or less attenuation, as well as removing any spatial dependency of the laser beam. The photodiode is used as an indicator of laser pulse energy by monitoring the photodiode voltage on an oscilloscope (LeCroy WaveSurfer 104MXs-B 1 GHz 10 GS/s). This voltage is extracted from the oscilloscope by a computer running a PID (Proportional Integral Derivative) loop that monitors this voltage. A desired voltage value is set by the user, and the PID loop sends commands to the stepper motor of the variable attenuator to maintain this value.

The photodiode voltage is calibrated to laser pulse energy by placing an Ophir PE25-C laser energy sensor just after the focussing lens L1 (Figure 3.3). The beam line once focussed by L1 ($f=300$ mm), and through the sample volume, is safely dumped. To sample different volumes around the μ -APPJ effluent, it is mounted on a 3-axis stepper motor (Zaber T-LSM050A) stage, allowing for precise movement and alignment of the desired volume into the beam line. The jet is mounted with the exit facing vertically upwards (see Figure 3.5) to avoid fluid turbulence from the buoyant helium, and the effluent is probed by the beamline.



Figure 3.5: Photographs of (a) beamline with attenuation stage, photodiode pulse energy detection stage, and APPJ. (b) shows the APPJ mounted vertically on the 3-axis motorised stage, detection optics, and iCCD with filter.

The krypton sample is held in a Starna Spectrosil Fluorometer Cuvette, optically polished on all sides and designed for $> 90\%$ transmission for wavelengths above 200 nm. The cuvette is adapted for a Swagelok gas connection to fill and isolate the cuvette to a particular working pressure of reference gas. To fill the cuvette, it is first evacuated using a turbo pump which is then isolated. Gas fills the cuvette slowly through a needle valve while the pressure is monitored in parallel using an MKS Baratron pressure gauge. Once the desired pressure is reached, a valve on the cuvette is closed, and is removed from the pump/filling system.

The fluorescence is monitored normal to the beam path using an Andor iStar DH344T-18U-73 iCCD camera (1024 x 1024, 13 μm pixel size), capable of 1.9 ns gate width, focussed using a pair of achromat lenses with diameter of 2 inches and combined focal length of 40 mm to offer a large detection solid angle. An optical interference filter is used to isolate the fluorescence light, typically of bandwidth 10 nm. Using an iCCD gives spatially resolved TALIF in the focal plane. A shared region of interest (ROI) is used for both N and Kr cases (see red boxes in Figure 3.6). This gives a spatially integrated decay rate and signal for that integrated region, allowing for spatial resolution. It is important to use the same ROI, for both signals, as this preserves the essential spatio-temporal characteristics of the laser pulse interaction. As the cuvette is physically larger than the plasma jet, krypton TALIF signal is visible across the whole CCD image.

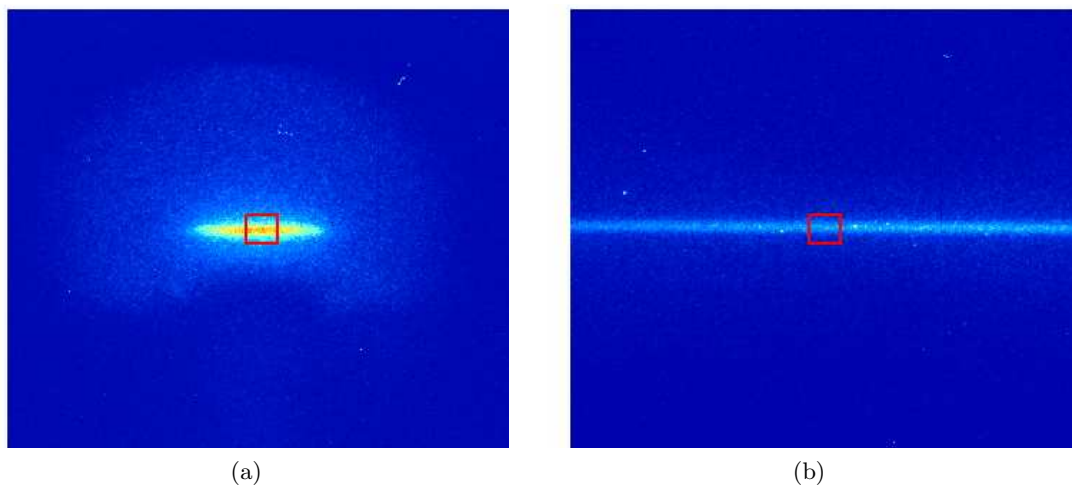


Figure 3.6: TALIF signals of (a) atomic nitrogen in the effluent of the μ -APPJ, (b) krypton at 1 Torr pressure. The same region of interest (red box) is used to find the spatially averaged decay rate and signal for both species.

The signal can be converted into real world space by performing a calibration of pixel size to real size, using the 1 mm electrode separation of the atmospheric-pressure plasma jet. Figure 3.7 demonstrates how the absolute position of the μ -APPJ exit to the beam path, along with the beam width, can be found by using a pixel-mm conversion. Consequently, the beam width was estimated as 100 μm , by taking a FWHM (Full Width at Half Maximum) of the TALIF signal integrated from left to right where there is a strong visible signal.

3.4.1 Excitation schemes

3.4.1.1 Atomic nitrogen

The excitation scheme used for modern N TALIF was proposed by Adams & Miller [96]. Previous to this, researchers used scheme a by Bischel et al [91] as shown in Figure 3.8a. It

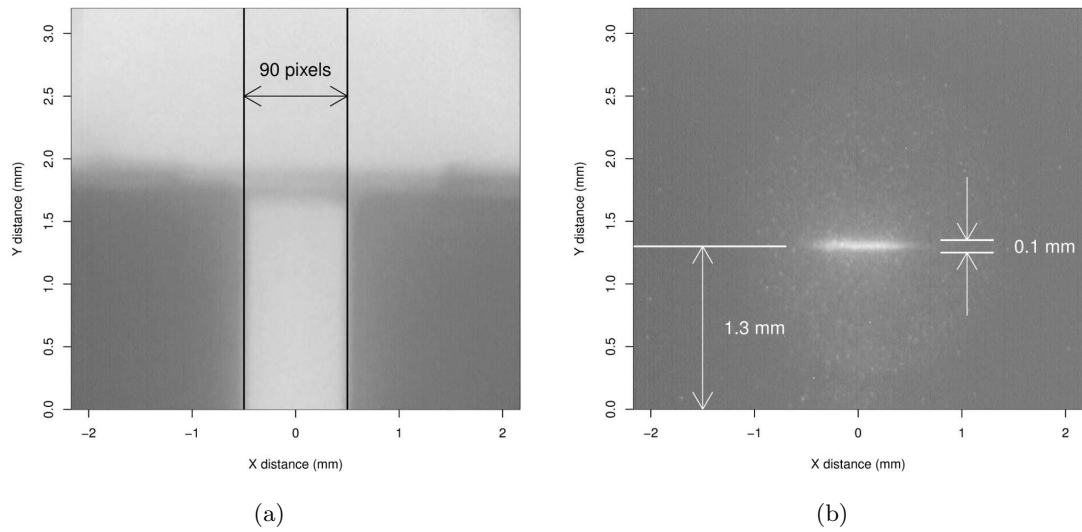


Figure 3.7: (a) The μ -APPJ is illuminated from behind, and extended vertically to get an image of the interelectrode distance of 1 mm. (b) Using the factor (90 pixels/mm) the position of the jet exit and the beam width can be found.

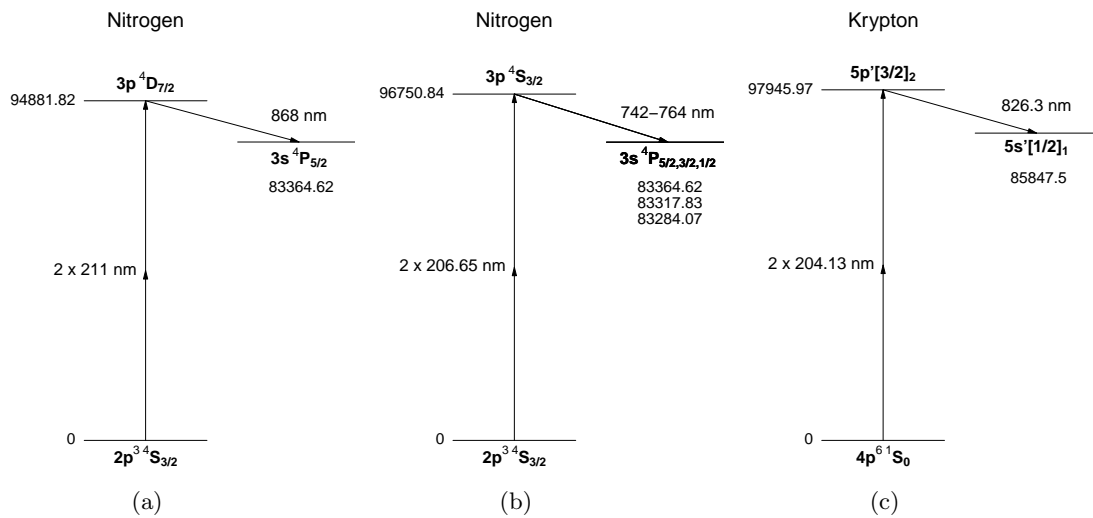


Figure 3.8: (a) Previous TALIF scheme for atomic nitrogen [91] N(211). (b) Preferred TALIF scheme for atomic nitrogen [96] N(207). (c) Preferred TALIF scheme for krypton [88] Kr(204).

uses an excitation wavelength of 211 nm from $N(2p^3 \ ^4S_{3/2} \rightarrow 3p^4 \ ^4D_{7/2})$, hence the shorthand N(211) is sometimes used. The detection wavelength is at 868 nm, based on de-excitation into the $N(3p^4 \ ^4P_{5/2})$ state. The newer excitation scheme (Figure 3.8b) holds many advantages over the old scheme.

The now standard scheme [67, 70, 104, 106] uses an excitation wavelength of 207 nm, which can be more experimentally challenging to produce. However, the two-photon excitation

cross section for the $N(2p^3\ ^4S_{3/2} \rightarrow 3p\ ^4S_{3/2})$ is 3.5 times greater than the $N(211)$ case [96] resulting in more fluorescence photons. The fluorescence wavelength is ~ 745 nm, which offers improved sensitivity for most detectors, which means more signal. Thirdly, the $N(3p\ ^4S_{3/2})$ excited state is self-quenched much less than the $N(211)$ case. This results in longer lifetimes at elevated pressures which are easier to estimate, as well as more signal.

The only slight complication with the $N(207)$ scheme is the decay of the excited state drops into three spectrally close lower levels $N(3s\ ^4P_{5/2,3/2,1/2})$, with only a negligible fraction being lost to IR transitions [107]. Each final state has larger or smaller probability of being populated by decay from the upper state, based on their individual Einstein coefficients as shown in Table 3.1.

Final state	λ (nm)	A_{2k} (s^{-1})	Rel.
$3s\ ^4P_{5/2}$	746.8	1.96×10^7	0.53
$3s\ ^4P_{3/2}$	744.2	1.19×10^7	0.32
$3s\ ^4P_{1/2}$	742.4	5.64×10^6	0.15
		37.14×10^6	1.00

Table 3.1: Final state, wavelength in air λ , decay rate A_{2k} , and relative line strength of $N(3p\ ^4S_{3/2})$ decay. Values for λ and A_{2k} taken from [99].

From Table 3.1, the $N(3p\ ^4S_{3/2} \rightarrow 3s\ ^4P_{1/2})$ transition emits over half the photons at 746.8 nm, with around a third emitted at 744.2 nm, and 15% at 742.4 nm. These wavelengths are subject to different losses due to the interference filter used.

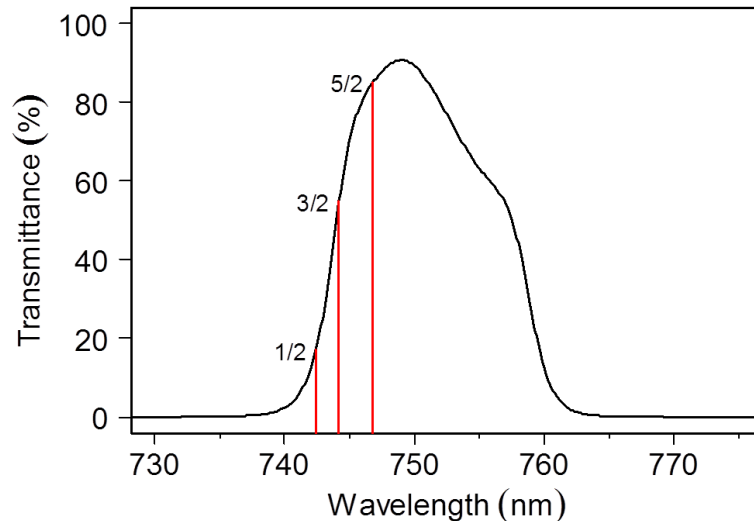


Figure 3.9: Transmission through optical interference filter used for TALIF. Advertised centre of 745 nm and bandwidth of 10 nm. The 3 considered final states are labelled by their J value.

Figure 3.9 highlights how interference filters must be properly characterised for N TALIF.

By taking the sum of the relative strengths convoluted with their respective transmission through the optical filter, the equivalent signal strength reaching the detector is 65.2%. All optical filters used were characterised using a Shimadzu UV-1800 UV-VIS spectrophotometer with 0.1 nm resolution.

3.4.1.2 Krypton

The scheme used for krypton as shown in Figure 3.8c, has a similar transition wavelength to atomic nitrogen (Kr(204) vs N(207)), with a reasonable detection wavelength of 826 nm. The detection wavelength is dissimilar enough to have to use a different optical filter for the detection stage, the response of which is given in Figure 3.10.

The krypton is held in a cuvette with 4 windows of high optical transmission ($> 90\%$ transmission for wavelengths > 200 nm), two windows are aligned along the beam path, the other two are normal to the detection apparatus. The transmission of both the incoming laser pulse, and the emitted fluorescence light were taken from spectrophotometer measurements. Care must be taken, as the spectrophotometer records transmission for the two windows (4 total reflection surfaces) of the cuvette, whereas the excitation happens inside the cuvette after only two reflection surfaces. Likewise emitted TALIF radiation is attenuated by only one window. The transmittance is therefore the square root of the measured two window transmittance.

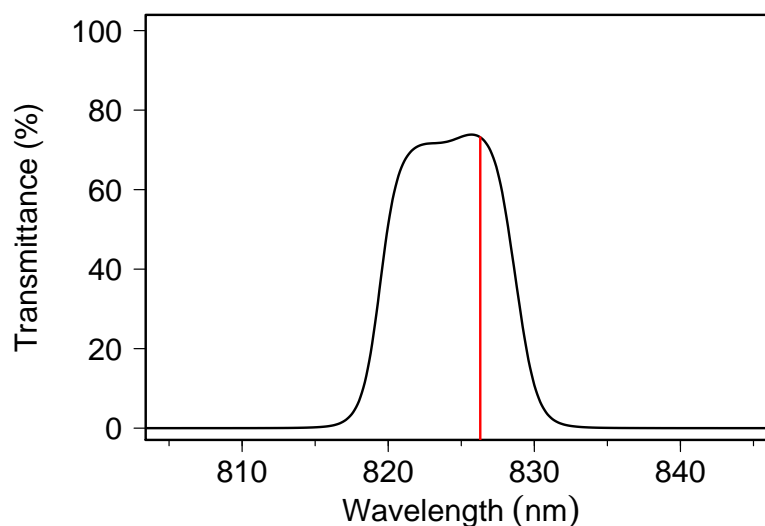


Figure 3.10: Transmission of optical interference filter used for Kr. Transmission at 826.3 nm is 73.1%.

When using a noble gas for calibration, care must be taken to ensure a reliable fluorescence signal. Firstly, the laser energy must be kept low enough to avoid photoionisation, for the signal to be proportional to I^2 (see Figure 3.2). Secondly, the laser intensity must be low enough as to avoid damage to the gas cell windows. This can be tested by performing

multiple TALIF measurements, and monitoring for a loss in signal over time (as the damaged window attenuates the laser pulse). The density must be great enough to render a useful fluorescence signal, but not be self quenched enough to give unresolvable decay rates. For a simpler experimental procedure, the lifetime of the reference species can be set to a value similar to that of the species of interest by increasing the density. For krypton this would be a pressure of around 10 Torr, when considering the self quenching coefficients and natural lifetime from [88]. By having similar lifetimes, iCCD settings can be held constant to give identical response between the sample and reference gases.

For krypton, the gas density, and the laser intensity must be low enough to avoid Amplified Spontaneous Emission, (ASE). Instead of the fluorescence signal being radiated isotropically, there is a coupling for the radiation emitted to be along the beam path, and hence not detected. ASE when using TALIF is a known obstacle [88, 108, 109], however it has also been used, and most documented, as a mechanism for probing electronic states [110–112].

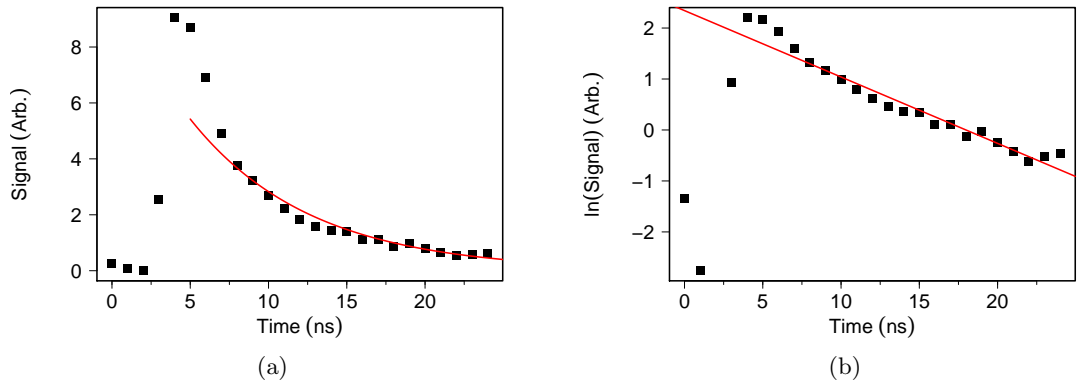


Figure 3.11: TALIF signals of krypton at 10 Torr pressure. (a) Raw data with line of best fit taken in log-space. (b) $\ln(\text{Signal})$ with performed linear fit. There is a clear deviation away from an expected exponential decay due to ASE, with a dramatic decrease in signal at the start of the decay.

Amplified spontaneous emission is caused by a population inversion between the E_3 and E_2 states [113] and is proportional to ground state density. With krypton, ASE is prevalent [109, 113, 114], and very low densities [89, 115] and low laser energies [109] are required to prevent it. Luckily, the use of shorter laser pulses also helps to reduce ASE [108]. The affect of ASE can be seen as a modification of the decay rate in the fluorescence signal. When using 10 Torr of Kr which would offer similar decays rates to atomic nitrogen, and has been the density used in previous TALIF investigations into hydrogen density [109], the loss of excited state population by stimulated emission during ASE gives a “non-linear” decay rate, as shown in Figure 3.11. The rate of decay is accelerated at the start, indicating an extra loss mechanism of the excited state, and is also not constant [115].

Figure 3.12 shows how using a ground state density of krypton to 1 Torr reduces the affect of ASE, giving a usable signal. The low density and laser energy results in very small detection signals, and long decay rates compared to plasma species. These distinctly different detection signals must be managed through experimental techniques.

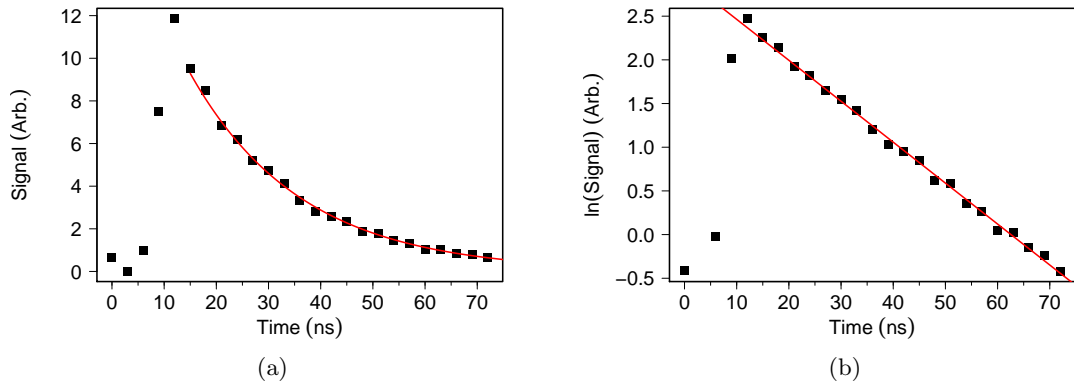


Figure 3.12: TALIF signals of krypton at 1 Torr pressure. (a) Raw data with line of best fit taken in log-space. (b) $\ln(\text{Signal})$ with fit. At lower ground state densities, ASE is not observable. Lifetime of krypton at 1 Torr is estimated to be 21 ns.

3.4.2 Measuring lifetime and total fluorescence

Decay rate is measured by moving a set camera gate width through the decay using a digital delay generator (see Figure 3.13). The laser supplies a pre-trigger to the camera, allowing for internal electrical delays in the camera. The pre-trigger is set early enough that the camera can be triggered up to 8 ns before the laser pulse arrives at the sample volume, allowing for capture just before as well as during the fluorescence decay. These measurements are averaged over 64 images to minimise the effects of fluctuations in laser pulse energy. This can accurately determine the lifetime by taking the natural logarithm and fitting linearly.

Taking the cumulative area under this curve can give a measure of total fluorescence signal, as long as measurements are taken into the noise floor, ensuring capture of all available signal. When the lifetime of both the species of interest, and the reference gas are similar, then the same detection gating can be utilised.

However, for atomic nitrogen with a lifetime of ~ 3 ns, a gate step of 1 ns is used and the gate width is 2 ns, whereas the slow lifetime of ~ 21 ns for Kr at 133 Pa (1 Torr) yields only a small signal at 2 ns. The gate width must be increased to maintain a reasonable signal-to-noise ratio, a gate width of 6 ns offers an acceptable signal. Also, steps of 1 ns is inefficient when the lifetime is much longer. The steps are closer to 3 ns to effectively sample the Kr decay with a reasonable resolution. The changes in gate width mean that simply taking the sum of all the data points is not comparable between the two cases as the iCCD does not have a linear relationship of signal and gate width to counts response.

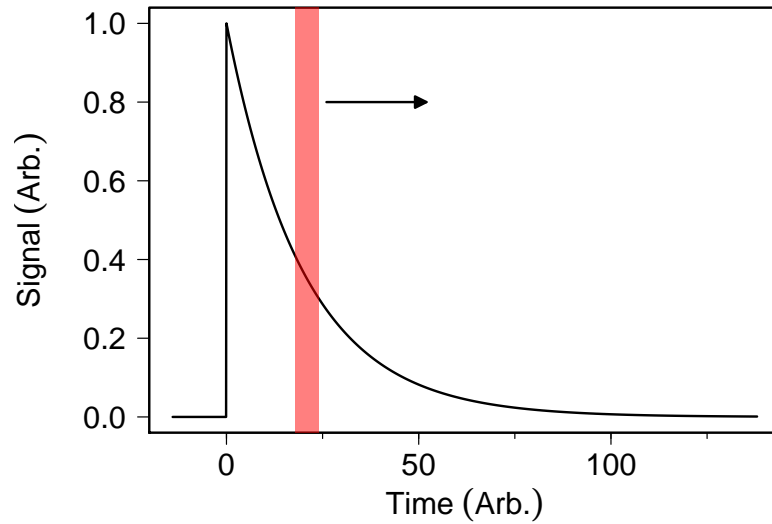


Figure 3.13: Schematic of how the camera gate delay is increased as to sample the fluorescence decay at different points in time.

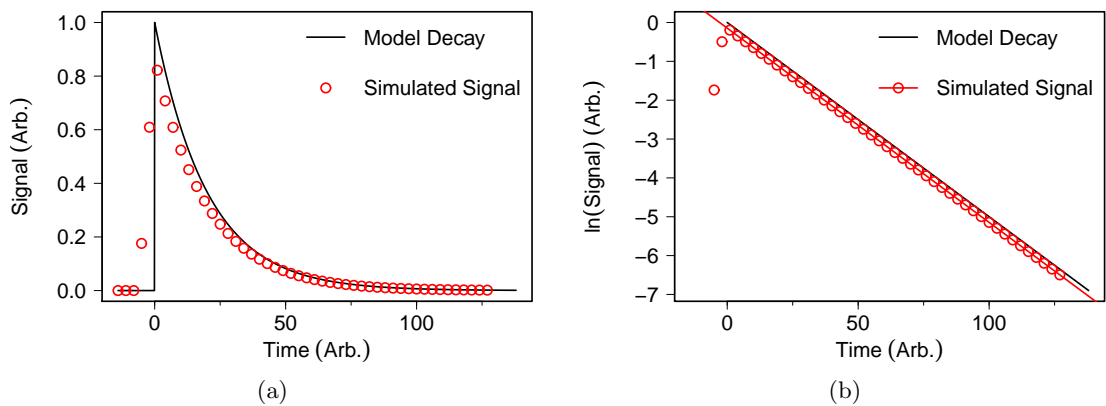


Figure 3.14: At each camera gate delay, the recorded signal exhibits the same decay as the true fluorescence. (a) shows the simulated recorded signal in time. The exponential decay model and the simulated TALIF signal have identical decay constants (b), showing that a stepped constant detection gate of scale similar to that of the decay can correctly capture the fluorescence decay rate.

With different gate widths and step sizes, it is required to ensure that a gate step and width of arbitrary value will record the lifetime correctly (see Figure 3.14). A “model decay” of a simple exponential function, is integrated between two points of the iCCD gate, simulating when the gate is open and acquiring signal. This “simulated signal” is repeated for different gate steps along the signal decay. This produces measures of signal for given gate delays, as would be the case in experiment. By comparing the estimated lifetime of the simulated iCCD signal, to that of the pure model exponential decay, it can be shown that for this experiment, the decay can be correctly estimated using any gate width or step size.

To measure the total fluorescence, in each scenario, a secondary image is taken with a long gate width that spans the signal decay. Once a background measurement has been removed, what is left is the total fluorescence signal, using the same gate width (therefore iCCD response) for both N and Kr.

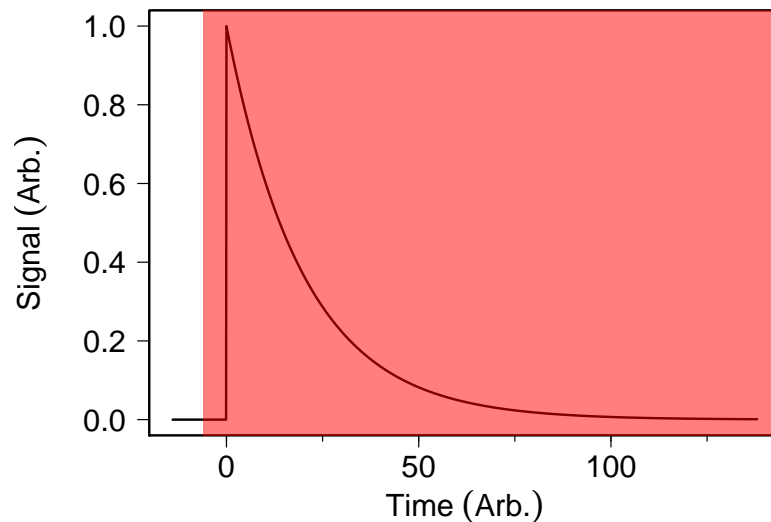


Figure 3.15: The total fluorescence decay can be captured separately using a long detection gate. The long exposure gate width is determined by the expected decay constant

Of course there is no possible way to capture the infinitely long exponential decay, however the camera gate can be held open long enough to capture 99.9% of the possible light. Integrating the exponential decay between 0 and a given gate width time will yield the fraction of the total signal collected (see Equation 3.14). This integral can be rearranged to instead give the required gate width for a given wanted total signal. Using a desired detection fraction of 0.999, which is 99.9% of all possible signal, and the lifetime of krypton at 1 Torr of ~ 21 ns, using Equation 3.15 the required long gate width is ~ 145 ns. Considering a detection fraction of 0.99 corresponds to a gate with of ~ 100 ns, a few nanoseconds of included “dead” time before the laser interaction and fluorescence begins, as in Figure 3.15, is acceptable.

$$\text{detection fraction} = 1 - \exp\left(-\frac{\text{gate width}}{\tau}\right) \quad (3.14)$$

$$\text{required gate width} = \tau \times -\ln(1 - \text{required detection fraction}) \quad (3.15)$$

To make a background measurement, the delay of the camera is placed 500 ns after the laser pulse interaction. This gives a region in time where an immeasurable TALIF signal should be taking place. A gate width of 145 ns is also roughly two RF cycles at 13.56 MHz. This means that any stray light from the plasma source should also be well averaged, especially over the 256 accumulations usually undertaken per datum. These long gate width exposures are taken as a function of wavelength to sample over the normalised line profile, which is then fitted to a Gaussian distribution. The area of this distribution is the recorded signal used, as it does not require knowledge on the exact shape of $g(\nu)$, and cancels out longer term wavelength fluctuations in the laser system.

3.5 Error estimation

In Equation 3.13, there are sources of systematic error in χ , and sources of stochastic error in the measured values of decay rate A and signal S . Firstly, systematic errors will be considered.

3.5.1 Quantum efficiency and optical transmission

The values for quantum efficiency are taken from data sheets supplied by the manufacturer of the iCCD. These do not have an associated error given, however when using digitisation tools, and considering variation in manufacture, the error is estimated for the ratio is $\pm 10\%$. The ratio of optical transmission of the iCCD focussing lenses (Thorlabs 2" 80 mm achromatic) between the 745 nm region and 826 nm is almost identical at 99% recorded to the second decimal. This value for possible error in the ratio is essentially negligible when considering other factors. Transmission of the filters has been measured (see Figures 3.9 and 3.10) with high wavelength resolution. Assuming a conservative 0.1 nm error in wavelength calibration of the spectrophotometer, the associated error in transmission when considering the individual line strengths of atomic nitrogen as well as transmission in and out of the gas cell is 1.84% for the N signal, and 0.78% for the Krypton signal. The error in these ratios is taken in quadrature, resulting in $\pm 10\%$.

3.5.2 Natural lifetime, branching ratio, and two-photon absorption excitation cross section

By rearranging the reduced optical branching ratio a_{23} to extract the measured decay rates A in Equation 3.13 the constant values left hidden in χ is

$$\frac{A_{23R}}{A_{23X}} = \frac{a_R^* \times A_{2R}}{a_X^* \times A_{2X}} \quad (3.16)$$

where a^* is the radiative optical branching ratio with no quenching (i.e. A_{23}/A_2), and A_2 the natural decay of the excited state. The optical branching ratio for krypton is taken from [97], and the branching ratio for atomic nitrogen is unity. The optical branching ratios themselves have only a small amount of error, in the range of $\pm 2\%$ [97], however there are large discrepancies in the radiative natural lifetime of the excited unquenched states $A_2 = 1/\tau^*$. For krypton the value of $\tau^* = 34.1 \pm 3.4$ ns is used [116], though it is in disagreement with earlier work (26.9 ± 0.3) ns [97], it has been cited as a more reliable study [88], with some supporting measurements made by others [109]. For N, the value of $\tau^* = 26.9 \pm 1.5$ ns is used [99, 116]. These errors equate to 5-10 %, and in quadrature gives and overall ratio error of $\pm 11.5\%$.

The largest error however comes from the estimation of the two-photon excitation cross section. This is usually found empirically, as the quantum mechanical estimation required is not trivial [117–120] and rarely confirmed experimentally [121]. For some species, such as krypton, no estimations exist. Instead the ratio between two species is found, rather than the absolute values themselves [88, 95, 109]. These values have a large uncertainty of $\pm 50\%$. The overall error from all possible systematic values is $\pm 53\%$, effectively the largest error $\pm 50\%$ due to the uncertainty in $\sigma^{(2)}$.

3.5.3 Stochastic errors

Though there is possibility of large systematic errors, this only comes into play when considering absolute values of density. Relative measurements are affected only by stochastic errors during the measurement process.

3.5.3.1 Signal and the normalised line profile

The signal detected as a function of wavelength is proportional to the normalised line profile $g(\nu)$. By integrating over wavelength, this function becomes unity, and the signal is now proportional to the area of the integrated function. When using a traditional nanosecond dye laser with a doubling (or tripling) crystal, the output wavelength can be changed using a grating inside the cavity, allowing for tunability of the wavelength over the transition. This offers many points with which to fit a Voigt profile to. By integrating over a given normalised function (the integral goes to unity between minus and positive infinity such as the Voigt),

means the signal is no longer dependant on the shape of the normalised line profile, for both the species of interest and the calibration species, but only the integrated area [109]. The signal intensity can change for example with temperature due to Doppler broadening, and so staying at one laser wavelength and comparing values is not valid, hence integrating across the whole transition is required.

Fitting Voigt functions is a topic of interest mathematically and computationally [122, 123], as with many degrees of freedom, the probability space is large and computational tricks must be used to fit this distribution well. The use of the pseudo-Voigt is a useful trick, a reduction of the complicated convolution to just the sum of a Lorentzian and Gaussian which are weighted to give a fair approximation. This can be subsequently found using a fitting procedure of choice. Alternatively, with computing power in abundance, using Bayesian analysis to fit the distribution, and give meaningful error estimation in the process, is perhaps a more robust approach, especially if data is scarce [124, 125].

The ps laser system used in this study is locked to wavelength steps roughly the size of its bandwidth, so at 206 nm, this is a step size of 0.02 nm. In Figure 3.16, it is apparent that only a few points are available for fitting a distribution to the TALIF signal. It is assumed that the broad laser profile dominates over the other broadening processes, leaving an approximately Gaussian response rather than a true Voigt. The FWHM Doppler broadening of the N absorption line can be calculated using $\Delta\tilde{\nu} = \lambda^{-1}(8 \ln 2 k_B T / mc^2)^{1/2}$ [126]. For atomic nitrogen with a mass of 14 amu, and assuming a temperature of 310 K the value is 0.163 cm^{-1} . This is an order of magnitude smaller than that of the laser, which is reported by the laser manufacturer to be around 4 cm^{-1} . However, Doppler broadening gives a Gaussian distribution, and so these two values simply sum together. In contrast the naturally pressure broadened line width [127], using a value for the decay rate at atmospheric-pressure, though Lorentzian in profile has a width two orders of magnitude smaller than that of the Doppler broadening, and hence is assumed to be negligible.

Fitting a Gaussian profile is common in TALIF experiments at atmospheric-pressure [89, 109], and estimates a width of around 4 cm^{-1} which is consistent with that of the laser bandwidth. The 95% confidence interval for the area in Figure 3.16 reveals a less than 4% difference in signal. However, with so few points, over fitting is a evident problem, and would automatically lead to “good” fitting. Without more data points it is very difficult to give a credible value to the possible error from fitting. A conservative estimate of $\pm 8\%$ will be used in this analysis.

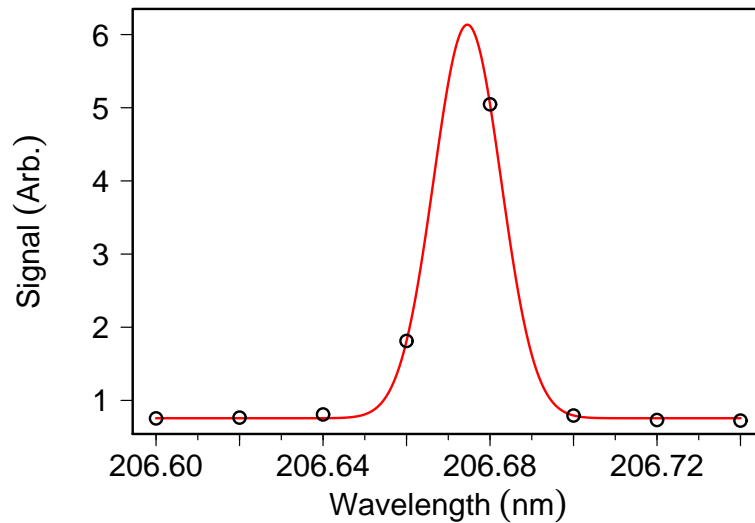


Figure 3.16: Gaussian fit to N TALIF as a function of laser wavelength. Very few points are available for fitting, leading to large possible errors.

3.5.3.2 Lifetime estimation

At a laser wavelength that gives the most signal, e.g. in Figure 3.16 the wavelength is 206.68 nm, the signal is measured as a function of time as described in Section 3.4.2. Due to a large number of points and a good signal to noise ratio, fitting of the lifetime is robust. Even with low signal quality, the error that is estimated during the fitting procedure is no more than $\pm 5\%$.

3.5.3.3 Detection fluctuations

The iCCD used will impart some amount of noise to the measurement, however it is important to rule out any underlying trends or abnormal behaviour. Using a Thorlabs LIUCWHA white light LED Array, the camera signal was monitored using the same gain, gate, and delay settings as is used when performing TALIF. Using three standard deviations from the mean, the deviation is less than $\pm 2\%$, which can be expected when considering the LED array is not a perfect constant light source.

3.5.3.4 Laser energy and plasma stability

The laser energy is monitored throughout the measurement to ensure it has not appreciably decreased or increased during the experiment. Even though it is controlled by the active attenuation stage, there is still a $\pm 1\%$ drift per hour over the course of a full experiment. More importantly there is some shot to shot variation of around $\pm 3\%$, which is made worse when considering the signal is based on I^2 . To combat this, the recorded signal is averaged over many laser shots. For the decay rate, typically 64 shots are taken as this estimation is

robust to noise, but also the most time consuming. For measuring time integrated signal, 256 shots are averaged over which leads to a lower shot noise fraction. Using krypton as a “standard” source, of which the signal should not change in time, it was found that 64 and 256 shots for the lifetime and integrated signal respectively give very reproducible results.

When measuring with the plasma however, it needs time to stabilise both chemically and thermally. It is operated for at least an hour, often two hours while the laser system itself is warming up. Through measurements of optical emission spectroscopy, it has been found that this is sufficient time for the plasma to reach an equilibrium state. When parameters are changed such as input power or gas admixture, the plasma is left for at least ten minutes to stabilise.

3.5.4 Total error estimation

Table 3.2 collates both systematic and stochastic errors for TALIF measurements. The error when making relative measurements is dominated by the vague uncertainty from fitting a distribution to the signal data to integrate out the normalised line profile, with an estimated $\pm 14\%$ maximum error. Of course for each measurement, the error from the effective decay rate can be included directly, as well as the error from fitting the distribution, which can have an extra factor included to represent the possible over fitting that may be occurring with so few usable fitting points. These two give a reasonable idea of the possible stochastic error when considering the other factors are small.

When calibrating to give an absolute measurement of a species, the systematic errors possible from the required fixed values lead to a possible error of 53%, completely dominated by the error in the two-photon absorption cross section ratio. TALIF results will show error bars for the stochastic component only, with the caveat that all absolute density measurements are subject to a systematic error of $\pm 53\%$.

Systematic		(%)	Stochastic		(%)
Quantum efficiency	η	10	Normalised line profile	$g(\nu)$	8
Optical Transmission	T	negligible	Effective decay rate	A_{eff}	5
Branching Ratio	a^*	2	Laser energy ²	I^2	2
Natural lifetime	A_2	11.5	iCCD response		2
Two-photon Excitation cross section ratio	$\sigma^{(2)}$	50			
		53			14

Table 3.2: Estimated errors for various fixed and measured values. Systematic errors are dominated by the error in the two-photon absorption cross section ratio, where as the the stochastic errors are dominated by the uncertainty in the fitted area using a Gaussian profile.

3.6 Results

3.6.1 Variation in N₂ admixture

Figure 3.17 shows the central absolute atomic nitrogen density 1 mm from the jet exit as a function of molecular nitrogen admixture in 1 slm He and an applied voltage amplitude as measured at the APPJ electrodes (described in full in Chapter 4) of 295 V, with a broad peak in atomic nitrogen production at 0.3% N₂ admixture. This is consistent with previous relative measurements [67], as well as absolute measurements made using mass spectrometry [68] and VUV absorption [58]. Clearly, adding more reagent species does not necessarily lead to greater N production, revealing the non-linear nature of plasma chemistry. The peak does not vary to any great extent with applied voltage (275 V to 450 V), meaning that for optimum production, the admixture should be between 0.25–0.35%.

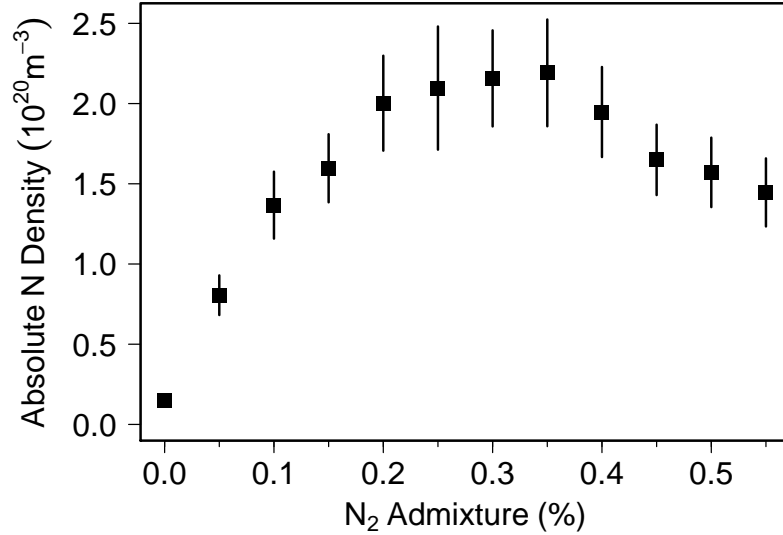


Figure 3.17: Absolute N density with changing N₂ admixture. The density peaks around 0.3% N₂ in 1 slm He. The broad peak is invariant with applied voltage, in this case 295 V.

The shape is a trade off between the production of N with increased N₂ density, which is proportional to $\sqrt{n_{\text{N}_2}}$ [67], and the increased population of molecular ro-vibrational states which modify the EEDF (Electron Energy Distribution Function) and rob the system of energy, and so fewer electrons have sufficient energy to dissociate N₂ [128]. The latter begins to out compete the former and a peak production admixture is the result. Other species such as atomic oxygen share similar dependencies on operating parameters [2, 3].

As suggested, atomic nitrogen production may act as a precursor for other relevant chemical species, either in the effluent itself or when in contact with liquids. The overall trend of atomic nitrogen production with molecular nitrogen admixture correlates well with measured nitric oxide production in the effluent of the μ -APPJ [4]. It was found that a peak

in NO production occurs at the same molecular admixture, as well as the steep rise at low admixtures, and extended tail after 0.35 % N₂, indicating that N is indeed a vital precursor molecule for some applications.

3.6.2 Variation in applied voltage

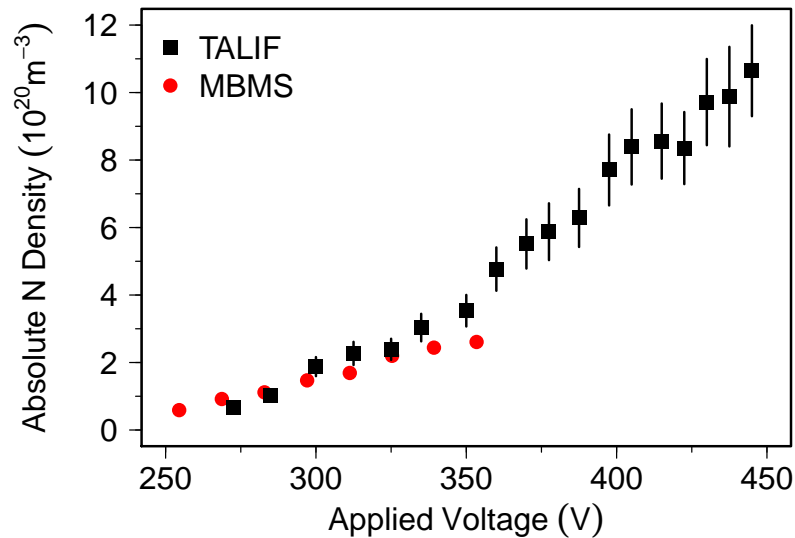


Figure 3.18: Absolute N density with applied voltage for 0.25 % N₂ admixture. Species density increases roughly linearly with input voltage. TALIF shows good agreement to Molecular Beam Mass Spectrometry [68] using a higher flow rate of 1.4 slm and 0.25 % N₂.

Figure 3.18 illustrates the linear nature of N density increasing with applied voltage amplitude. This has been observed during relative TALIF measurements in previous investigations [67], and the absolute values are consistent with mass spectrometry data [68] which also measures in the effluent. Density can vary greatly, between $(0.7 \pm 0.1) \times 10^{20} \text{ m}^{-3}$ at 270 V to $(10.6 \pm 1.3) \times 10^{20} \text{ m}^{-3}$ at 445 V before the plasma becomes unstable. For the lowest driving voltage, assuming a gas temperature of 300 K at atmospheric-pressure, the dissociation fraction is 0.1 %. For the highest driving voltage, the dissociation fraction is above 1.4 %. Higher driving voltages produce greater electron densities, which can go on to produce more of some reactive species, such as atomic nitrogen, through electron impact dissociation [63]. As with atomic oxygen in the μ -APPJ [2, 60], increased driving voltage (and therefore power) increases the density of atomic nitrogen, but there is two orders of magnitude difference between the two.

Considering the dissociation energy thresholds for N₂ and O₂ are 9.79 eV and 5.16 eV respectively, this may begin to explain why the dissociation fraction for atomic nitrogen is so low. There is little work in terms of simulations for the μ -APPJ operating with nitrogen, though there are simulations using helium and oxygen [43]. These fluid simulations show the electron energy probability function (EEPF) is greater for the lower energy threshold for

dissociation of molecular oxygen, compared to the dissociation energy of molecular nitrogen which is nearly twice as high. Molecular nitrogen then is less likely to be dissociated due to the lack of electrons with sufficient energy when compared to atomic oxygen assuming a similar EEPF and the same electron density. To understand the mechanisms behind reactive species formation, more information is required about the energy coupling in the plasma.

3.6.3 Comparison of measured lifetimes to predicted values

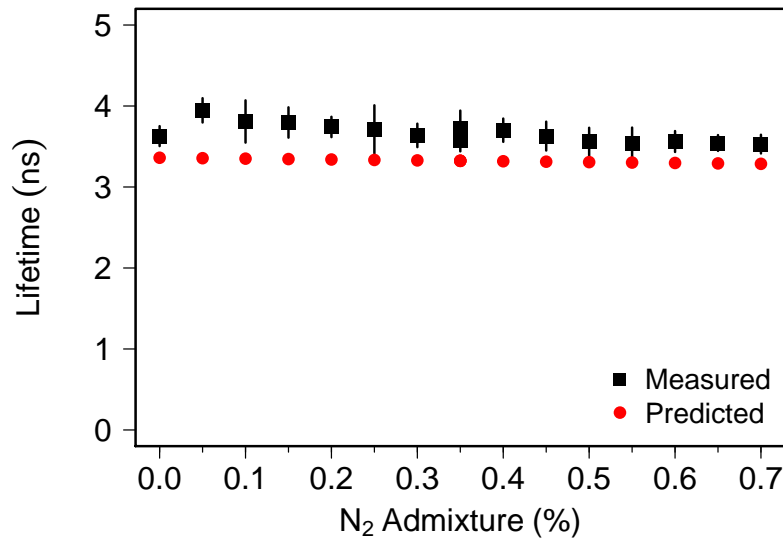


Figure 3.19: Measured and predicted lifetime of the $N(3p\ ^4S_{3/2})$ state for various admixtures of N_2 , assuming a gas temperature of 310 K to anticipate neutral gas heating [54]. Predicted values over estimate the rate of quenching, resulting in shorter lifetimes than measured.

Quenching coefficients for these simple systems, assuming that helium and molecular nitrogen are the only significant quenching partners can be predicted using values from literature. Figure 3.19 demonstrates the subtle differences that can occur in lifetime that are not represented when estimating. The measured values show a peak at small admixtures, with the lifetime decreasing with higher admixtures of molecular nitrogen. Helium quenches the $N(3p\ ^4S_{3/2})$ state at a rate four times lower than that of N_2 ($(0.11 \pm 0.01) \times 10^{-16} \text{ m}^{-3}$ compared to $(0.41 \pm 0.09) \times 10^{-16} \text{ m}^{-3}$ [88,116]), but it is much more prevalent. The result is that for additions of N_2 there is very little noticeable difference in lifetime, going from 3.36 ns to 3.28 ns when solely using the predicted quenching values. When estimating the quenching contribution, factors such as impurities and changes in temperature (therefore density) are negated, which could lead to the discrepancies observed. Overall, the estimated quenching coefficients from literature appear to be consistent with those measured in the early effluent, with only 9% over estimation of quenching on average. This gives credibility to previous studies which have used estimated values for quenching in the core μ -APPJ plasma [67].

3.6.4 Atomic nitrogen density in complex chemical environments

3.6.4.1 Synthetic air

Direct measurement of the lifetime allows for atomic species to be measured in complex plasma chemistries where the absolute combination of quenching contributions is not known. For example, this allows for measurement of atomic nitrogen in synthetic air admixtures where the multitude of species makes estimating the quenching inaccurate. Synthetic air is a 4:1 ratio of N_2 and O_2 to mimic atmospheric ratios without humidity or trace gases. It allows for the possible tailoring and control of more complex species such as NO which is a biomedical relevant molecule [75, 77, 80], and as shown is a direct result of N density.

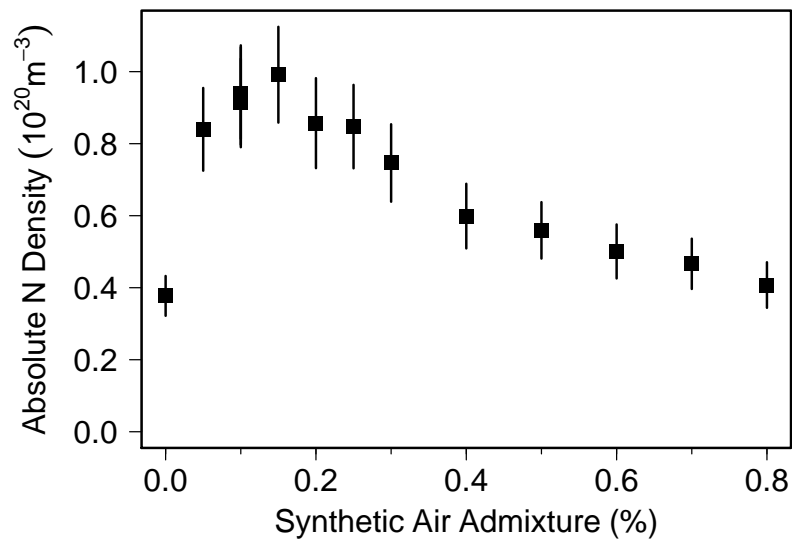


Figure 3.20: Absolute N density with varying 4:1 N_2 : O_2 admixture at a driving voltage of 425 V. The maximum N density is found at very low admixtures, and steadily decreases with increased admixture. The N density is lower for synthetic air than N_2 only admixtures.

In the past, measurement of atomic species in synthetic air admixtures has only been performed using VUV absorption [58]. The experimental implications limit these measurements to the core plasma, and is not suitable for assessing species densities in “real-world” atmospheric conditions. Figure 3.20 demonstrates the change in atomic nitrogen density as a function of synthetic air admixture, at a reasonably high operating voltage of 425 V.

Once again, the absolute N density exhibits a peak in production, however it is shifted to very small admixtures of around 0.15%. This early peak is consistent with VUV absorption measurements [58], found at 0.1% admixtures. The absolute density is an order of magnitude lower when comparing to the same applied voltage for peak production nitrogen only admixtures. Densities range from $(0.48 \pm 0.07) \times 10^{20} \text{ m}^{-3}$ to $(1.15 \pm 0.16) \times 10^{20} \text{ m}^{-3}$ for a applied voltage range of 248–425V. For lower applied voltages, as is used in VUV absorption, absolute densities agree well, with measured peak densities of $(0.57 \pm 0.04) \times 10^{20} \text{ m}^{-3}$ [58].

The addition of molecular oxygen clearly modifies the characteristic production of atomic nitrogen in the μ -APPJ, and the inevitably produced atomic oxygen may be acting as a sink for atomic nitrogen, producing secondary species. As atomic oxygen should be in abundance due to the low dissociation energy, even as a minority fraction of the feedstock gas it is not unreasonable that it could reduce the atomic nitrogen density by an order of magnitude.

3.6.4.2 Far effluent in ambient air

Measuring the lifetime also allows for measurement far in the effluent where the quenching contribution is not known due to mixing with ambient air. Using ps-TALIF offers insight into the distribution of reactive species at the point at which they would reach the treatment site, an important consideration when tailoring plasma reactive species. Predicting the flow of reactive species to biomedical substrates has been investigated using techniques such as time integrated imaging and Schlieren imaging [54, 129] measuring traditional fluid flows. TALIF can complement techniques such as flow imaging by offering a picture of how species are distributed, and reveal how mechanisms such as mixing can effect the eventual density.

Figure 3.21a shows how lifetime measurements can be spatially resolved far into the effluent region. Along the axial direction and out to the sides the lifetime drops due to incoming ambient molecular species quenching the excited state. The early effluent still contains the predominantly helium mixture that is leaving in a laminar flow (considering the Reynolds number is 200 for helium only at 1 slm). In Figure 3.21b the absolute atomic nitrogen density is given with distance both away from the jet exit (axial distance) and the radial distance outwards. Densities can not be measured accurately below 0.5 mm axially due to occlusion of the solid angle by the jet [116]. The density shows a correlation between the overall shape of the density distribution and the recorded lifetime. Three main processes are possible for reducing the density of atomic nitrogen once it leaves the plasma channel. Firstly, the measurement of lifetime indicates the entrainment of ambient species that react with the atomic nitrogen to form secondary products. The second is recombination of N with feedstock species, which may be more prevalent in the early effluent before a decent population of ambient species are present. Thirdly, diffusion and other transport mechanisms reduce the measured species densities in the far effluent.

Figure 3.22a shows the measured lifetime in the effluent of the μ -APPJ as a function of axial distance from the centre of the jet exit (radial distance = 0 mm). Measurements are made after 0.5 mm axially, as occlusion of the detection solid angle by the jet body occurs below this [116]. The lifetime down the central axis shows in more detail how ambient species mixing changes as the effluent progresses outwards from the jet towards a theoretical target surface. Lifetime measurements in Figure 3.22a show a linear rate of change, indicating a linear increase in ambient species until an equilibrium condition occurs after 4 mm and the lifetime settles to ~ 1.5 ns. In comparison, by assuming a fully mixed 4:1 ratio of $N_2:O_2$, and

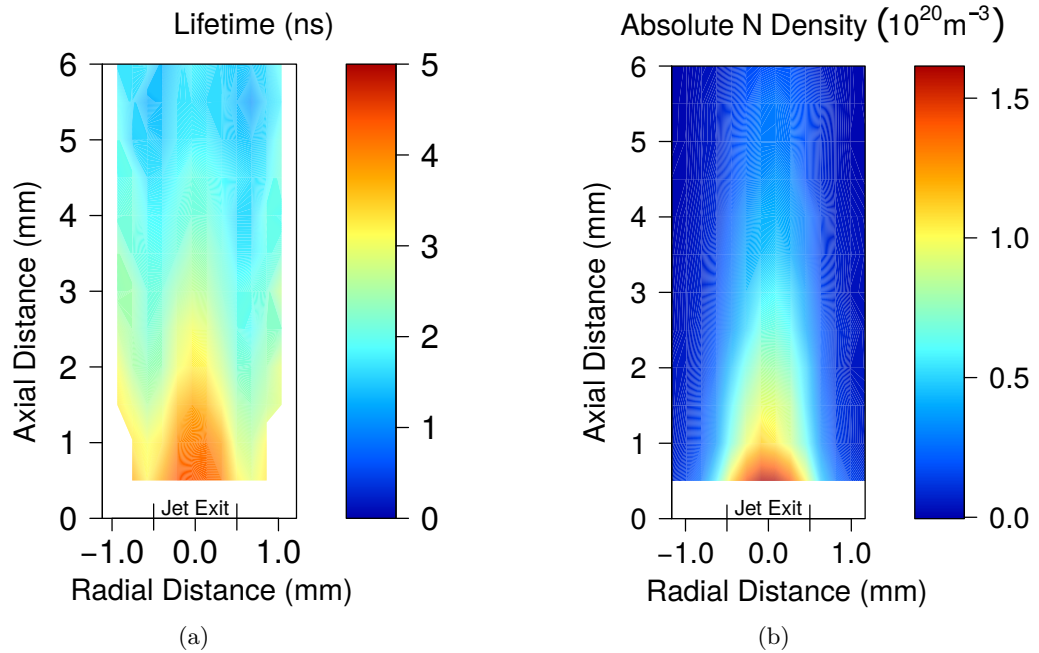


Figure 3.21: Spatial lifetimes and atomic nitrogen densities in the far effluent. (a) shows spatial distribution of the measured lifetime. Absolute densities are reported in (b) and show atomic nitrogen densities generally decreasing further from the jet exit. The jet exit is at 0,0 extending ± 0.5 mm radially.

using the quenching coefficients from [88], the expected lifetime would be 0.2 ns at 300 K, which would result in an over estimation in atomic nitrogen density by 750%. The axial density in Figure 3.22b can be approximated to a single exponential decay, which implies a single dominant rate of N destruction. The destruction of atomic nitrogen is not solely determined by ambient species entrainment. If this was the case, the rate of N destruction would be increasing as more ambient species diffuse into the effluent and to form secondary products.

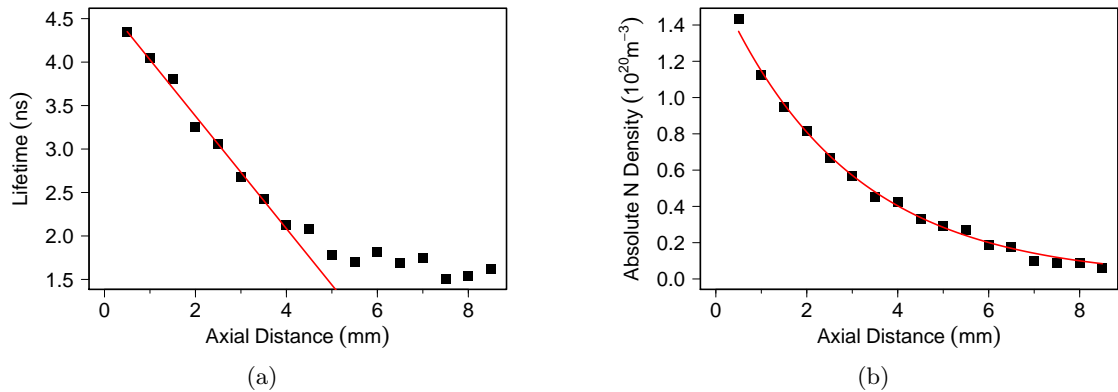


Figure 3.22: Both lifetime (a) and density (b) show steady rates of decrease as the effluent moves further into the ambient atmosphere.

Exponential loss of atomic species is known to occur [57, 60, 68] in the effluent region. For 0.3% N_2 in 1 slm, along the central axis out from the μ -APPJ there is a half-life of just under 2 mm, the equivalent of 0.12 ms. This is ten times faster than the combined dominant three-body recombinations between two nitrogen atoms and a third partner ($N + N + M = N_2 + M$, where M is He, N_2 , or N) [63, 67, 68, 70]. As the rate appears invariant with ambient species mixing, nor consistent with recombination, fluid effects may determine species densities. Kelly *et al.* [66] performed 2D fluid modelling of the μ -APPJ to spatially resolve oxygen species densities (such as O and O_3) in the effluent region. Atomic oxygen shows a similar half-life of 2.5 mm, which is much shorter than recombination alone.

From simulations and spatially resolved ps-TALIF, it can be postulated that fluid effects do play a role in the distribution of reactive species. More importantly the reactive species densities reaching a target surface should be proportional to the core reactive species densities, but with a relationship that can not be assumed merely through using recombination. Estimation of treatment site species densities require explicit measurement with techniques such as TALIF or with complex 2D or 3D fluid and chemistry modelling.

3.7 Summary

Atomic nitrogen can be measured using two-photon absorption laser induced fluorescence successfully in the previously unknown effluent region of the atmospheric pressure plasma jet. This effluent region is ultimately the interaction point between reactive species from the jet and a treatment site, and knowledge of specific densities is of importance to those wishing to utilise the jet for specific tasks. The use of ps-TALIF has enabled greater insight into real-world applications of the micro-atmospheric pressure plasma jet.

Measuring the excited state lifetime directly has however confirmed that the typical quenching coefficients used from literature are valid at atmospheric pressure. This adds credibility to previous measurements of atomic nitrogen density in simple chemistries in the core plasma using nanosecond TALIF systems, whereas before this study there had been some doubt over the reliability of quenching coefficients at elevated pressures.

It is possible to tailor the density of atomic nitrogen through choice of admixture, with the peak production found between 0.25 % and 0.35 %, inline with previous estimates. Values can be further tailored by changing the applied voltage, from less than $(0.7 \pm 0.1) \times 10^{20} \text{ m}^{-3}$ to $(10.6 \pm 1.3) \times 10^{20} \text{ m}^{-3}$. With the appropriate admixture and driving voltage, two orders of magnitude on the density are available, equivalent to a range of 3 ppm to 40 ppm. These densities at 0.25 % admixture equate to dissociation fractions ranging from 0.1 % to 1.4 %.

The unique ability to measure into the far effluent has revealed that atomic nitrogen density at a given distance is governed not only by the surrounding chemistry, but also the fluid effects associated with the μ -APPJ expelling effluent into open atmosphere. This atomic nitrogen in the effluent can then go on to produce other biologically relevant species such as NO, and understanding the production of atomic nitrogen has allowed for insight into where more complex chemistry is formed. Formation of more complex molecules from plasma sources is still a large topic of investigation, and the results shown will aid in that discussion.

The underlying plasma dynamics underpin the mechanisms for tailoring reactive species such as atomic nitrogen. Changing parameters such as gas composition and applied voltage offers crude control over the reactive species density, however further understanding of the electron dynamics can provide knowledge to further tailor plasmas for their intended application. This leads to the need to estimate power being deposited in the plasma reliably.

Chapter 4

Measuring Plasma Power and Operating Modes

Measurements of plasma power can help diagnose the state of an RF plasma, as it is linked to the electron density, and the electron temperature. For the μ -APPJ, measurement of power is already an important subject [12, 56]. In order to accurately compare plasma devices, energy efficiencies, and experiments to simulations between different institutions and operating regimes, it is essential to measure the plasma power. Despite its utility, in reality plasma power is often not reported, as it can be difficult to measure accurately in small RF APPJs. It has been argued by some researchers [7–9] that a lack of reliable measurements of plasma power in the μ -APPJ not only causes issues when comparing experiments and devices, but ultimately hinders fundamental research. For the μ -APPJ, the COST reference jet, and other small atmospheric RF plasma devices to be characterised effectively, the plasma power needs to be measured for various operating parameters, including driving voltage and molecular admixture.

4.1 Measuring power in AC circuits

To measure power in an AC circuit, the integral of the voltage V , and current I is taken, as shown in Equation 4.1. Typically the integration is made over one period T .

$$P = \frac{1}{T} \int_0^T V(t)I(t) dt \quad (4.1)$$

Considering $V(t)$ and $I(t)$ in an RF situation are sinusoidal, they can be written as $V(t) = V \cos(\omega t)$ and $I(t) = I \cos(\omega t + \theta)$ respectively, where θ is the phase shift between them, and ω is the angular frequency ($\omega = 2\pi f$). The phase shift can be visualised as voltage and current leading or trailing one another in time, as shown in Figure 4.1. Using a product-to-sum trigonometric identity, the integral becomes

$$P = \frac{VI}{2T} \int_0^T \cos(2\omega t + \theta) + \cos(\theta) dt$$

and by substitution of $T = 2\pi/\omega$ for one period, results in time-averaged power of

$$\bar{P} = \frac{VI}{2} \cos(\theta) \quad (4.2)$$

for a sinusoidal voltage and current with amplitudes V and I respectively.

Equation 4.2 is often written without the factor of $1/2$, using the root mean squared (RMS) value of voltage and current instead ($RMS = \text{amplitude}/\sqrt{2}$). This can lead to confusion, and accordingly voltage and current values in this text are reported as amplitude.

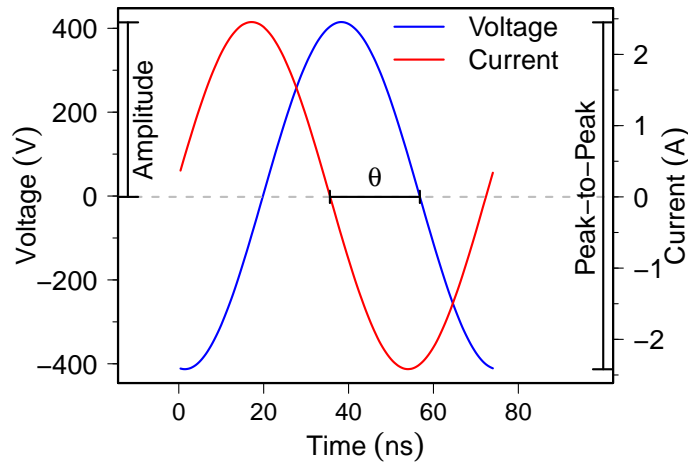


Figure 4.1: Example of observed sinusoidal voltage and current waveforms for the μ -APPJ, with phase shift θ between them.

To calculate time-averaged power, three components are required: amplitude of voltage, amplitude of current, and the phase between them. By applying some test cases to Equation 4.2 it is possible to understand how power is dissipated in AC circuits. For purely resistive

circuits, when voltage and current are in phase and $\theta = 0$, all the possible power is dissipated in the system and Equation 4.2 further reduces to what it recognised in DC systems. For purely inductive systems $\theta = \pi/2$, therefore $\cos(\pi/2) = 0$, in this scenario no net power is dissipated in the system. The same case is found for purely a capacitive system, as $\cos(-\pi/2) = 0$.

In reality no AC circuit is purely capacitive or inductive, and the resultant Power Factor, the common nomenclature for $\cos(\theta)$, is close to but not equal to zero. In these reactive regimes, where cosine has large gradients, small changes in the phase angle lead to large changes in the power factor. Conversely, in a very resistive circuit, cosine is near its maximum and the power factor is at unity. Large changes in phase angle now produce very small changes in the power factor meaning it remains close to unity. In reactive systems, measurement of phase can be the largest source of error.

4.1.1 Impedance

In an AC system, such as an RF circuit, impedance Z is used in place of traditional DC resistance R , though both are measured in ohms (Ω).

$$Z_R = R \quad (4.3)$$

$$Z_L = i\omega L \quad (4.4)$$

$$Z_C = -i\frac{1}{\omega C} \quad (4.5)$$

The impedance of resistors Z_R is expressed simply as net resistance, with no dependency on frequency. For inductors, reactance Z_L is given by the product of angular frequency ω and inductance L . For capacitive reactance Z_C , it is the reciprocal of the product of frequency and capacitance C . As frequency increases, inductors play more of a role, and conversely capacitors affect the system less. To calculate the impedance, the vector addition is taken of all three, with the reactive parts (represented by X) multiplied by the square root of minus one i .

$$Z = Z_R + Z_L + Z_C \quad (4.6)$$

$$Z = R + iX \quad (4.7)$$

The capacitive and inductive impedance are in imaginary forms, as they take energy from the circuit, but then give it back, resulting in no net loss of energy. These interactions do however change the phase between voltage and current. Total impedance Z can be written in terms of a complex number (see Equation 4.7). As impedance is a complex number, it can be expressed using an Argand diagram. As shown in Figure 4.2, impedance is a vector

with magnitude $|Z|$ and direction θ . For a purely resistive system, $\theta = 0$, whereas for purely capacitive or inductive components the phase angle is $-\frac{\pi}{2}$ and $\frac{\pi}{2}$ respectively. This means that $-\pi/2 \leq \theta \leq \pi/2$.

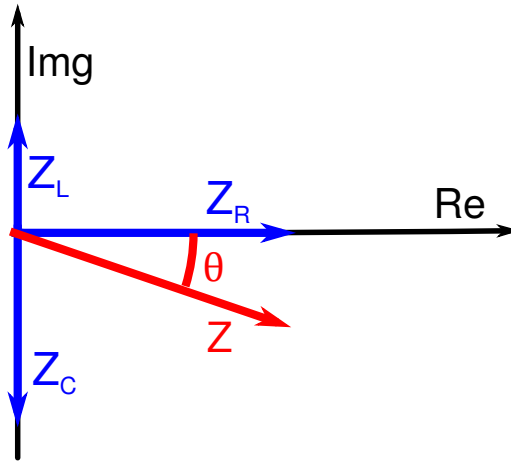


Figure 4.2: Argand diagram demonstrating impedance of different components. The resultant impedance is a vector with magnitude $|Z|$ and direction θ .

4.2 Approximating plasmas as circuits

The plasma, the physical device comprised of electrodes and windows, as well as the associated cables and connections to a power supply, can all be modelled with an appropriate electric circuit model. The system can be described as series and parallel arrangements of resistors, capacitors and inductors. Often it is more convenient to ‘lump’ certain aspects of the system together. When measuring plasma power, it is convenient to separate the plasma components from the additional system components. As well as the known components, there are unknown components referred to as ‘strays’ or ‘parasitics’. These are typically unknown losses that arise from the physical system, and can be something as simple as the fact the plasma device must be mounted to a table, offering different capacitive paths to ground. These strays are also lumped together. Circuit models of the plasma themselves vary depending on if they are time dependent, or time-averaged. They also are tailored with respect to the operating parameters such as pressure. Collisional and collisionless plasma models will handle interactions differently, but despite this, plasmas can still be generalised as a time-averaged circuit describing the bulk plasma and sheath [1, 16].

A basic time-averaged circuit model for a symmetric capacitively coupled plasma [16] is shown in Figure 4.3. Power in the plasma bulk is dissipated ohmically through electron-neutral collisions [1, 16], represented by R_P . The electrons resist the changing electric field to some degree through their inertia, this is represented as an inductance L_P . As discussed in Chapter 2, the electrons are considered highly mobile with respect to the driving frequency

despite more collisions at high-pressure, and so this term is usually small. The sheath is in essence a space charge, which a capacitor describes appropriately, represented by C_S . In the sheath region there is energy dissipated into ions, along with electrons through both ohmic and stochastic heating, represented by R_S .

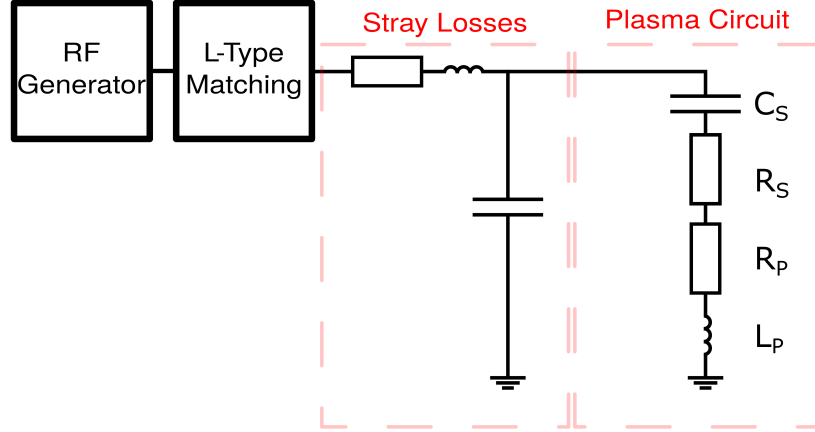


Figure 4.3: Plasmas can be approximated as a collection of electrical components based on the physical properties of the bulk and sheath. The sheath region acts as a capacitor, as well dissipating energy. The bulk plasma dissipates energy predominantly ohmically, with the electrons imparting some inertia into the system, modelled as an inductor. Parasitic losses or strays, lead to power being dissipated elsewhere in the circuit.

For a high-pressure capacitive discharge, it is expected that the dominant energy deposition process is through electrons heated by strong electric fields created in the bulk plasma during time periods when the RF current is maximum [16, 130–133]. These fields arise in order to drive the required current across the discharge gap and maintain current continuity. This heating is collisional in nature meaning any collisionless heating can be neglected in atmospheric-pressure plasmas.

At greater driving voltages, it is expected that the sheath potential can begin to greatly heat ions that enter the sheath through collisions [16, 65]. With addition collisional heating from the sheath, the circuit model is expressed as a series combination of bulk resistance (R_P), sheath resistance (R_S), and sheath capacitance (C_S).

A parallel plate capacitor can be specified in terms of plate area A and plate separation d . To calculate the capacitance, the permittivity of free space ϵ_0 and the dielectric constant of the interelectrode material ϵ_r are also required.

$$C = \epsilon_r \frac{\epsilon_0 A}{d} \quad (4.8)$$

Between helium and air, the difference in dielectric constant is negligible, and can be assumed as unity for both [134]. When the plasma is ignited, the capacitance of the plasma channel is replaced with the equivalent of the components that the plasma can be approximated to. Modelling the sheath as a capacitor, the plate separation d is better described

as sheath thickness S_m , which in turn is a function of various plasma parameters [1, 16]. It should be noted that the capacitance of the sheath also has a factor analogous to the dielectric constant.

The bulk plasma can be defined as having a width that is the electrode gap spacing minus the maximum sheath extent for the powered and grounded side ($1\text{ mm} - S_m$). In essence, the bulk properties are linked to the sheath properties, and the sheath properties are connected to the bulk properties. Together they form an equilibrium, with the resistive and capacitive parts shedding light on the state of the plasma. This concept of the plasma being modelled as electrical components will be of use later when examining how power is coupled into the plasma, and how the plasma dynamics change as a result.

4.3 Strategies for measuring plasma power

In low-pressure systems, the plasma and its chamber are normally the dominant electrical system, and the power lost into parasitics and matching is small compared to the plasma power [25] (though they are still important to characterise). The power dissipated in atmospheric-pressure plasma jets on the other hand can be very small when compared to the losses in the total system. In low-pressure systems, reporting the power from a generator is usually sufficient, as the losses in a well designed system are negligible, this is not the case for APPJs. When measuring power in an APPJ, it is desirable to measure after the matching box to remove as many unknown losses as possible. Unfortunately, this often means that when measuring plasma power, the phase angle measured is close to $-\pi/2$, creating the possibility for large errors.

Godyak [135] conveniently outlines some useful strategies for measuring plasma power. They are based on measuring voltage and current simultaneously with an oscilloscope for real time estimation of plasma power.

For more transient plasmas where the electrode voltage is not sinusoidal or contains considerable harmonics, for example in pulsed plasmas, it is more useful to perform the integration of voltage and current directly using Equation 4.1. This integration is simple to achieve on a modern digital storage oscilloscope (DSO), but in practice this method usually has the highest degree of uncertainty [135]. When using well behaved sinusoidal voltages, Equation 4.2 can be used directly, where losses in the ancillary circuitry are deemed to be negligible, and the plasma dissipates nearly all the power. To negate losses, this method is used as close to the electrodes as possible. Unfortunately, the oscilloscope as well as the cabling and electronics for the voltage and current probes induces a small amount of unwanted measured phase shift, known as instrumental phase θ_i .

At 13.56 MHz, the period is $\simeq 73.75$ ns. A typical mid to high end modern DSO will have a sample rate on the order of 10 GSa/s, the equivalent of a 0.1 ns sampling interval, which yields 0.5° between samples. Instrumental phase can be removed in real time by skewing (shifting one waveform with respect to another on the oscilloscope in time) and performing the maths required on the scope [136]. Unfortunately, at extreme phase angles, this results in unacceptable uncertainties. Using $\pm 0.5^\circ$ angle as a metric, at -89° , this yields an uncertainty of $\pm 50\%$ in the power factor when skewing by integer time steps. This error becomes linearly worse when considering slower sample rates or higher driving frequencies.

Another technique used to estimate plasma power is the ‘subtractive’ method. The subtractive method addresses both the issue of losses, and the issue of measuring phase. A commercial power meter is placed pre-matching where conditions are close to 50Ω ; removing the uncertainty that comes with measuring phase accurately. Power dissipation is measured with and without plasma for the same applied voltage or current, and the difference between the two is taken as the plasma power [135, 137]. Without a plasma running, this technique

measures dissipated power in the rest of the system, and this value can be subtracted from the total when the plasma is running. This technique shows the smallest uncertainty [135] between the various methods. Despite this, for use with the μ -APPJ some modifications need to be made to reduce uncertainty further.

As mentioned in Chapter 2, high frequency RF generators are designed to operate into a $50\ \Omega$ load. This means any reactive parts must be cancelled out to leave an impedance of $50\ \Omega$ at a zero phase angle. Any deviation from this leads to standing waves forming in the system, and reflected waves travel back into the generator. Though most generators are designed to tolerate some amount of reflected power as a safety precaution, it is not a desired mode of operation, and can ultimately cause permanent damage. The physical design of capacitively coupled plasmas resembles that of a capacitor, two electrodes separated by a gap. This capacitance has to be cancelled out by a shunt (parallel) inductance. This inductance is usually in the form of a matching box. Matching boxes offer impedance matching to $50\ \Omega$ for the generator (allowing maximum power transfer), whilst downstream of the matching box can in fact be far from $50\ \Omega$.

Matching boxes, though important in maintaining maximum possible power transfer, introduce losses into the system. A well matched narrowband L-type with high quality components may result in just a few percent power lost between input and output, but this degrades rapidly when matching is poor. Broadband Π -type matching however can introduce losses of up to 90% [138] but over a large range of impedances. The compromise that must be made is between flexibility and performance, usually once a design and operating regime for a plasma system is known, an L-type matching unit is preferred. Previous estimates of power dissipation in APPJs have been performed [11, 136]. In these studies an inductive shunt has been utilised in place of a traditional matching network. This technique attempts to minimise the number of component losses, and helps cancel out the capacitive nature of the plasma device, resulting in a resistive only load, bringing phase angles closer to zero. While helping to remove some of the error when measuring phase, it however introduces some limitations.

Firstly, specialised inductive components must be manufactured, and this is not always possible, nor desired if wanting to operate with a traditional matching network. Secondly, the inductive components themselves still have losses analogous to a matching box. For example, the coupler design used by Marinov & Braithwaite [11], can lead to considerable heating, and therefore losses, if matching is poorly maintained. Thirdly, when using a commercial power meter (Impedans OCTIV VI probe) in a pre-matching configuration, non-physical results were found, such as negative plasma powers for the μ -APPJ. This behaviour has been observed in other systems [25]. The losses in the APPJ system are too great, and variations in the quality of matching are enough to impede this method from working. Instead of pre-matching, the measurement of power in the μ -APPJ must be made post-matching.

Commercial probes are nearly always designed and calibrated for pre-matching into a $50\ \Omega$ load, traditionally for antennas and low-pressure systems where the accuracy of phase is not as important as for the μ -APPJ. This lack of accuracy at extreme phase angles in a post-matching configuration can lead to powers some orders of magnitude greater than the input power from the generator. This non-physical measurement of plasma power greater than the source generator power has been seen before in other atmospheric devices [139]. This inadequacy in some plug-and-play commercial probes results in the need for bespoke treatment of phase angle, where it must be measured accurately and with as high a precision as possible.

4.3.1 Treatment of phase angle

Phase angle can be measured in three broad ways. Sinusoidal functions can be fitted to the voltage and current waveforms, and their relative phase then measured. Fitting sinusoidal functions however is tricky, with many local minima that can halt fitting procedures, and therefore need very good starting parameters. Fitting for amplitude, phase and frequency leads to a large parameter space, with a very small probability volume in which the global minima occurs. It also necessitates the use of mathematical tricks to constrain variables such as phase which are cyclic. This results in very time consuming computation, and Bayesian approaches perhaps become more favourable for many reasons, rather than traditional least squares style regression. A faster approach is to measure zero crossing points, and interpolate the zero point in time, then taking the mean time between zero crossings. If the signal is noisy, then this zero crossing technique becomes very difficult. Though computationally rapid, it is to be avoided for all but near perfect signals with very little harmonic content. The most rapid and reliable method is to perform a fast fourier transform (FFT) [135,140] on the voltage and current waveforms.

The complex result from the FFT yields the phasor against frequency for each waveform. With a great enough number of data points, a near integer number of cycles, and a sufficient sample rate greater than the Niquist frequency, the resolution can be great enough to select out the driving frequency only. At this frequency, the amplitude and relative phase can be extracted from the FFT using the modulus and argument of the complex number respectively. To measure the relative phase between the voltage and current signals, the difference between their individual phases is taken, thus fulfilling the required values needed for Equation 4.2.

4.4 A method to measure plasma power in the μ -APPJ

The method used is based on the subtractive method, to try account for parasitic losses which are still a major concern even though the lossy matching box has been negated by measuring post-matching. Analysis is undertaken with post-processing to ensure a proper treatment of the phase angle. The required measurement of phase and subsequent calibration unfortunately does not lend itself readily to real-time power measurements.

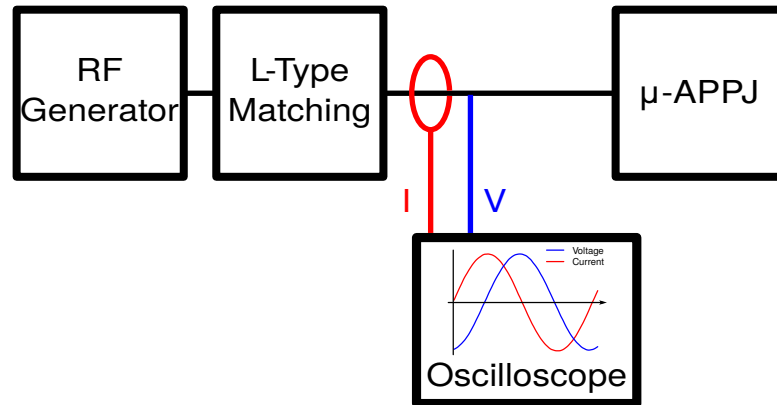


Figure 4.4: Schematic of power measurement experiment. Probes are placed post-match, between the matching network and the μ -APPJ. Voltage and current are recorded using an oscilloscope.

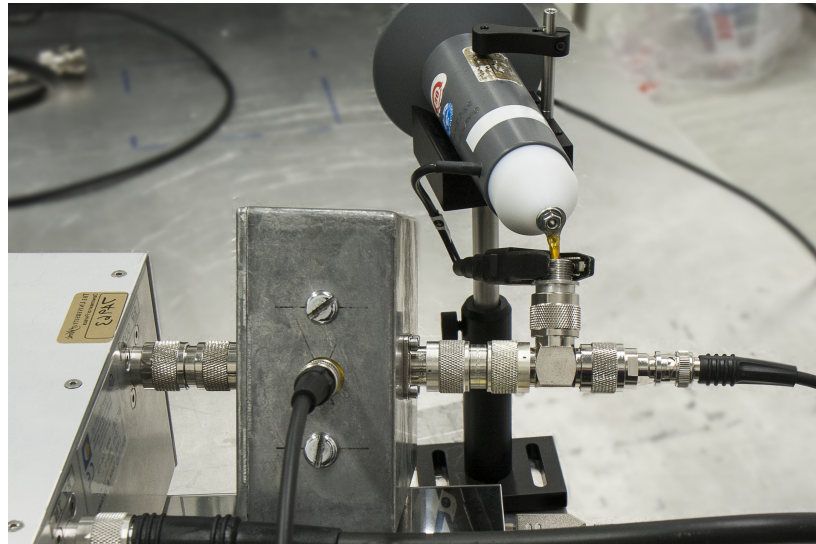


Figure 4.5: Photograph of V and I probes. Left to right is the L-type matching unit, the current monitor (mounted in an aluminium case), and voltage probe, with the final connection leading to the μ -APPJ.

Figure 4.4 shows a schematic of the experiment. An Ion Physics Corp. CM-100-L (1 V/A 100 MHz 20 A) current monitor is placed directly after the output of the L-type matching network. In shunt is a PMK 4002 (1000:1 100 MHz 20 kV) passive high voltage probe. This can also be seen in Figure 4.5. The voltage measured after the current probe was compared to the voltage measured simultaneously at the μ -APPJ electrodes, and found to be the same, indicating negligible voltage drop along the transmission line. Not only does having the voltage probe upstream allow a more robust physical configuration, it does not restrict optical access to the plasma, which is important for optical diagnostics. Moreover, as will be discussed later, it allows for a far simpler calibration procedure. The probes are connected to a LeCroy WaveRunner 204MXi-A (8 bit, 2 GHz, 10 GSa/s).

Channel interleaving is a common technique on oscilloscopes to save Analogue-to-Digital Converter (ADC) resources, effectively reducing the sample rate per channel in favour of more channels being measured. For example the 4 channels on the LeCroy 204MXi-A share two 10 GSa/s ADCs, one for channels 1 and 2, and one for channels 3 and 4. Sample rate can be maximised by using for instance channels 2 and 3, which each have a full ADC to utilise, rather than channels 1 and 2 which share an ADC and the sample rate must be split between them. Though the ramifications of channel selection would not normally be considered, as shown in Section 4.3, any increase in sample rate is appreciated when considering the possible error in phase.

4.4.1 Plasma on

Waveforms for voltage and current are recorded for the desired operating parameters when the plasma is active. These waveforms are recorded for a time series over 100 RF periods in length, at the fastest sample rate possible. The waveforms are averaged to help reduce non-correlated noise. When the plasma is ignited the appropriate voltage and current range to use on the oscilloscope can be selected, along with the voltage and current range that needs to be measured when the plasma is off. The power dissipated is the sum of the support circuitry system and the plasma.

4.4.2 Plasma off

The μ -APPJ is filled with air, and consequently breakdown cannot occur. In this case, energy is being dissipated in the remaining support circuitry only. The input power from the generator is incremented over a span to give a response of voltage and current that is similar to when the plasma was on. As the circuitry is invariant with input power, the power factor $\cos(\theta)$ is expected to remain constant. A simple $P = I^2 R$ relationship can be found as an outcome, and therefore plasma off power can be estimated for any driving current. The same can be made for voltage also, using $P = V^2/R$.

4.4.3 Calibration

As mentioned previously, the instrumental phase θ_i causes a measurable difference in the perceived and true phase angle of the system. This error in phase angle leads to an error in the measured power. By using a circuit with a known phase, any instrumental shift can be removed in post-processing.

The μ -APPJ resembles a capacitor, and when the plasma is on, the phase angle change is small enough for the circuit to still remain mostly capacitive. It makes sense then to use a capacitor for phase calibration, where the reactive part is far more dominant than the resistive part, resulting in an angle close to -90° . It has been shown that calibrating to an environment that matches the load under scrutiny reduces error considerably when considering a transmission line error model [140]. A Meiden SCV-155GT variable vacuum capacitor, and an MFJ 282-2018-1 variable air capacitor were used as standard components to calibrate the system to. These were characterised by using a HP 8714ES Vector Network Analyser, as well as a SARK-110 Antenna Analyser.

By having the current and voltage probes together, it is experimentally simple to replace the μ -APPJ with the standard component, while maintaining the same instrumental phase for all scenarios. Using a vector network analyser the true phase of the capacitor is given, for example $\theta = -89.6^\circ$ for the MFJ 282-2018-1. The phase angle between the voltage and current can be found by taking the argument of the complex number at the driving frequency for each, and taking the difference between them. When calculating the relative phase using FFTs in post-processing, as described in Section 4.3.1, a typical measured angle could be $\theta_m = 50.2^\circ$ between voltage and current. Rearranging Equation 4.9, the instrumental phase θ_i would be taken as 148.8° . This value can be used for all post-processing to find the true phase angle θ from the FFTs.

$$\theta = \theta_m - \theta_i \quad (4.9)$$

For as long as the physical position of the probes is undisturbed, as well as the cabling and settings on the oscilloscope (mainly volt/div selection), this calibration factor should be constant, though it is advisable to repeat periodically. When changing volt/div, the internal relay circuitry in the oscilloscope can induce a change in the instrumental phase. In some cases it has been measured to be 1 ps (LeCroy HDO6054). Though this is small percentage of the sample time, it is enough to be readily seen as a change in calculated power at extreme phase angles, especially at high frequencies investigated in this work. It is of utmost importance to keep these settings consistent for the plasma on, plasma off, and calibration cases.

4.4.4 Calculation

Once the plasma power has been calculated for the phase corrected plasma on and plasma off conditions, the two are subtracted as per Equation 4.10.

$$P_{plasma} = P_{on} - I^2 R_{off} \quad (4.10)$$

The comparison is made for the same current, as to include any thermal losses [11, 136], an example can be seen in Figure 4.10a.

4.4.5 Error estimation

4.4.5.1 Systematic errors

As well as a conservative estimate of $\pm 10\%$ error on the voltage and current readings, there is the error in phase to consider. When sampling the voltage and current, the jitter between channels on the oscilloscope can be taken as negligible when compared to the error possible in the calibration due to the instrumental phase.

When cosine is at extreme angles, it behaves as sine in the small angle approximation, i.e. $\cos(\theta \sim -\pi/2) \equiv \theta + \pi/2$. Consider a δ systematic inaccuracy in θ that arises from a inaccurate calibration.

$$\begin{aligned} P &= P_{on} - P_{off} \\ P &= \frac{IV_{on}}{2} \cos(\theta_{on} + \delta) - \frac{IV_{off}}{2} \cos(\theta_{off} + \delta) \end{aligned}$$

Using the small angle approximation for cosine,

$$P = \frac{IV_{on}}{2} \left[\left(\theta_{on} + \frac{\pi}{2} \right) + \delta \right] - \frac{IV_{off}}{2} \left[\left(\theta_{off} + \frac{\pi}{2} \right) + \delta \right]$$

the measured power is given by,

$$P = P_{plasma} + \frac{I\delta}{2} (V_{on} - V_{off}) \quad (4.11)$$

and the discrepancy due to calibration error is $\frac{I\delta}{2} (V_{on} - V_{off})$.

For the values of current and voltage in Figure 4.10b, a miscalibration of 0.5° when calculating only the power when the plasma is operating, without calculating the power when the plasma is not operating would yield 50% error. By measuring power for both when the plasma is on and off, this miscalibration now equates to $< 1\%$. This reduction in error can be conceptualised by imagining that the large error that exists on both the plasma on and plasma off measurements are to some extent cancelled out. The subtraction method

allows for this reduction in error at extreme phase angles, only if the inter channel jitter is assumed much smaller than δ , and δ is consistent for all measurements.

4.4.5.2 Stochastic errors

Most investigators are more familiar with performing fast fourier transforms rather than performing Bayesian analysis. Bayesian analysis gives an inference of both systematic and stochastic errors for free, whereas errors from fourier transforms are rarely discussed. As performing an FFT is a faster and more accepted practice for obtaining the amplitudes and phases of voltage and current, a discussion of estimating the stochastic error inherent in the FFT is undertaken here.

When performing an FFT the collected time series is transformed into the frequency domain, with each component frequency expressed as a complex number which can yield the amplitude and instantaneous phase as mentioned in Section 4.3.1. In the time series, there is the true signal which has noise added to it. When performing the fourier transform, this can be expressed as the fourier transform of the true signal, in addition to the fourier transform of the noise, as performing the fourier transform is linear.

The resulting complex vector is the simple addition of the true signal and a vector due to random noise. This is conceptualised in Figure 4.6. This deviation in the complex plane can lead to changes in both amplitude and phase. In the test case that the signal to noise ratio (SNR) is very low ($SNR < 1$), the error is dominant, and the probability for the measured phase is equal from $0 - 2\pi$. As the SNR becomes very large, the effect the noise plays on the resultant vector becomes smaller, until the probability for the measured phase approaches the true value.

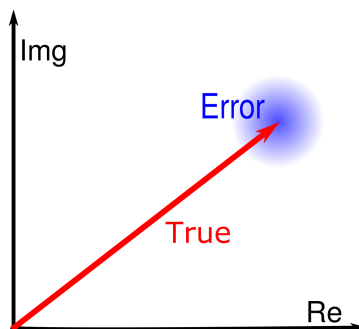


Figure 4.6: The complex result of an FFT has a magnitude and direction in the complex plane. The vector is the addition of the true signal and some error that comes from inherent noise. The resultant measured vector lies in the probability distribution which is Gaussian. Values closer to the true signal are more likely than those far away.

Regardless of the distribution of noise in the time domain, any truly random stochastic noise reduces to be normally distributed in the Fourier domain due to the central limit theorem. The resulting noise (and therefore possible error) on both phase and amplitude is in fact Gaussian and can be estimated from functions based on the noise to true signal ratio.

From an example FFT for voltage time-averaged over 128 iterations (Figure 4.7a), the magnitude at 13.56 MHz is five orders of magnitude greater than the noise present. The noise (Figure 4.7b) is fitted to a Rayleigh distribution, which is expected for data of this nature. As the magnitude is a function of both the real and imaginary component, but the two are uncorrelated, the result is a Rayleigh distribution. This uncorrelated nature to the noise is a key assumption when computing the possible error in both magnitude and phase, and a check of this is necessary.

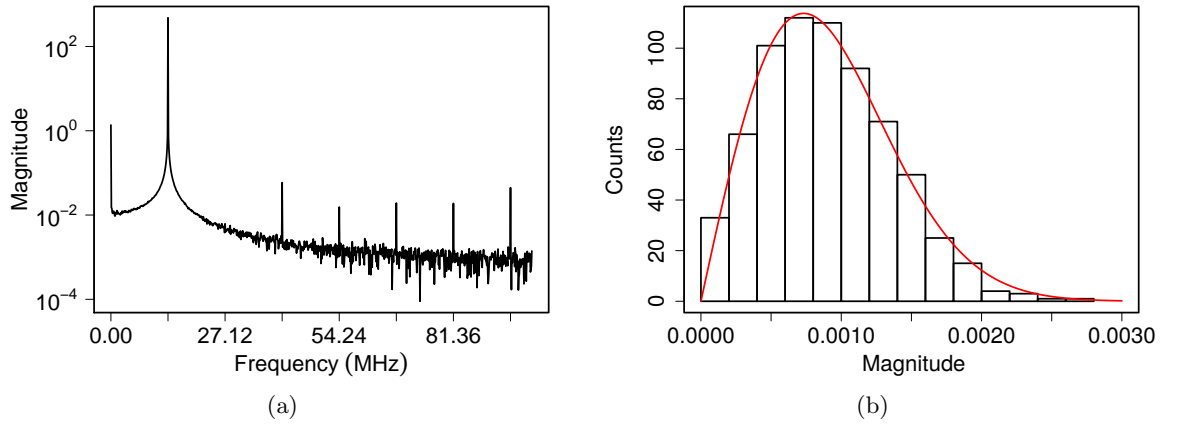


Figure 4.7: (a) Example FFT of voltage for μ -APPJ. (b) histogram of noise magnitudes fitted with Rayleigh distribution. The signals used are many orders of magnitude larger in magnitude compared to the noise contribution.

The error for phase and magnitude is dependant on the ratio between the true signal magnitude $|S| = \sqrt{\text{Re}^2 + \text{Im}g^2}$ and the standard deviation of the Fourier noise σ . As stated earlier, stochastic noise will become Gaussian in the Fourier domain, the standard deviation for the Fourier noise σ for a large number of samples becomes,

$$\sigma \simeq \sqrt{\frac{\langle x^2 \rangle}{2}} \quad (4.12)$$

where $\langle x^2 \rangle$ is the mean of the squares of the noise magnitudes.

The Rice Distribution [141] yields the probability of a measured magnitude $|M|$, given a true signal magnitude $|S|$ and the Fourier noise standard deviation σ . Returning back to the concept in Figure 4.6, this reflects the change in only the magnitude (which in this case is the amplitude of voltage or current required to calculate the power). The Rice Distribution gives a probability distribution of expected measured magnitudes $|M|$ with respect to the

true signal magnitude $|S|$ and Fourier noise standard deviation σ , where I_0 is the modified zeroth order Bessel function of the first kind.

$$P(|M| \mid |S|, \sigma) = \frac{|M|}{\sigma} \exp\left(-\frac{|S|^2 + |M|^2}{2\sigma^2}\right) I_0\left(\frac{|M| |S|}{\sigma^2}\right) \quad (4.13)$$

If the measured magnitude at the frequency of interest is large when compared to σ , $|M|$ approximates to the true signal $|S|$. In the limit of $|S| \gg \sigma$ by taking the second derivative with respect to $|M|$ at centre $|S|$, it can be shown that the Rice Distribution reduces down to a simple Gaussian $\mathcal{N}(|S|, \sigma)$. This is an expected result, in that the probable value of the measured magnitude $|M|$ is a Gaussian centred about the true magnitude $|S|$ with standard deviation σ . Therefore estimated error in amplitude could arguably be taken as 3σ .

To estimate the error in phase, which is arguably the most crucial for this application, a usually nameless distribution [142] is given below in Equation 4.14.

$$P(\Delta\phi|\text{SNR}) = \frac{1}{2\pi} \exp\left(\frac{-\text{SNR}^2}{2}\right) \left[1 + \frac{\sqrt{\pi}}{2} Q \exp(Q^2) (1 + \text{erf}(Q))\right] \quad (4.14)$$

$$Q = \frac{\text{SNR} \cos(\Delta\phi)}{\sqrt{2}}$$

This distribution describes the probability distribution of the error in phase $\Delta\phi$ with respect to the SNR. In the limit of a large ratio between true signal and the Fourier noise standard deviation, Equation 4.14 reduces down dramatically to leave Equation 4.15.

$$\Delta\phi \simeq \frac{1}{\sqrt{1 + \text{SNR}^2}} = \frac{\sigma}{|S|} \quad (4.15)$$

For the example FFT in Figure 4.7a, the value for $\sigma \sim 7 \times 10^{-4}$, where as the value for $|S|$ at 13.56 MHz is $\sim 5 \times 10^2$. The resultant expected error in the magnitude and phase is negligible when the signal to noise ratio is high, in this case $|S|/\sigma = 10^6$.

Figure 4.8 demonstrates the possible error in phase that can arise due to uncorrelated noise on top of the true signal. For single shot time series where the signal to noise ratio is smaller ($|S|/\sigma = 10^3$), there are clear deviations from the time-averaged values. Though the error in phase is appreciable, the deviation in magnitude (i.e. the value for applied voltage) is very small and nearly indistinguishable at this resolution. A typical error for signal shot magnitude is only 0.08 %, however the error in phase angle is 0.05° , an equivalent 6 % stochastic error in power factor. Averaging, even if only a few tens of time series, greatly reduces the uncorrelated noise and the evaluation of phase.

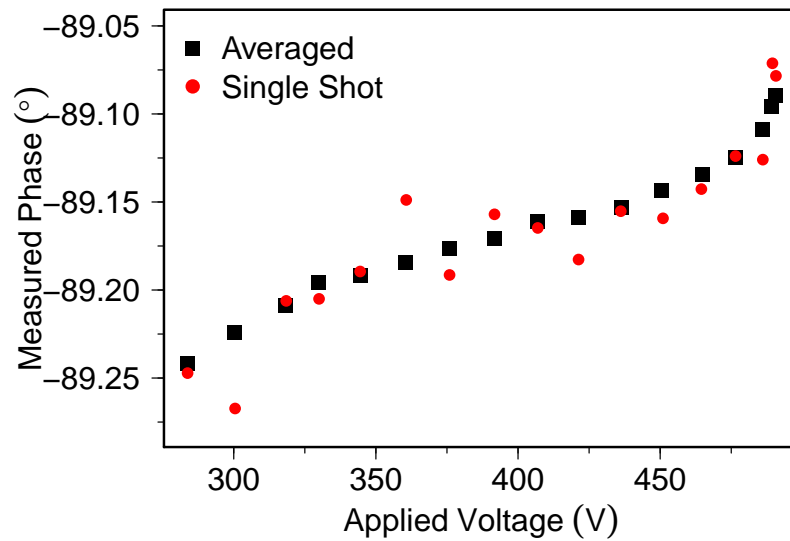


Figure 4.8: The calculated phase for single shot and averaged time series waveforms. The single shot values exhibit discrepancies from the averaged values with varying severity. These errors in phase can cause large errors in the eventual calculated power.

4.4.6 Proof of concept

To test the method, a larger modified version of the μ -APPJ was used. It is a sealed system with an electrode area eleven times greater than that of the μ -APPJ but with the same 1 mm electrode separation. A diagram of the Large APPJ can be seen in Figure 4.9. It has been designed and used primarily for VUV absorption spectroscopy [58], and requires the system be completely sealed with the gas inlets and outlets being connected via tens of centimetres of stainless steel pipework. The plasma is larger in volume, and should dissipate more power, and therefore the power should be easier to measure when compared to parasitics. This larger jet, as well as being experimentally more forgiving, is also a better approximation to a 1D system.

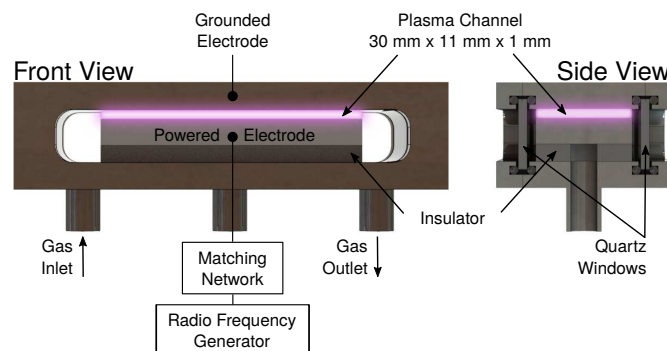


Figure 4.9: Large APPJ Diagram. The plasma volume is 11 times greater than the μ -APPJ.

Typically the most complex of fluid models for the APPJ are only 1D, approximating the system as infinite parallel plane electrodes, therefore side walls are not considered and the spatial resolution is across the discharge gap only, allowing for study of sheath and bulk dynamics in time. Estimates of plasma power from these models will act as a check on whether the measured power values appear reasonable using this phase-corrected subtraction method. Modelling of this plasma has been limited to oxygen admixtures of 0.5% [43, 66] and helium only discharges [43], and thus these admixtures have been used for this proof of concept.

Figure 4.10a shows the power measured when the plasma is operational using only helium. The plasma off measurement is taken when air is in the device, and a plasma cannot be ignited. The difference in dissipated power at the same current is therefore due to the plasma. There is a clear deviation in power when the plasma is on compared to when the plasma is off.

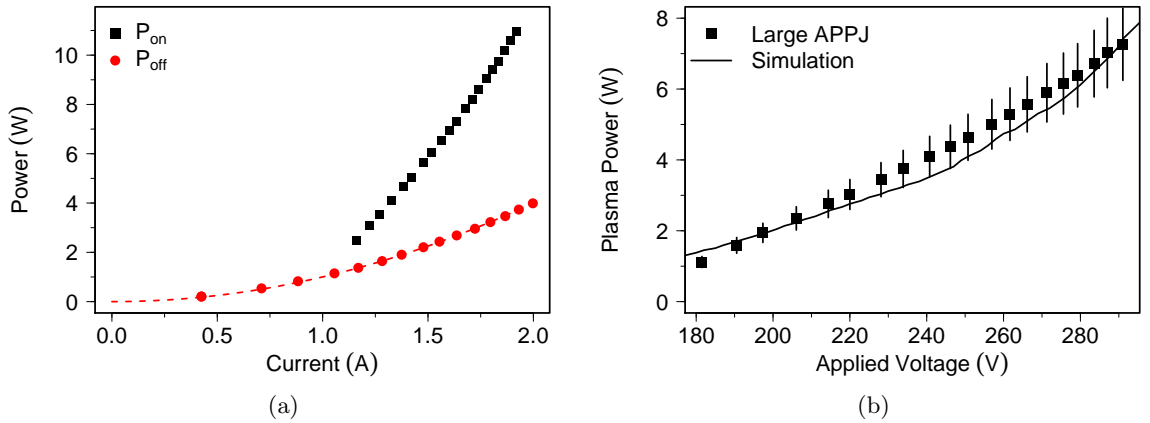


Figure 4.10: (a) Measured power for plasma on, and plasma off conditions for the Large APPJ with He only. Power factor does not change for the plasma off case, and can be estimated using $P = I^2R$. (b) Plasma power for helium only discharge using the Large APPJ, compared against benchmarked 1D simulations [43] show good agreement.

However, it should be noted that at plasma ignition, the power lost into the support circuitry and strays is 50% of the measured power when the plasma is operational. At the higher end, the power into support circuitry and strays is still over a third of the total dissipated power. It is evident that quoting the power when the plasma is ignited and assuming there are no other losses is not a suitable metric for actual plasma power, in the same way that quoting the generator power is not a suitable metric for actual APPJ power where there are losses into both the matching network and parasitics of the plasma device.

The calculated plasma power as shown in Figure 4.10b shows excellent agreement with a benchmarked 1D fluid simulation based on the APPJ [43]. This simulation consists of helium with a small amount of nitrogen (0.1%) to mimic air impurities. The sealed nature

of the larger jet, as it was designed to operate in the vacuum environment of a VUV beam line [58], limits the amount of air impurities that can enter the plasma, unlike the μ -APPJ.

The calculated plasma power was then compared to measurements using a commercial probe, the SOLAYL Vigilant VI probe, which has been optimised for APPJs. In the SOLAYL Vigilant VI probe the voltage and current probes are co-located on the transmission line, and this experiment will act as a test for the validity of using two separate probes with their inherent transmission line error, but calibrating to a capacitor to minimise this. Though the manufacturer states an instrumental phase shift, it has a large error of $\pm 2^\circ$. This value is acceptable for pre-matching configurations, but as discussed this uncertainty is unacceptable in post-matching configurations. The same calibration procedure was applied to the SOLAYL probe using a known capacitor, and the instrumental phase was found to be within the manufacturers error. Measuring plasma power post matching means that even for commercial probes that connect to an oscilloscope, this calibration is a requirement due to inherent instrumental phase differences.

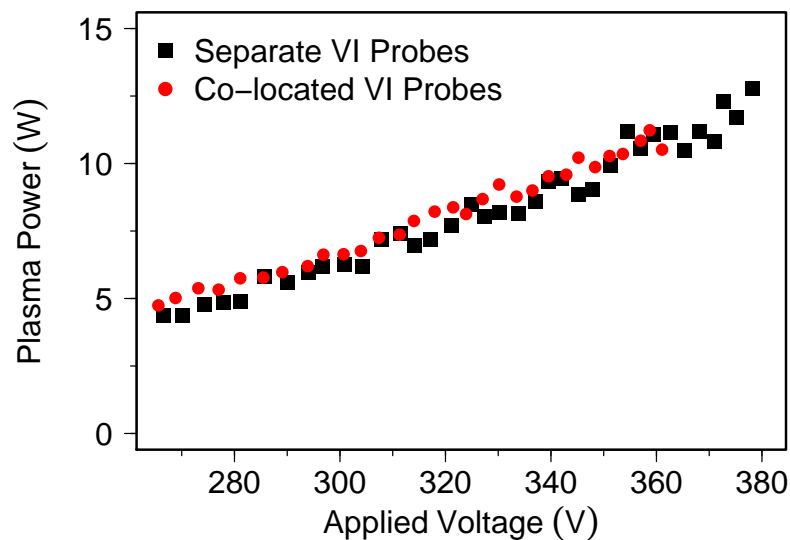


Figure 4.11: The measured plasma power is the same for both the commercial integrated probe, and when using individual current and voltage probes.

Figure 4.11 shows the measured plasma power being within error for the same driving voltage using individual probes and the combined commercial probe. The order of the probes and the calibration procedure yields the same result as the commercial probe, which has undergone extensive testing [140], with the current and voltage pick ups almost co-located. Using individual probes with the current probe upstream of the voltage probe is experimentally valid, and for this investigation also experimentally more convenient as the frequency and phase response is more uniform for individual probes when compared to frequency specific commercial probes, such as the Vigilant VI probe or the Impedans OCTIV VI probe.

Finally, the smaller μ -APPJ was compared to the larger jet. Figure 4.12 shows that for the same feed gas admixture (in this example 0.5% O₂) and velocity through the channel (16.6 ms⁻¹), the plasma power density per unit electrode surface area for a given driving voltage is the same for both devices, which share the same inter-electrode distance of 1 mm. Their operational voltage ranges are not equal for a number of reasons. Firstly, the larger jet suffers from less wall losses (as a fraction of its volume) in comparison to the μ -APPJ. Secondly, the smaller impurity content is likely to change the breakdown voltage. Thirdly, the sharp corners of the electrode design in the large APPJ lead to localised sparks and arcing at the corners where the electric field is enhanced, as a consequence the upper voltage is limited as to prevent electrode damage.

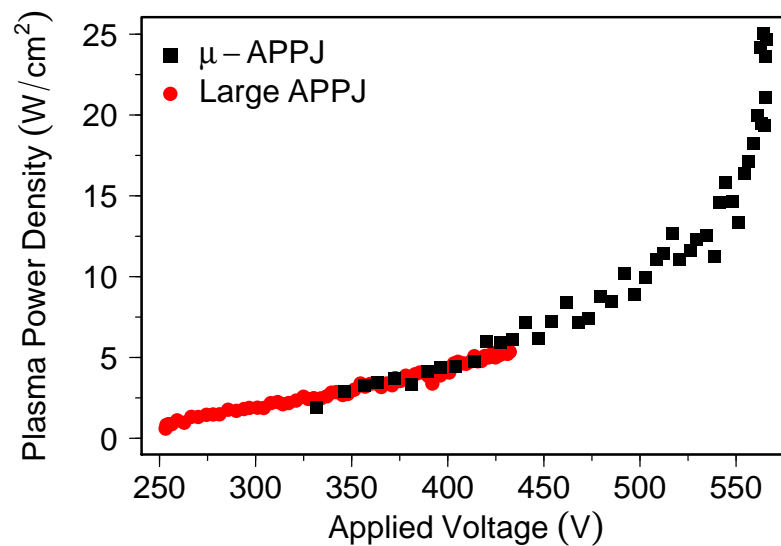


Figure 4.12: For the same gas mixture, and same driving voltage, both the large and micro APPJs have the same power density. For example 0.5% O₂ admixture.

It can be seen that the μ -APPJ suffers from more noise when measuring plasma power. To begin with, the phase angle is closer to -90° (between -89.5° and -89.1° for 0.5% O₂) when the plasma is in operation. The large APPJ has a phase angle ranging from -88.6° to -87.3° when using 0.5% O₂ admixture, and so noise does not play as great a role in the power factor. Furthermore, the power measured in the μ -APPJ with the plasma running is sometimes not much greater than the plasma off case. This may range from a few percent at ignition to 100% at the highest plasma powers. Despite this, the plasma power measured shows clear trends and a good quantitative measure of the plasma power for a given voltage. The shape of the power-voltage characteristic is in very good agreement with measurements of power made in atmospheric-pressure plasmas in the past [11, 136, 143–147], as well as simulation [148].

4.4.7 Advantages of measuring phase angle directly

Phase is resolved as a consequence of the chosen method of measuring plasma power. This phase can be used to help probe the state of the plasma. Reported phase angles can be cryptic, as they may be for the lumped plasma circuit, or what is measured as a whole. They can be useful in illustrating how the circuit as a whole is behaving and what type of impact operating the plasma has, but the absolute number is not always the best gauge. Instead, the degree of change and in which direction is a far more useful indicator of the plasma system.

Figure 4.13 shows how phase angle changes as voltage is increased for the entire measured circuit (plasma and strays). As the phase angle becomes closer to zero, it is clear that the discharge is becoming more “resistive”, as the plasma power is increasing with voltage. However, if this was not known the change in phase angle would be indistinguishable from a scenario where the circuit is merely becoming more inductive. Measuring the voltage, current, and phase allows for resolution of both the resistive and reactive components.

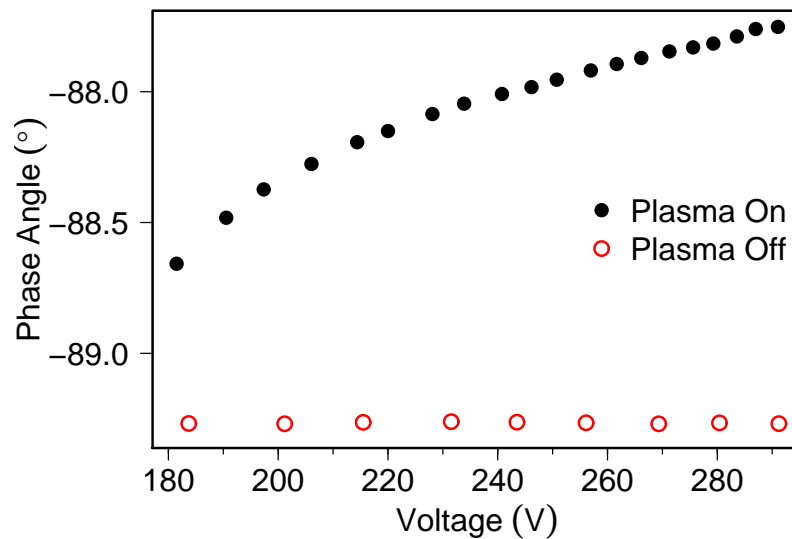


Figure 4.13: Phase angle of the system when the plasma is ignited, and when operated with air for the Large APPJ in a helium feed gas.

Figure 4.14a shows the change in resistance when the plasma is operating compared to the resistance measured when the plasma is not operational. The resistance increases, which is to be expected when considering that more power is being dissipated in the circuit due to the plasma. However, the reactance is also changing as seen in Figure 4.14b. By taking the expected value of plasma inductance [16] using $L_p = R_p/\nu_m$ where R_p is the plasma resistance (around $2\ \Omega$) and ν_m is the effective electron-neutral collision frequency ($10^{12}\ \text{s}^{-1}$), the inductive reactance using Equation 4.4 is on the order of $150\ \mu\Omega$. When instead considering the capacitive reactance using Equations 4.8 and 4.5, it is on the order

of $4\text{ k}\Omega$. For this system, a crude plasma model of a resistor and capacitor in series can be assumed [143, 149], with the reactance can be described as a change in net capacitance.

At low input voltages, the difference between the plasma on and off cases is the addition of more capacitance due to the sheath region. As the reactance is getting closer to zero, the capacitive impedance Z_C must be diminishing, and therefore the capacitance is increasing. As voltage is increased, the reactance clearly deviates from the plasma off case, indicating that the capacitance is further increasing. From Equation 4.8 in a normal capacitor the decrease in Z_C must come from a shrinking electrode gap d . In our model, this equates to a contracting maximum sheath width S_m with increased voltage. It is known that as electron density increases, S_m will decrease [1, 16, 145, 150], which coincides with our increase in dissipated power.

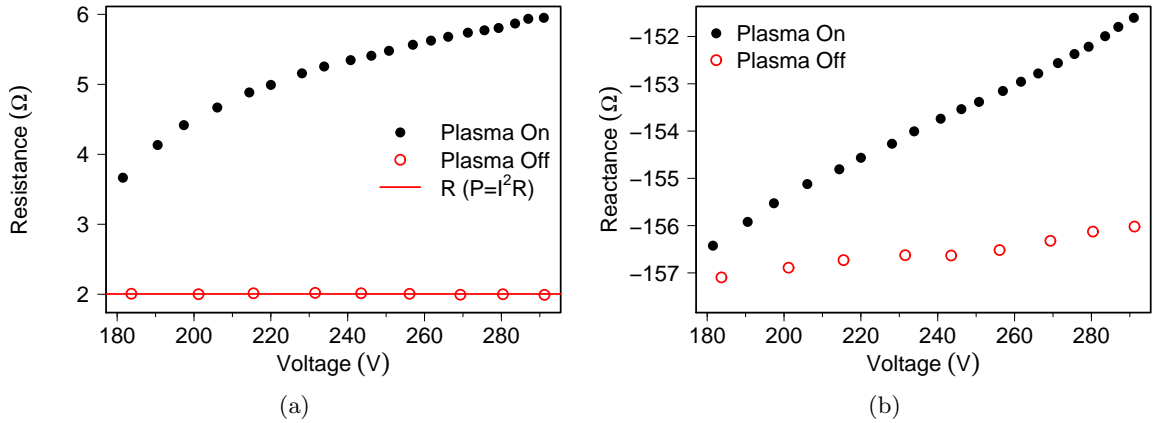


Figure 4.14: (a) Change in resistance between the on and off cases in a helium only plasma for the large APPJ. (b) Sheath capacitance changes the reactance of the system compared to when the plasma is not operating.

The change in resistance in Figure 4.14a may be understood when consulting the resistivity. In the first approximation the resistivity may be considered invariant, however the resistance scales with the bulk plasma volume. As the sheath region diminishes, the greater the bulk volume becomes, and with a constant resistivity the resistance increases, therefore greater bulk power dissipation. This increase in resistance is observed with a linear relationship with voltage after the initial phase of the bulk filling the entire plasma channel at low voltages. The behaviour of increasing plasma resistance has been observed in the μ -APPJ and other APPJs in the past [11, 151]. In low-pressure this behaviour has been attributed to ion heating in the sheath [138], which is proportional to electron density as electrons are responsible for the production of ions through electron impact ionisation [16]. As the electric field in the sheath increases, there is more electron production from electron-cascade events, and this will increase the ion density in the sheath as a result. This does occur at elevated pressures [16], and can be a significant source of heating at high power [43, 65]. The resis-

tance then can be understood as two forms of collisional heating, firstly into bulk electrons, and secondly into sheath ions at high power, both of which scale with bulk electron density.

4.5 Results

As the method used has been shown to give estimates of plasma power for the Large APPJ which are consistent with simulations and power densities in the μ APPJ, estimates of plasma power can be made for the μ -APPJ under various operating parameters of interest.

4.5.1 Variations in N_2 and O_2 admixture

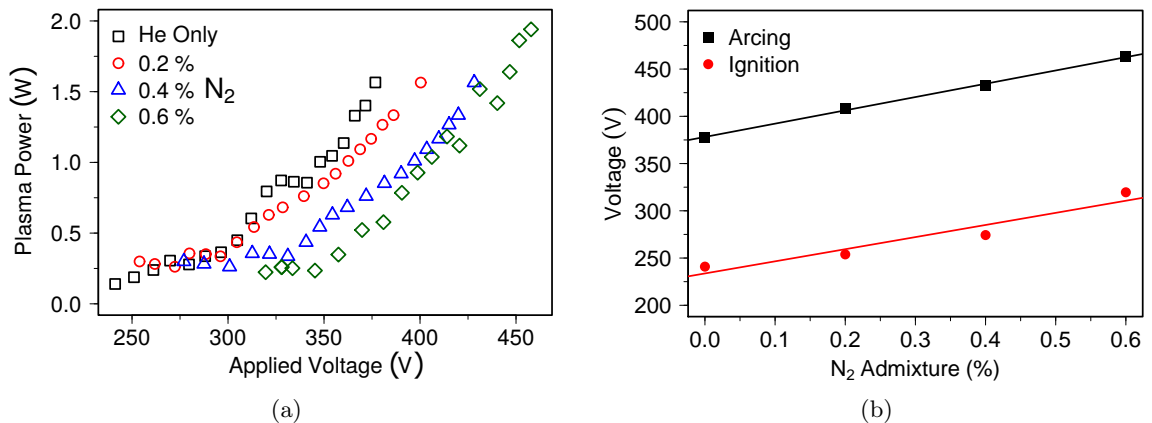


Figure 4.15: (a) Plasma power as a function of driving voltage for nitrogen admixtures up to 0.6%. Plasma power begins at around the same value of ~ 0.25 W for all admixtures, with an early flat behaviour of power with applied voltage. At higher operating voltage, there appears a decrease in power for the same driving voltage with higher admixture. (b) shows the change in ignition and arcing voltage for each admixture. Ignition and arcing voltage increase with molecular admixture.

Figure 4.15a shows the plasma power with applied voltage for differing admixtures of molecular nitrogen in 1 slm helium. At first all nitrogen admixtures appear to share roughly the same power for the first 25 V to 50 V at approximately 0.25 W. Above these voltages, the plasma power increases at a similar rate for all admixtures. The plasma power with increasing N_2 admixtures shows a decrease for the same driving voltage after the initial flat response. For example, at 375 V the plasma power for helium only is around 1.4 W, whereas for 0.6% N_2 the value is closer to 0.55 W. This drop in plasma power for equal driving voltage has been seen in previous studies [11]. A linear relationship across the admixtures can be found giving a -0.3 W difference at this voltage for every 0.2% increase in nitrogen admixture. The maximum input power before arcing appears fairly invariant with admixture, with a power of 1.6 W (except with 0.6% N_2 admixture at 1.9 W). Values estimated agree

with those found by Marinov & Braithwaite [11], who measured around 1.5 W at 0.2% N₂ admixture, as well as the general shape.

Figure 4.15b demonstrates the change in ignition and voltages before arcing across the different N₂ admixtures studied. Both ignition and maximum voltage increase at roughly similar rates of 29 V for every 0.2% nitrogen admixture increase. For repeatable power densities for various nitrogen admixtures, the ignition or arcing point is a fairly reliable metric, whereas the same voltage with various admixtures may lead to considerably different values for plasma power.

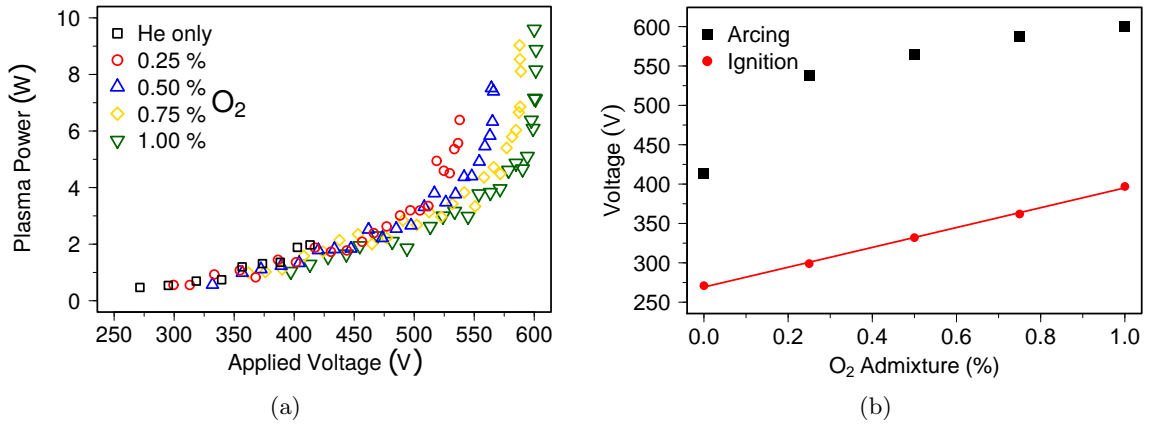


Figure 4.16: (a) Plasma power as a function of voltage for O₂ admixtures up to 1%. Plasma power appears largely invariant with O₂ admixture, with only a slight decrease in plasma power observed with increased molecular admixture. (b) shows change in ignition and arcing voltage for each admixture. Ignition and arcing voltage increase with molecular admixture.

Plasma power against applied voltage for varying admixtures of molecular oxygen is shown in Figure 4.16a. Below 475 V the decrease in plasma power for a given voltage is marginal when oxygen admixture is increased. What is visible is the increased voltage required to ignite the plasma when more oxygen is added to the gas mixture as shown in Figure 4.16b, mimicking the behaviour for molecular nitrogen admixtures. For O₂ admixtures however there does not appear to be the same parallel linear trend in the maximum voltage as with N₂, but still with the lowest maximum voltage found with helium only.

The increase in ignition voltage seen with higher admixtures has also been seen previously [11, 147, 152]. The increase in breakdown voltage, V_b , with molecular admixture can be understood when consulting Paschen's Law for simpler DC cases (for which RF discharges share similar characteristics in highly collisional regimes such as atmospheric-pressure),

$$V_b = \frac{bpd}{\ln(apd) + \ln(\ln(1 + 1/\gamma_{se}))} \quad (4.16)$$

The constants a and b are dependant on the gas, and are determined experimentally. The term pd is the pressure length product, and γ_{se} is the coefficient for secondary electron

emission and is dependant on the material of the electrodes. At atmospheric-pressure, for a 1 mm plate separation, the breakdown voltage required for O₂ is roughly 7 times greater than helium, likewise for N₂ the value is 8.5 times greater [26]. At these elevated pressures, with typical values for the a coefficient and secondary emission coefficient of the stainless steel electrodes, the breakdown voltage ratios begin to be roughly proportional to the constant b .

As more molecular species are introduced into the helium, the required breakdown voltage increases. For oxygen, for every 0.25% admixture, an increase of approximately 30 V is seen, consistent with other measurements of the μ -APPJ [11]. For the equivalent 0.25 % admixture of nitrogen, the change is 36.5 V, which shares the same ratio of 7:8.5 in the b coefficients. This factor of 30 V per 0.25 % O₂ is the same for both the large and micro plasma jets, indicating that the higher voltages are indeed a Paschen effect.

The slight decrease in power for the same voltage with higher molecular admixtures is known to happen in experiment [11] as well as modelling [66], however for oxygen admixtures in the early linear regime below 475 V it is not as dramatic as in the nitrogen case, with the voltage to power relationship essentially the same for all admixtures. This allows for a degree of reproducibility for differing admixtures, by selecting a voltage that will allow operation over all desired gas admixtures, rather than taking the ignition point, where the dissipated powers are not equal. The region in which the power rises dramatically (this will be discussed in 4.5.2), occurs later with respect to voltage with higher admixtures [153], meaning that total power is higher before this transition occurs (see Figure 4.16). This is twinned with greater maximum plasma power overall before the plasma begins to “arc”; these behaviours have been reported for coaxial APPJs [143].

4.5.2 Diagnosis of plasma operating modes

As mentioned in 4.5.1 there are two apparent regimes in which the plasma appears to operate with oxygen admixtures. After ignition, a slow linear increase in power with driving voltage is observed, followed by a dramatic increase in plasma power at a critical point. These are known as the α -mode and γ -mode [26].

At high-pressure an α -mode discharge is driven by electron excitation by the advancing and retreating sheath edge [1, 16, 131], and the electron density increases with voltage [145]. The plasma looks diffuse, with dark regions near the electrodes (where the sheath is present). Heating is dominantly in the plasma bulk due to the “hard wall” of the expanding and retreating sheath edge. At a critical current density, the dominant spatio temporal electron heating mechanism changes the from bulk to sheath.

γ -mode has extra contributions to electron heating from inside the sheath. The symbol γ refers to secondary electrons which at low-pressure are produced due to ion bombardment of the electrodes and subsequently accelerated in the strong sheath electric fields [26]. At atmospheric-pressure the secondary electrons mainly originate through Penning ionisa-

tion [43, 154] within the plasma sheath where they are accelerated by the strong sheath electric field. The transition to γ -mode can be classified as the point where electron-cascade production due to the high sheath electric fields is equal to or greater than production through bulk penning ionisation [150]. Ions are also accelerated through the high sheath electric fields, and more energy is dissipated as a result. There now exists an extra intra-sheath collisional heating term, which in the circuit description of the plasma is given by another resistor R_g .

Phase Resolved Optical Emission Spectroscopy (PROES) has been performed on μ -APPJs in the past [41, 155–157] and can indicate the spatio-temporal sources of excitation of species in the plasma. As such, PROES is regarded as the best method to identify mode transitions as it allows direct visualisation of the electron dynamics [146, 154, 158, 159].

However, the implementation of PROES requires a costly intensified CCD (iCCD) and often knowledge of collisional quenching rates of excited states, which at atmospheric-pressure can introduce significant uncertainties (see discussion for TALIF in Section 3.2.2.2). As such, the identification of mode transitions from the electrical characteristics is favourable due to the low cost and ease of implementation.

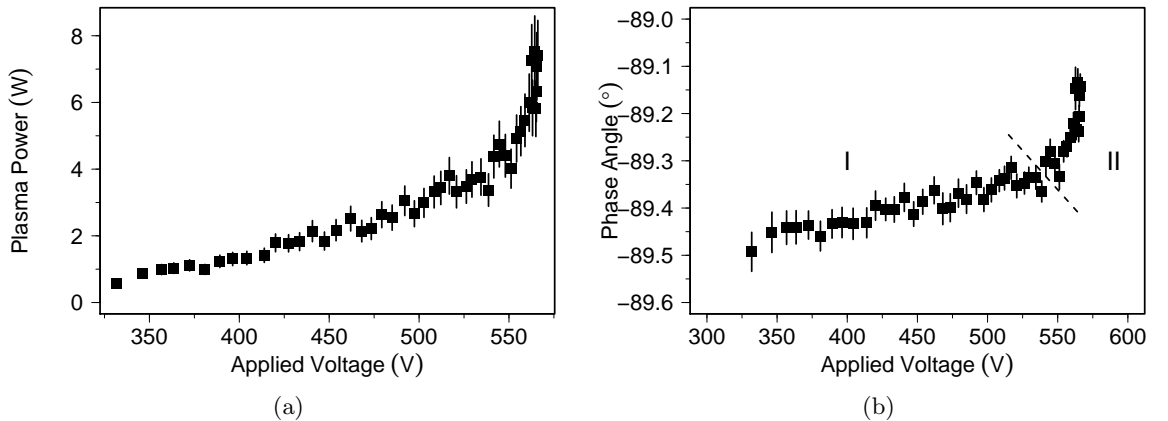


Figure 4.17: (a) Plasma power as a function of driving voltage at 13.56 MHz with 0.5% O_2 admixture. Power increases monotonically, with an accelerated rate at voltages above 550 V. (b) Phase angle of the system when the plasma is operational for the μ -APPJ. Firstly the plasma operates in a traditional α -mode in region I. As voltage increases, the phase angle begins to increase sharply, indicating a mode transition in region II.

Figure 4.17a shows the plasma power varying from around 0.9 W at 350 V, to around 3.8 W at 530 V at a fairly linear rate. The plasma power then dramatically increases up to 7.5 W at 565 V, practically doubling over only 30 V. The plasma power vs voltage response is expected for the μ -APPJ as it operates in the α -mode and into a so-called “hybrid mode”, where electrons are produced in similar quantities through both α and γ mechanisms [43, 145, 148]. For a full transition into a gamma mode, the voltage would be expected to begin reducing with higher plasma power. There are no observable hysteresis

effects, which may result in differing voltage-power characteristics as the generator power is increased or decreased [34, 147].

The phase angle of the plasma and ancillary circuitry is presented in Figure 4.17b, with the error bars coming from a Bayesian error estimation based on the uncertainty in voltage, current, frequency, and noise, with the absolute values being nearly identical with estimations made by FFT. Two distinct regions can be seen in the phase angle which suggests two different regimes of plasma dynamics. The linear region between 330 and 530 V is visible, with a faster rate of change occurring afterwards in the same voltage range seen in the plasma power. The change in phase angle reflects the increase in power being dissipated, and possibly phase angle alone can indicate mode changes, but once again the resistance and reactance can be separated out to glean more information.

Figure 4.18a shows a steady linear increase in resistance for the plasma on case, with a sharp rise in conjunction with the sharp rise in dissipated power. The reactance in Figure 4.18b demonstrates the same behaviour of the sheath diminishing as in Figure 4.14b, but at the higher voltages the decrease becomes more exaggerated. The exaggerated decrease conforms to what is known about the electron excitation during $\alpha - \gamma$ transition. The sheath width decreases rapidly with γ -mode [145, 160], as the sheath begins to have considerable electron populations, it is no longer a charge free region like in a true capacitor and behaves more like the quasineutral bulk plasma. This is seen as a near vertical decrease in the net reactance. This increase in bulk plasma volume also explains the rise in plasma resistance, as well as being enhanced by increased sheath heating into the ions [16, 43, 65].

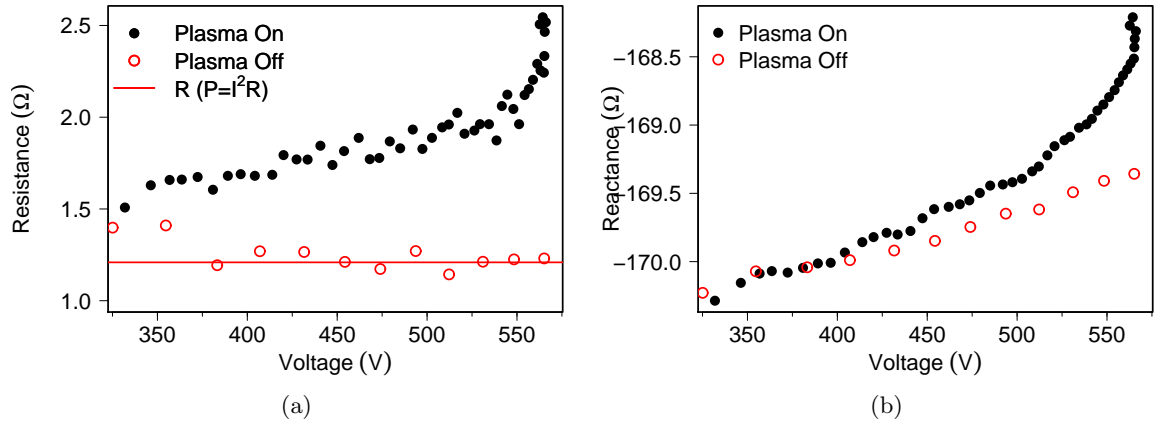


Figure 4.18: Change in resistance (a) when the μ -APPJ is on compared to when the plasma is off indicates greater power dissipation. The sheath capacitance changes the reactance (b) of the system when compared to when the plasma is not operating.

Though the transition to γ -mode is not necessarily abrupt (and gradual transitions have been seen at atmospheric-pressure [145]), it can be seen especially in the resistance, that the gradient is an indicator for mode change. For this to be a true transition into γ -mode, voltage would be decreasing with further input of power into the system, however coupling more power into the μ -APPJ is not possible. What limits the operation of the μ -APPJ in a fully fledged γ -mode at 13.56 MHz is the formation of an “arcing-mode” [12,143,156,161,162] also known as a “constricted-mode” [163] where localised gas heating develops into an arc plasma [164]. This arc type regime is undesirable, as it causes damage to the electrodes through high currents and considerable heating, in some cases enough to melt the surrounding plastic chassis of the μ -APPJ.

This arcing can be mitigated with the use of dielectric materials over the electrodes [163], so-called Dielectric Barrier Discharges (DBDs) can allow operation further into the gamma regime, which may offer greater reactive species densities [165]. This mode transition may in fact be a hybrid-mode that consists of significant contributions of both bulk and sheath heating, hence the turn over into the γ -mode is not seen, but enhanced power deposition takes place.

4.6 Comparison to PROES

Phase Resolved Optical Emission Spectroscopy (PROES) is a technique whereby optical plasma emission is captured by a fast gated detector such as an iCCD to offer spatio-temporal resolution of emission throughout the RF cycle [166, 167].

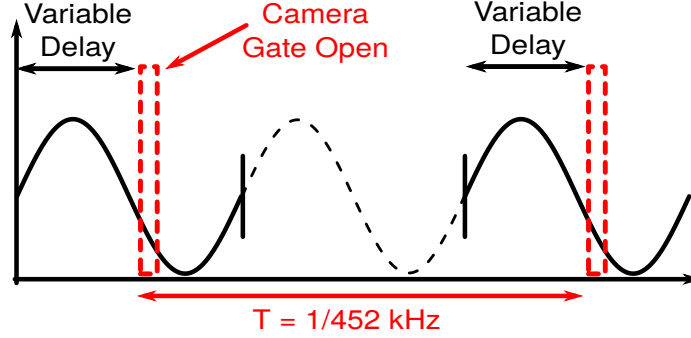


Figure 4.19: Diagram demonstrating the concept of PROES. Images are taken every 30th RF period at 13.56 MHz, the equivalent to 452 kHz. The RF waveform represents from the trigger out of the RF generator. After a sufficient number of images at a given variable delay are acquired, the camera gate delay is increased, and over the course of the measurement, spatially resolved measurements of emission are recorded for the whole RF cycle for a fixed camera gate width.

Figure 4.19 demonstrates how the detection gate is sequentially moved to acquire images throughout the RF cycle. The Andor iCCD used is capable of being triggered at a rate up to 500 kHz, which is slower than the trigger signal from the RF generator at 13.56 MHz. Therefore the RF generator trigger out is conveniently prescaled by the digital delay generator already *in situ* for TALIF (Stanford Research Systems DG645) resulting in a trigger signal being sent to the camera 1 in 30 RF cycles (equivalent to 425 kHz). The camera gate is then delayed by a set value by the digital delay generator via PC serial commands, allowing for images to be taken along the full RF cycle. In this work, an incremental gate delay of 1 ns was used.

Emission of a single line using an interference filter in front of the iCCD can be converted to excitation using the same theory that was established for TALIF in Section 3.2.1. Assuming that the ground state population (n_1) remains constant, and knowing that the signal detected ($S(t)$) is directly proportional to the excited state density (n_2), Equation 3.3 can be rearranged to give the excitation rate, $Ex(t)$, as function of Signal, $S(t)$, and effective decay rate A :

$$Ex(t) = \frac{1}{n_1} \left(\frac{d}{dt} S(t) + A \cdot S(t) \right) \quad (4.17)$$

Excitation rate is given as $Ex(t)$ rather than $R(t)$ (as is the case for TALIF in Equation 3.3) to avoid confusion as it is assumed for PROES that excitation originates primarily

through electron impact excitation, where TALIF uses laser excitation. Excitation features offer insight into where energy is deposited spatio temporally in the system, and has been used in the past to investigate power deposition previously in atmospheric pressure plasma jets [60], as well as low pressure discharges [166, 167]. Treatments of PROES can be found in those articles, or more thoroughly in [168] and [169].

Previous measurements using TALIF offer an excellent opportunity to confirm the interpreted measurements of phase and power to phase resolved optical emission spectroscopy. Not only is an iCCD that is spatially calibrated available, but the TALIF measurements themselves offer the decay rates of the excited states directly. This removes the need to estimate the decay rate, and accurate maps of electron impact excitation can be made by taking the first derivative of the emission and correcting for the effective lifetime [130]. The calculated excitation is then averaged over the electrode area to give a 1D map across the discharge gap between the electrodes as a function of time.

4.6.1 Sheath dynamics and operating modes

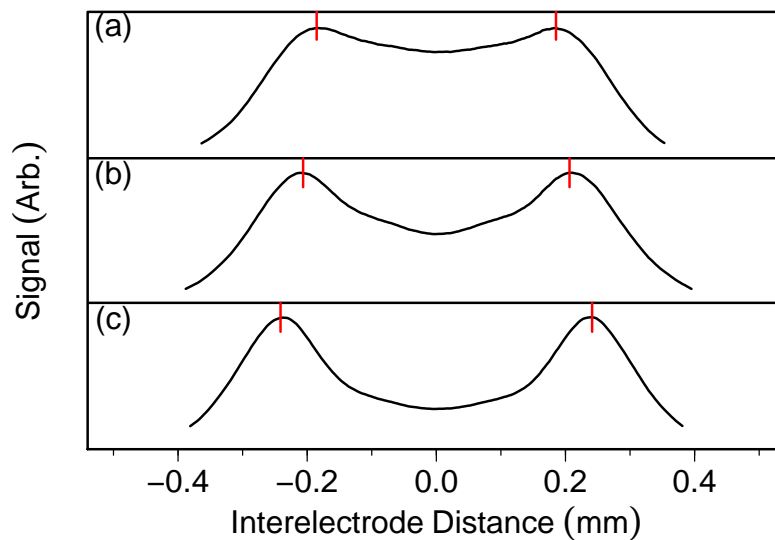


Figure 4.20: Atomic oxygen emission at 844 nm for a He plasma with 0.5% O₂ admixture is time-averaged over one RF cycle, and integrated along the plasma channel, resulting in time integrated emission between the electrodes. As power density increases, the sheath region constricts resulting in thinner sheath features. Peak emission is indicated with a red vertical marker to aid in visualising sheath extent, where ± 0.5 mm indicates the electrodes. No appreciable emission is visible inside the sheath. The highest power (c) has smaller sheath structures than the medium (b) and low power (a) cases where they span further into plasma channel.

Before investigating phase resolved emission, the time-averaged emission can also act as an indicator for plasma dynamics. When operating the μ -APPJ with 0.5% O₂ admixture, time integrated images of atomic oxygen emission at 844 nm over an RF cycle give an im-

pression of the extent of the sheath as operating power increases. The emission at 844 nm results from the electron impact excitation of atomic oxygen into the $O(3p^3P)$ state. This can occur via direct electron impact excitation of O, which has an electron energy threshold of 10.98 eV or through dissociative excitation of O_2 which has an electron energy threshold of 16.3 eV. Therefore emission allows visualisation of the regions of time and/or space where electrons have energies above these thresholds due to sheath expansion and collapse mechanisms. In Figure 4.20 as voltage and therefore power is increased from (a) to (c) the sheath region contracts, i.e. the region of high emission moves closer to the electrodes as predicted by the measurement of reactance in Figure 4.18b.

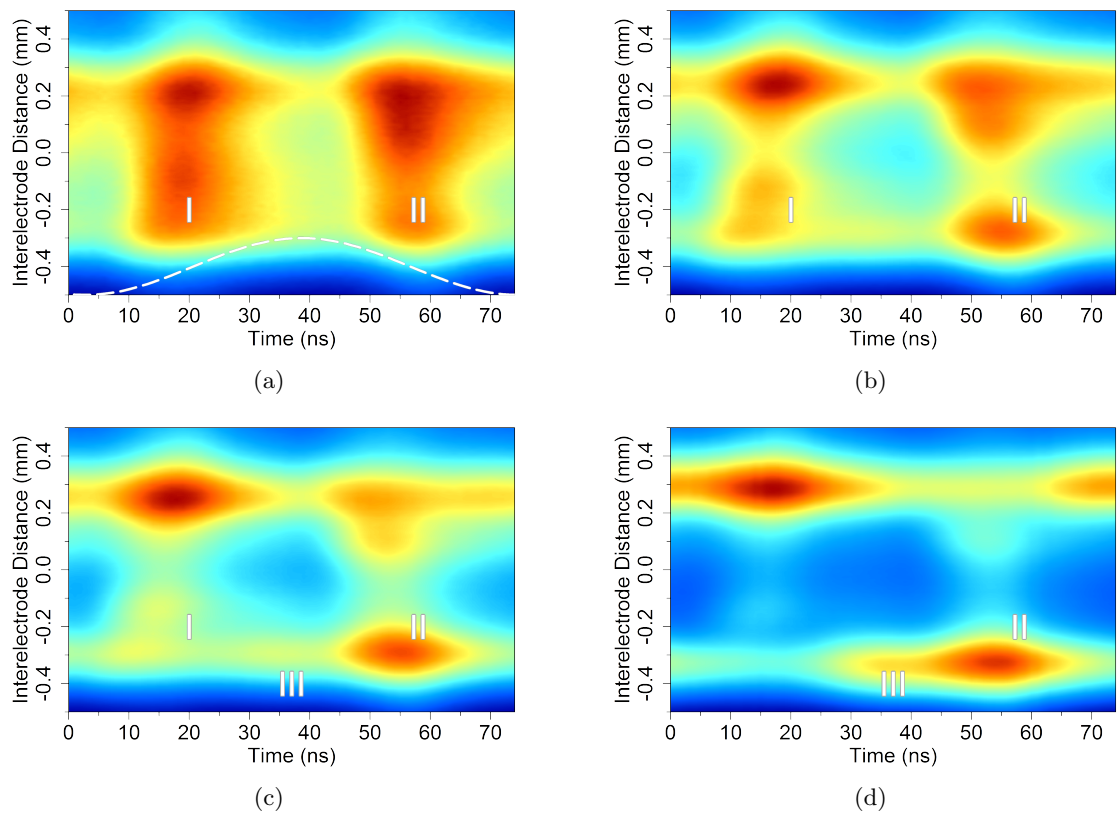


Figure 4.21: The excitation is shown as a function of both space between electrode (vertical axis), and time throughout one 13.56 MHz RF cycle (horizontal axis). Each is normalised to the maximum value, with blue being the lowest value and red the highest value of excitation. Power density increases from (a)-(d) (~ 1 W, ~ 2 W, ~ 3 W, ~ 5 W), with electron impact excitation occurring from different spatio-temporal locations. Excitation in region “I” is a consequence of sheath expansion, whereas excitation in region “II” is due to sheath collapse heating. Region “III” indicates intra-sheath energy deposition. (a) shows a dashed line to represent how sheath extent changes over an RF cycle, however this is merely to guide the eye, and has not been explicitly calculated.

Resolving emission of the 844 nm line as the plasma evolves over the RF cycle can reveal more information about the heating mechanisms in the plasma. Figure 4.21 indicates where excitation is happening in both space and time in the plasma. Each image is normalised to the maximum excitation, as the ground state density (as per Equation 4.17) is required to obtain absolute values.

Figure 4.21a shows spatio temporal excitation for a low power ~ 1 W discharge. The dashed line represents the motion of the sheath over the RF period, however it is not an explicit calculation and should not be taken as an actual value. There are two regions visible where excitation occurs close to the electrode, which are offset on the opposite electrode. Excitation in the first region I originates from sheath expansion, where the sheath can be thought of as a “hard wall”, accelerating electrons away into the bulk and imparting energy. When the sheath collapses, there is a field reversal, and the electrons are dragged back, also imparting energy [60], highlighted in region II.

As power increases further (~ 3 W), sheath collapse becomes the dominant process in coupling energy into electrons (Figure 4.21c). Finally, at power densities just before reaching the constricted or arcing mode (Figure 4.21d ~ 5 W), a third feature is visible (region III). This feature comes from Penning ionisation inside the sheath, and those electrons produced are accelerated strongly in the sheath fields and collide with O and/or O₂ to produce the observed emission. This indicates the hybrid mode between plasma sheath heating α -mode, and the intra-sheath heating γ -mode exists, as predicted by the power measurements.

4.7 Summary

Estimates of plasma power can be performed in small atmospheric-pressure RF capacitively coupled discharges, without need to make assumptions on the phase angle, while maintaining a flexible experimental setup, which has not been achieved previously with the μ -APPJ.

Plasma power in the μ -APPJ in the α -mode is fairly linear with applied voltage, in helium a range of 0.25 W to 2 W between 240-410 V. For 0.5% admixture of O₂, range of 0.9 W to 3.8 W for a voltage range of 350-530 V. When in the hybrid mode, this plasma power can be considerably higher. For nitrogen admixtures, powers typically range from 0.25 W to 1.6 W which is equivalent to oxygen admixtures in the same voltage range.

Measuring plasma power has allowed not only a measurement for benchmarking and comparisons, but a unique perspective on best practices when operating and comparing atmospheric-pressure plasma jets. For example in oxygen admixtures, when comparing plasma properties at varying admixtures the voltage is the best metric for ensuring a fairly consistent power density when unable to measure plasma power directly, whereas using the ignition/arcing point will not yield the same power density between measurements. When measuring plasma power in a μ -APPJ device such as the EU COST reference jet, it is also important to measure the power when the plasma is off to try reduce the overall systematic error when estimating the true plasma power. The typical assumption that there is no power dissipated when the plasma is off can lead to very large discrepancies, especially at low operating powers when the plasma dissipation is only a few percent more than the parasitics.

Finally, mode transitions are discernible when assessing the phase in a post-match configuration between the voltage and current, and offers a cost effective alternative to other techniques such as PROES. It is also apparent that the transformation into the gamma mode is not abrupt, and the two modes can coexist in a hybrid mode, as confirmed by PROES measurements. Measurements of power in the μ -APPJ using other methodologies have not definitively identified this behaviour, and it now may allow for further tailoring of plasma operating parameters for specific applications.

Chapter 5

Characteristics of the μ -APPJ under driving frequency variation

Application and design usually dictate the required radio band in which a device operates. This may be the Very Low Frequency (VLF) band for kHz plasmas, High Frequency (HF) for MHz devices such as the μ -APPJ, or Ultra High Frequency (UHF) for microwave driven devices. The particular driving frequency in these ranges is usually chosen because of external constraints, such as the International Telecommunications Union (ITU) Industrial, Scientific, and Medical (ISM) bands, and often more importantly the availability of components. It makes sense for a manufacturer or researcher to use existing components and equipment, such as magnetrons for microwave ovens operating at 2.45 GHz, which are mass produced, cheap, and readily available (as well as acceptable for industrial, scientific, or medical use).

There is growing interest in using different frequencies to tailor plasma parameters. An excellent example is the field of low-pressure plasma etching, where plasma frequency can alter the ion energy or the flux to a surface [170]. This has led to investigations into dual frequencies [130, 167, 171], as well as tailored waveforms of multiple harmonics [10, 172, 173], to allow control over both the ion energy and flux simultaneously.

There has been comparatively little in the way of modelling and operating the μ -APPJ at harmonics of 13.56 MHz [159], perhaps because this frequency offers reactive species at low gas temperatures [54], which are of importance for temperature sensitive applications such as bio-medicine. With RF equipment at this frequency being prevalent and affordable, there has been little call for change. However, with frequency mixing at atmospheric-pressure gaining more exposure, with the possibility of further control of plasma produced species [174], there is requirement to understand how APPJs operate and what are their characteristics at different frequencies.

5.1 Power Dissipation

In order to better understand the role that varying the operating frequency has in the plasma itself, the power-voltage characteristics have been measured for three different frequencies: 13.56 MHz, 27.12 MHz, and 40.68 MHz. These are shown in Figure 5.1a and 5.1b. The μ -APPJ is operated from ignition, but for 27.12 MHz and 40.68 MHz, an arcing mode was not observed, and so the voltage was stopped at an arbitrary point as to avoid damage to the jet from extended use at high power which is associated with gas heating [54, 175] and power dissipation into the ancillary circuitry. The power can be compared for the different driving frequencies for the same feed gas mixture. Two scenarios were assessed using nitrogen or oxygen in 1 slm helium. An admixture of 0.3% N_2 was used (Figure 5.1a), corresponding to maximum production of atomic nitrogen (see Chapter 3), and 0.5% O_2 (Figure 5.1b) used which corresponds to maximum atomic oxygen production [2].

Visible in Figure 5.1 is the clear difference in discharge power and operating voltages for the fundamental and the first two higher harmonics of $f_0 = 13.56$ MHz.

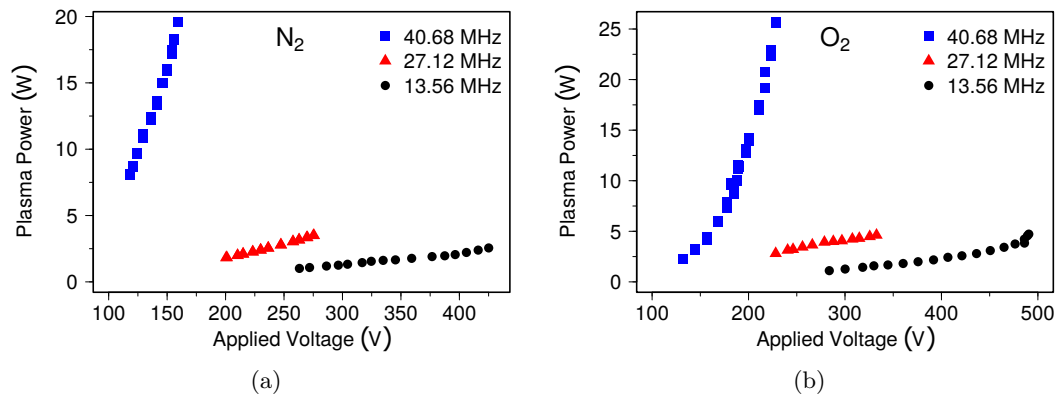


Figure 5.1: Plasma power as a function of voltage for 13.65 MHz, 27.12 MHz, and 40.68 MHz. Higher driving frequencies exhibit greater plasma power for lower driving voltages for both 0.3% N_2 admixture (a), and 0.5% O_2 admixture (b).

For both working gas mixtures, the breakdown voltage for higher radio frequencies is expected to be lower [176, 177], and has been observed experimentally in atmospheric-pressure plasma devices [158, 161, 174, 178, 179]. The approximate factor for the change in breakdown voltage in the μ -APPJ is consistent with those previously measured [174].

For the same driving voltage, it is apparent in Figure 5.1 that 40.68 MHz dissipates most power in the plasma, and 27.12 MHz dissipates more power than 13.56 MHz. Previously at 13.56 MHz the increase in plasma power was attributed to the increase in electron density. From analytical investigations, the electron density is expected to increase at roughly a factor of $(f/f_0)^{>2}$ [180] as frequency increases for the same driving voltage. In fluid simulations of dual frequency 13.56 MHz and 40.68 MHz operation of the μ -APPJ with He and a small

N_2 impurity, the power coupled into electrons for the same driving voltage amplitude was found to be greater for the higher harmonic [171]. However in the same study, the electron density was found to be the same when compared to the same power density. In short, higher frequencies produce greater power density at lower voltages, with the electron density dependant on the power density regardless of frequency.

Over the operating voltage range, at 40.68 MHz the increase in power per volt increase is also greater than the other two frequencies during the linear portion, e.g. in Figure 5.1a the gradient for 13.56 MHz is 0.009 W/V whereas the gradient is 0.268 W/V for 40.68 MHz. For oxygen admixture in Figure 5.1b, the gradients are 0.011 W/V and 0.339 W/V for low and high frequency respectively, over a factor 30 greater for both cases. The time-averaged power input then does not simply scale with frequency (n more cycles in which energy is transferred in the same time), but is a non-linear phenomena.

This increase in electron density is not only indicated by increased power deposition, but also in time integrated images of emission at 844 nm for the μ -APPJ operated with 0.5% oxygen admixture at both 27.12 MHz (Figure 5.2i) and 40.68 MHz (Figure 5.2ii). For both frequencies in Figure 5.2, the same behaviour is observed as for 13.56 MHz, shown in the previous chapter (Figure 4.20), in that the sheath width continues to contract with higher input power densities ((a)-(c)). Moreover, the sheath extent in general is closer to the electrodes as frequency increases when comparing the two harmonics and the fundamental frequency (shown in Figure 4.20); this is consistent with modelling [180] and experiment [181]. From the previously established circuit model, contraction of the sheath is a result of increased electron density which has been predicted and observed from the power measurements.

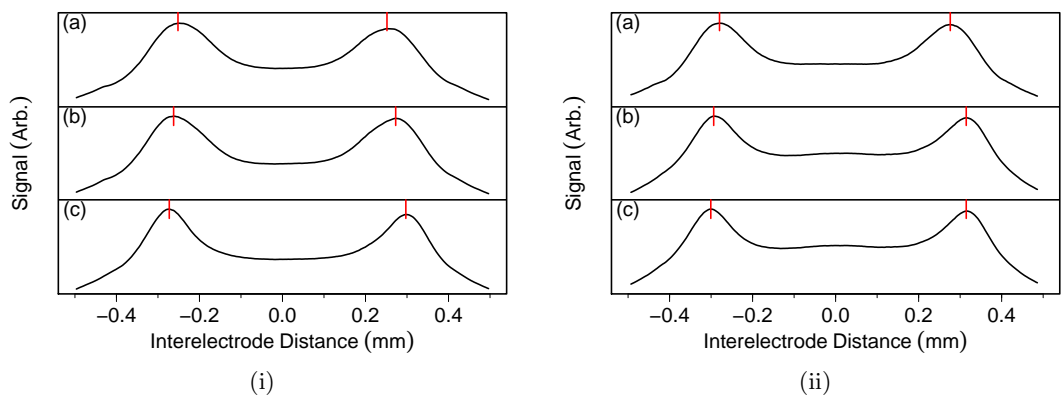


Figure 5.2: Time-averaged emission is an indicator for sheath width, red vertical lines denote emission maxima. At 40.68 MHz (ii) the sheaths are closer to the electrode surface than for 27.12 MHz (i). This is a result of higher electron densities. Both (i) and (ii) exhibit sheath structures closer to the electrodes than 13.56 MHz, with the sheath extent diminishing as power density increases for low (a), medium (b), and high power cases (c).

Though electron density is expected to increase, the electron temperature remains unknown. Some atmospheric-pressure simulations predict it will increase [174], while other simulations predict the mean electron energy to decrease [158], and measurements made with line ratios of argon see little to no change [178]. Fluid simulations using dual frequency in the μ -APPJ suggests that regardless of power density the mean electron temperature (and the electron energy distribution function as a whole) is largely invariant, with only a slight decrease (less than 3%) at 40.68 MHz compared to the fundamental [171]. As the electron energy distribution function (EEDF) has not been assessed, the increase in power dissipation can only be broadly linked to the increase in electron density with the assumption that the EEDF is invariant as modelling suggests [150, 171].

5.2 Reactive Species Production

From measurements of power dissipation, it is clear that the plasma dynamics can be altered by simply changing the driving frequency. This in turn may alter the chemistry produced in the plasma. To optimise the plasma for applications, changing the driving frequency may be a useful way to tailor reactive species densities.

As shown, power dissipation is greater for higher frequencies, which likely indicates higher electron densities. As electron impact is the dominant form of dissociation for both O_2 [182] and N_2 [63] to produce their respective atomic reactive species, it can be predicted that for higher frequencies, for the same driving voltage the reactive species density should be higher. Moreover, the species densities and the power densities should have a qualitative agreement as the two are so closely related via the electron density.

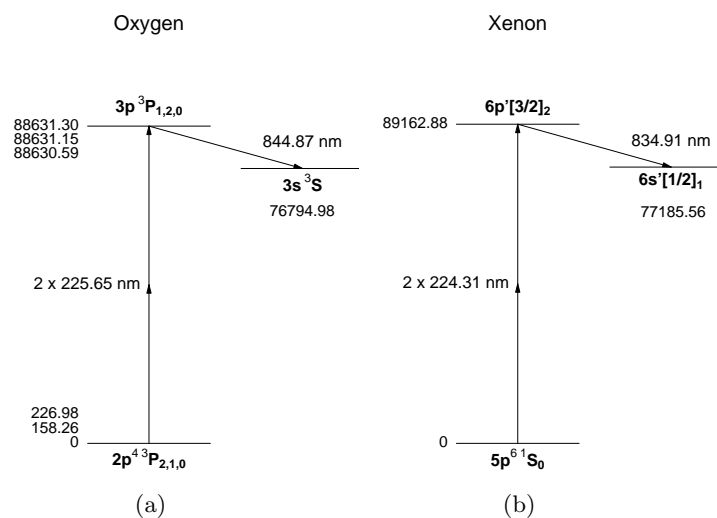


Figure 5.3: (a) TALIF scheme for atomic oxygen O(226) and (b) scheme for xenon Xe(224).

The same admixtures of 0.3% N₂ and 0.5% O₂ were used as for the power-voltage characteristics shown in Figure 5.1, corresponding to maximum atomic species production. Measurement of atomic species densities was performed using TALIF as per Chapter 3. The filters used in front of the iCCD are centred at 845 nm and 835 nm for atomic oxygen and xenon respectively. The excitation schemes used are shown in Figure 5.3, and originate from Niemi *et al.* [59], which has only a $\pm 25\%$ systematic error compared with $\pm 53\%$ for N TALIF due to a more reliable estimate of the two-photon absorption cross section ratio as discussed in Chapter 3. The stochastic error is still in the region of $\pm 14\%$ for all measurements. A complication that arises using the atomic oxygen O(226) scheme is the three possible ground states to excite from. The populations of these states are given by a boltzmann distribution, and therefore the ground state can be estimated by assuming a thermally determined population between the three possible states. This treatment has been covered in detail in [59], and will not be discussed further here. A calibration pressure of 10 Torr of xenon was used for measurement of atomic oxygen. TALIF images were collected to measure both the decay and total fluorescence signals as described in Chapter 3 for all species.

5.2.1 Absolute N and O densities

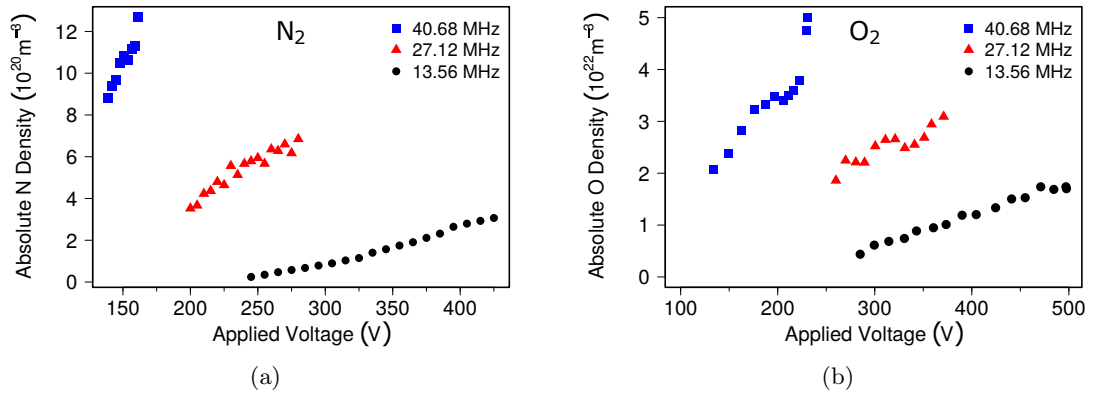


Figure 5.4: TALIF measurements for varying driving frequency for a 0.3% N₂ plasma (a), and a 0.5% O₂ plasma (b). The maximum achievable reactive species density is greater for higher driving frequency. The systematic error for (a) is $\pm 55\%$ and $\pm 25\%$ (b), with both sharing a stochastic error of around $\pm 14\%$.

Figure 5.4 shows absolute atomic nitrogen and oxygen densities in the near effluent of the μ -APPJ. Immediately the qualitative correlation between power and species densities is apparent. The higher the operating frequency the greater the atomic species densities. This correlation also extends into some finer details, such as in Figure 5.4b the atomic oxygen density at ignition for both 27.12 MHz and 40.68 MHz is similar, which mimics the similar plasma power at ignition. This is in contrast to atomic nitrogen production in Figure 5.4a

at ignition, which shows 40.68 MHz having a greater density, reflecting the greater plasma power also seen at ignition under these conditions.

For atomic nitrogen production, the average density measured across the operational range is 7 times greater for 40.68 MHz than the fundamental, for 27.12 MHz it is over 3.5 times greater. Production of atomic oxygen shares a similar story, with an increase of 2.9 and 2.1 times for the third and second harmonic respectively. If electron density is increasing only with higher plasma power regardless of frequency, then it is expected that reactive species densities should also linearly increase with plasma power.

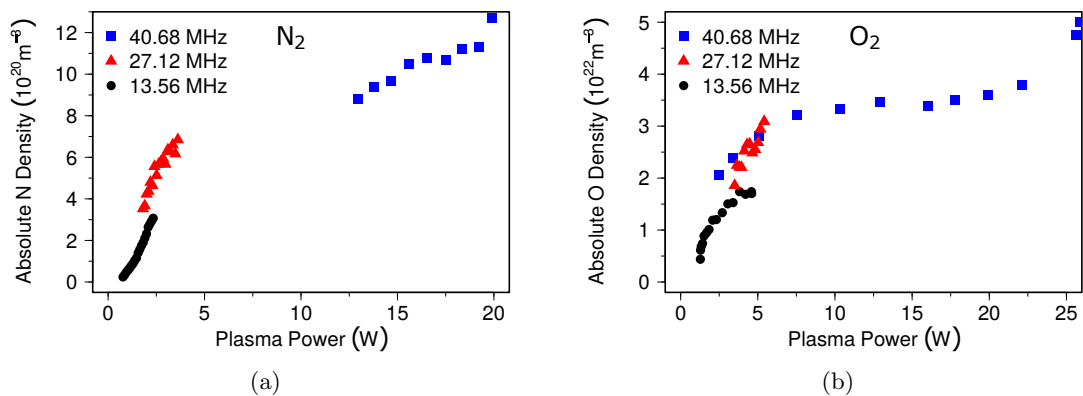


Figure 5.5: Atomic species densities for both N (a) and O (b) against the plasma power. 13.56 MHz and 27.12 MHz both share similar trends, suggesting a linear relationship between plasma power and species production. However in both (a) and (b) the trend is not continued at 40.68 MHz.

Figure 5.5 shows that both atomic nitrogen and oxygen production are linearly correlated to plasma power for 13.56 MHz and 27.12 MHz. At 40.68 MHz this begins to deviate at high plasma powers. Figure 5.5b exhibits roughly the same atomic oxygen density for the same plasma power regardless of frequency, but as the plasma power increases above 5 W the trend in O production is not matched. This behaviour of retarded production of atomic oxygen at high plasma power is shared with atomic nitrogen.

This deviation at higher plasma power for 40.68 MHz can be for numerous reasons. Most considerable is the assumption that the EEDF is invariant, however it is not clear if this is the case. The EEDF may begin to change, which alters the rate at which molecular species are dissociated. Simulations of dual frequency operation [171] suggest a drop in the high energy tail of the EEDF. Unfortunately without measurements of the electron energy distribution it is not possible to confirm nor deny this.

5.2.2 Efficiency in reactive species production

If increased operating frequency (and therefore increased operating plasma power) does not lead to a direct linear increase in plasma produced reactive species, which frequency is most energetically efficient at producing atomic nitrogen and atomic oxygen?

To assess the efficiency of the plasma at producing reactive species at various frequencies, the number of reactive species produced per joule of energy is scrutinised. This crude technique uses the fact that there is 1 slm of gas throughput in the system to convert from Watts to Joules, using Equation 5.1. Energy lost into other mechanisms such as gas heating rather than making and breaking bonds leads to inefficiencies. The most efficient plasma would be one where all energy deposition goes only into dissociating molecular species into atomic species in this case.

$$\frac{\text{Atoms}}{\text{Joule}} = \frac{\text{Density} \cdot \text{Flow Rate}}{\text{Power}} \quad (5.1)$$

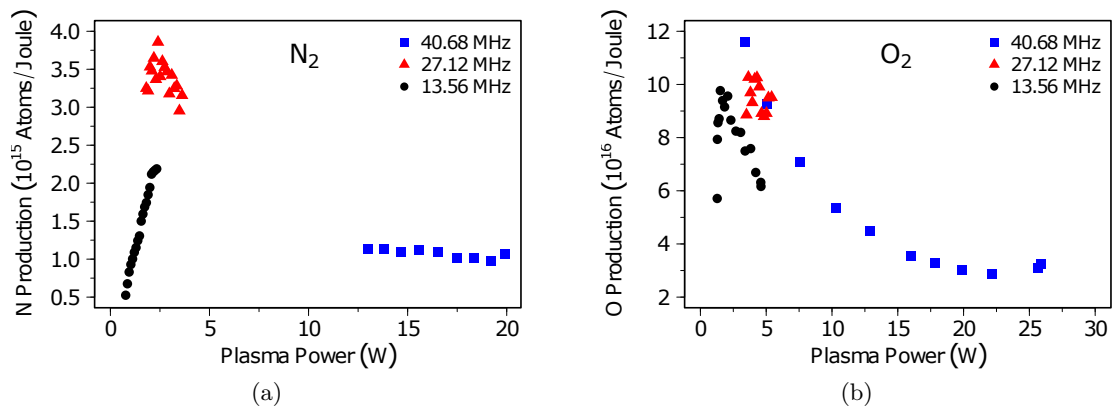


Figure 5.6: Energy efficiency for the three operating frequencies at producing N (a) and O (b) in the μ -APPJ. Higher values are better. Higher plasma powers correlate with poor energy efficiencies.

Surprisingly for both N and O production in the μ -APPJ, in Figure 5.6 there appears to be a most efficient plasma power of ~ 2.5 W for producing atomic species. For higher plasma powers using 40.68 MHz the efficiency is lower, as well as lower plasma powers using 13.56 MHz. This measure of energy efficiency implies that using 27.12 MHz is broadly speaking the most efficient choice at producing reactive species under these operating conditions.

Many large scale applications need efficiency when producing radical species to be cost effective. Some niche applications however rely on the absolute density of reactive species. For example the treatment of cancer requires a particular “dose” [8], and densities below a certain threshold may actually enhance the growth of cancer cells, which is clearly not ideal. Bio-medical applications though require low gas temperatures and high frequency operation is not an option as the gas temperature is typically higher than at low frequencies. To attain

better efficiency while producing high reactive species densities at low gas temperatures borders on the subject of tailored waveforms and frequency mixing, which goes beyond the scope of this investigation. However, this work does show that such optimisation is likely to be possible by changing the voltage waveform, either through simply varying the frequency or through explicitly tailoring the voltage waveform.

5.3 Operating modes

In Chapter 4 it was demonstrated that the μ -APPJ is capable of operating in a hybrid $\alpha - \gamma$ mode. It has been postulated that the use of different frequencies can invoke a true γ -mode in other APPJs [149]. A helium only plasma is operated across the frequency range, and once again the power dissipated at the same driving voltage is greater for higher frequencies. This is shown in Figure 5.7 where the power-voltage characteristics are plotted for the μ -APPJ under operation with helium feedstock only at the three different driving frequencies. In Figure 5.7, the ignition voltage decreases with frequency as anticipated, but the approximate range in ignition powers is only 1 W (0.25 W, 0.4 W, and 1.25 W as frequency is increased).

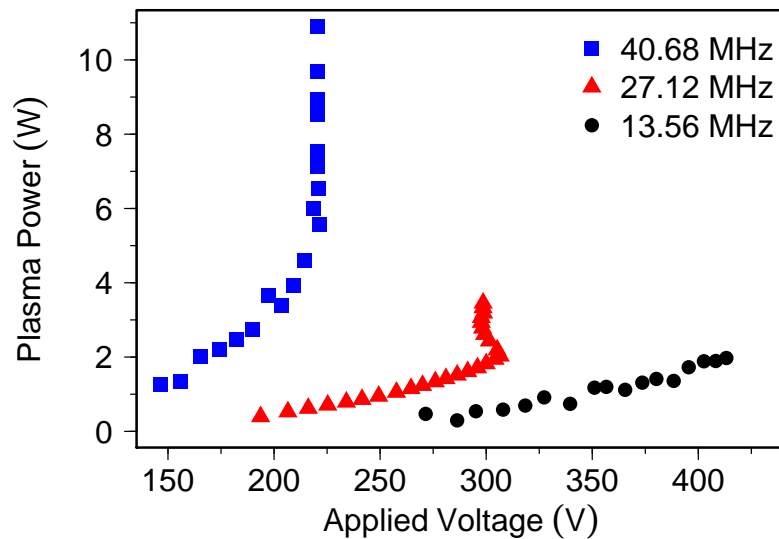


Figure 5.7: Plasma power at the three frequencies used for a helium only discharge. For higher frequencies, the voltage begins to decrease for greater operating power, indicating a true mode transition into the γ -mode regime.

Operating with only helium with no admixtures of nitrogen or oxygen (apart from impurities) reveals operating modes that exist at higher frequencies but not at 13.56 MHz. With typical admixtures of 0.3% nitrogen or 0.5% oxygen, the plasma reaches an arcing mode rather than exhibiting this new behaviour, and therefore no additional molecular species were added for this investigation. In Figure 5.7 the voltage turns over with increased plasma power for 27.12 MHz and 40.68 MHz, indicative of a true γ -mode operation.

The mode change can be assessed by interrogating the resistance and reactance response for these two frequencies. Both Figures 5.8 for 27.12 MHz and 5.9 for 40.68 MHz demonstrate a dramatic change in both resistance (a) and reactance (b) at a certain voltage. In Figure 5.8 the turning point occurs at 306 V, a plasma power of 2 W, and increases for another 1.45 W before operation of the plasma was stopped to minimise damage from heating. For Figure 5.9, the plasma power is 5.6 W at 222 V, continuing to 10.9 W maximum power before arbitrary shutdown. The shutdown point was defined as when the plasma reached an arcing mode, or if electrode temperature (measured using a simple infrared thermometer) reached 90 °C. The glass temperature for the PEEK housing material is ~ 150 °C, and so temperatures were kept below this to avoid damaging the jet. For the higher frequencies no arcing mode was found to develop, yet as a large amount of power can be dissipated in the external circuitry through the matching and parasitics it is essential to stop operation to minimise any thermal damage.

The explanation for the observed trends in resistance and reactance is the same as for the 13.56 MHz case discussed in Section 4.4.7. The sheath region is decreasing in size, and therefore bulk width is increasing. This gives rise to greater resistance from the bulk, but also greater resistance from ion heating in the strong sheath electric fields.

From the comparison of resistance and reactance to PROES measurements at 13.56 MHz, discussed in Section 4.6, it was observed that the electron heating dynamics changed substantially during the mode transition into the hybrid α - γ mode. It is important to carry out the same comparison here for the higher frequencies, particularly as they allow for the transition into the true γ -mode, which has not been studied previously in the μ -APPJ.

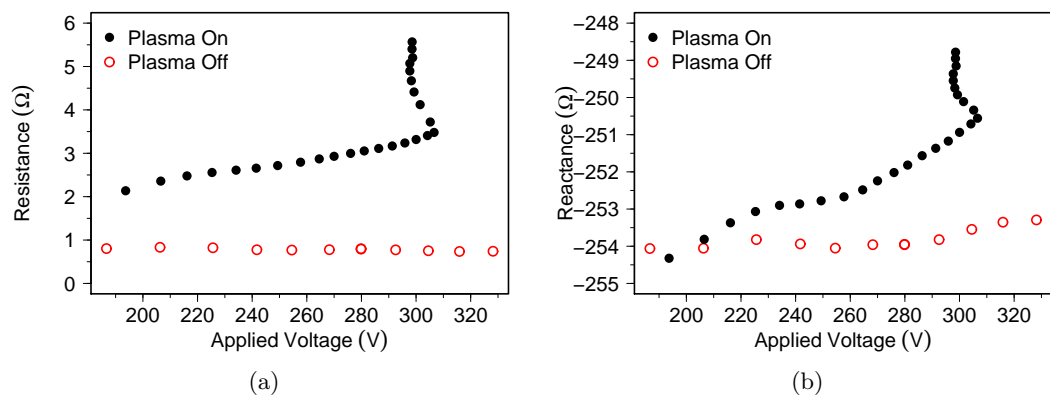


Figure 5.8: Both resistance (a) and reactance (b) indicate two modes of plasma operation at 27.12 MHz with helium only. Both increase steadily to begin with, indicating standard α -mode operation as with 13.56 MHz. At 306 V, the power increases despite decreasing driving voltage which is consistent with γ -mode operation.

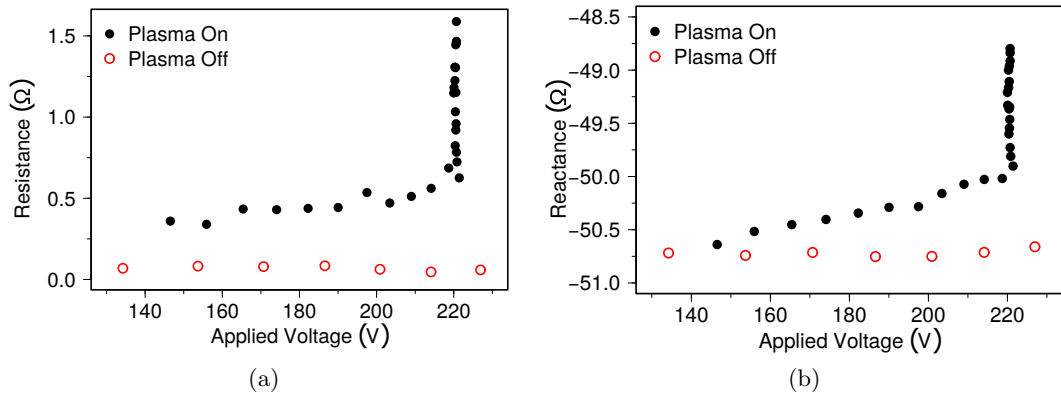


Figure 5.9: Both resistance (a) and reactance (b) indicate two modes of plasma operation at 40.68 MHz with helium only. Both increase steadily to begin with, indicating standard α -mode operation as with 13.56 MHz. At 222 V, the power sharply increases despite the voltage decreasing only slightly.

5.3.1 Comparison to PROES

The turn over of voltage is most pronounced at 27.12 MHz, and will therefore be used in this test. An added bonus of performing PROES at this frequency is that offers slightly better spatial resolution, due to larger plasma structures. As shown in Figure 5.2 the emission originates closer to the electrodes at 40.68 MHz, ultimately making interpretation of PROES images not as obvious. The time integrated emission from the plasma at the helium 706 nm line can show where the heating is taking place and if the sheath is indeed shrinking in concordance with the electrical measurements. The emission at 706 nm results from the electron impact excitation of helium into the $\text{He}(3s^3S)$ state, requiring energies above 22.7 eV.

Figure 5.10 has emission originating from closer to the electrodes as power increases, but at high power densities where the voltage turns back (c) the emission is dominated by contributions from within the sheath. This intra-sheath emission is a credible marker of a γ -mode operation, where the heating from inside the sheath is greater than that of the bulk.

The final evidence of the presence of a true γ -mode is seen in Figure 5.11. As the quenching coefficients for this emission line are not known, the PROES images presented are in fact the raw emission at 706 nm, rather than the corrected excitation. At elevated pressures, it is often inconsequential to use the raw emission for qualitative purposes, as the lifetimes of the excited species are very short, and still highlight easily where emission originates. Using actinometry, it has been estimated that the lifetime is ~ 6 ns [132], which is short enough to be able to resolve different excitation structures through emission alone.

As power density increases from 5.11a ~ 0.5 W, to (b) ~ 1 W, the heating by sheath expansion (region I) begins to be shared by that of intra-sheath heating (region III). Emission from sheath collapse (region II) appears to be very small, in concordance with PIC simulations at 27.12 MHz [150]. As power is further increased in (c) (~ 2 W) the emission from

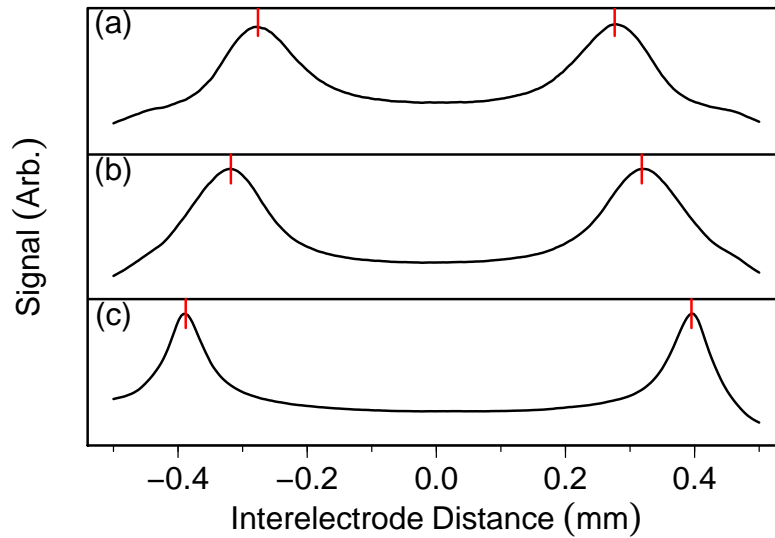


Figure 5.10: Time integrated emission at 706 nm for 27.12 MHz He only plasma. Sheath constricts at low density ~ 0.5 W (a) to high power densities ~ 2 W (b), before finally entering a γ -mode regime and emission is dominated by intra-sheath excitation (c) at ~ 3 W.

secondary sheath electrons is dominant. Once the voltage turns over, emission is exclusively by electron impact excitation in the inner sheath [150, 159] (see Figure 5.11d). The sheath is heavily constricted and emission originates very close to the electrodes.

Observation of the γ -mode has been limited to helium only operation, a limitation that has been documented previously with other atmospheric discharges [146]. The consequence is that even if it does enhance the plasma chemistry suitably as some have predicted, the associated complications from power and heat management, as well as reduced input gas control due to the very small possible admixtures makes it an unlikely mode of operation for the μ -APPJ or the EU COST jet reference [12]. Nevertheless, the more accessible hybrid-mode observed in Chapter 4 could be utilised to promote reactive species production.

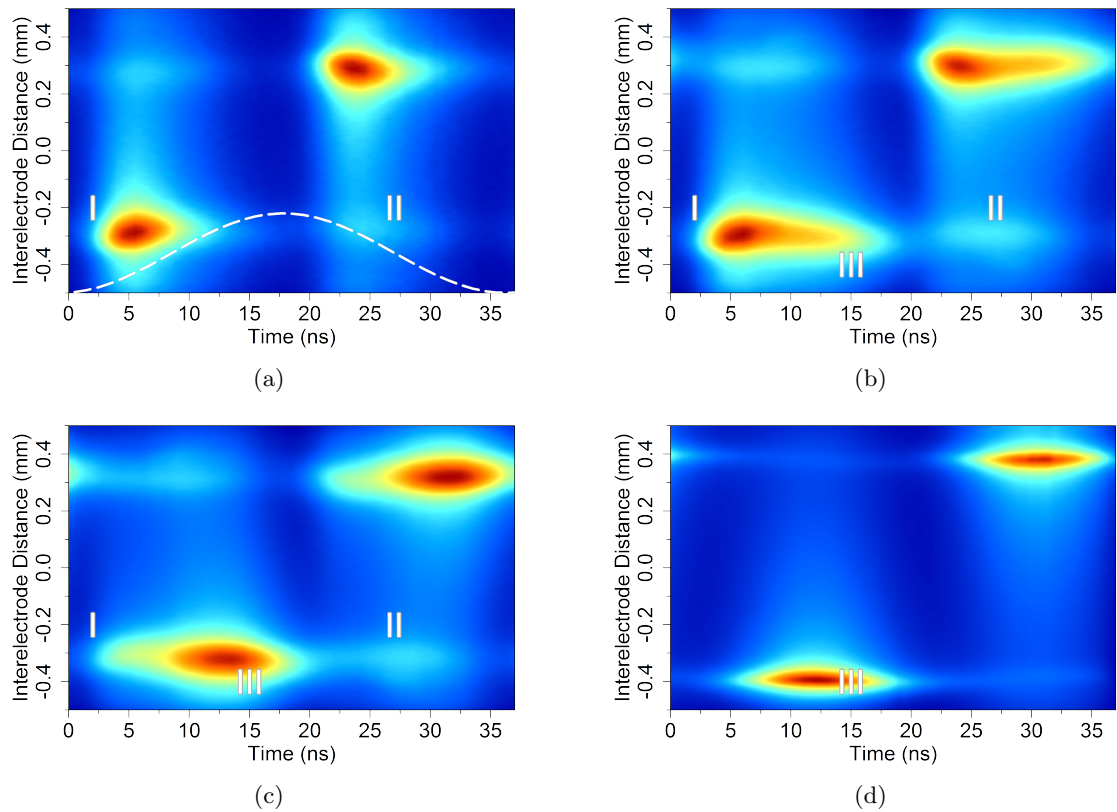


Figure 5.11: The excitation is shown as a function of both space between electrode (vertical axis), and time throughout one 27.12 MHz RF cycle (horizontal axis). Each is normalised to the maximum value, with blue being the lowest value and red the highest value of excitation. Excitation in region “I” is a consequence of sheath expansion, where as excitation in region “II” is due to sheath collapse heating. Region “III” indicates intra-sheath energy deposition. As power density increases from (a) ~ 0.5 W, (b) ~ 1 W, (c) ~ 2 W, the heating from sheath expansion (I) begins to be shared with intra-sheath heating (III). Finally in (d) as the voltage decreases with greater power density (~ 3 W), heating comes almost exclusively from inside the sheath only. This verifies a true γ -mode operation. (a) shows a dashed line to represent how sheath extent changes over an RF cycle, however this is merely to guide the eye, and has not been explicitly calculated.

5.4 Summary

For the first time, the μ -APPJ has been operated and characterised at other harmonics of 13.56 MHz in terms of both dissipated power but also reactive species densities. Higher operating plasma powers can be utilised for lower operating voltages with the application of higher driving frequencies. The resulting greater electron densities can in turn produce more reactive chemistry.

Higher reactive species densities can be achieved by using higher driving frequencies up to 40.68 MHz. Changing the frequency allows for an extension of the range in which the μ -APPJ can be operated in α -mode, giving another knob with which investigators can tailor the plasma to produce the reactive species densities desired. This has particular relevance to those investigating tailored waveforms, and how frequency can control plasma dynamics.

The unique combination of power measurements at these experimentally challenging driving frequencies, along with the capability to measure densities of reactive atomic species accurately in the effluent, has led to the estimation of production efficiency in the μ -APPJ, which has not been often considered previously. This also reveals that there is perhaps an optimum plasma power density that suits the production of atomic oxygen and atomic nitrogen at between 2.4 W to 2.5 W. Further investigation is required into the role of the electron energy distribution function at different frequencies and what role that has on reactive species production besides the mere raw increase in electron density.

Operation at higher frequencies also opens up the possibility for true γ -mode operation. This intra-sheath dominated heating mode has not been previously observed in the μ -APPJ. At both 27.12 MHz and 40.68 MHz it is possible to see enhanced plasma power for reducing applied voltage in helium only discharges, which was then confirmed by phase resolved optical emission spectroscopy.

Chapter 6

Using the Effluent of the μ -APPJ to Etch Photoresist

The μ -APPJ geometry is destined for use in applications, and now the plasma chemistry is better defined, it is possible to link optimisation of these processes to the plasma chemistry. This also provides a test of the μ -APPJ's efficacy in "real-world" scenarios.

The removal of photoresist is a common industrial application of low-pressure plasmas [20,21,183,184], and was a motivation behind developing the first RF atmospheric-pressure plasma devices [27,28] to mitigate the use of vacuum equipment which is an additional capital and operating cost, limiting wafer processing to batch production.

Photoresist is used as a mask to control where etching and deposition on a substrate may take place for industries such as semiconductor manufacture. It consists mainly of long chain hydrocarbons, and is photosensitive to UV light. Photoresist is coated over a substrate, typically using spin-coating. Figure 6.1 demonstrates how photoresist can be used to preferentially etch a substrate, allowing for complex architectures. Once the photoresist is coated over the substrate, a desired pattern is set into the photoresist by focussing down an image of the desired layout using UV light passing through a mask in a process called UV lithography. The photoresist then softens (positive resist) or hardens (negative resist) in response to the UV light. During etching of the substrate, the soft photoresist is etched quickly to reveal the substrate, whereas the hardened resist acts as a sacrificial barrier, protecting the substrate underneath.

After plasma processing of the substrate, any remaining hard photoresist has to be removed. For modern complex semiconductor architectures many steps are required, each with a particular pattern that must be etched or deposited. Residual photoresist can inhibit these processing steps and ultimately lead to defective products [184,185]. Photoresist is a vital tool in semiconductor manufacture, however it must be completely removed after every application when producing modern devices.

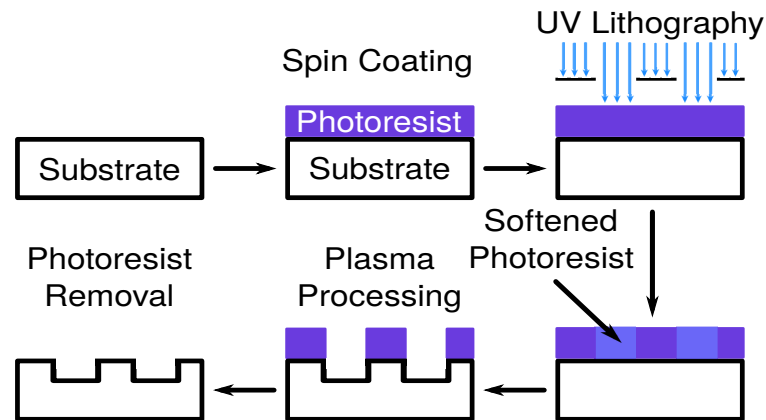


Figure 6.1: Positive photoresist is spin-coated onto a substrate, and is exposed to UV light with a particular pattern. The positive photoresist softens under exposure to UV, which is more susceptible to etching. Photoresist then acts as a sacrificial protection of the substrate to allow preferential etching of the substrate where the photoresist has been softened during UV lithography. Once the plasma processing is complete, the residual photoresist is removed to leave the desired substrate topology.

6.1 Removing photoresist

Dry plasma etching of photoresist (referred to as ashing or stripping) using a plasma is often preferred over wet chemical etching during semiconductor manufacture. Traditionally, an oxygen containing inductively coupled plasma (ICP) is formed in contact with the wafer and chemical etching along with physical removal takes place to ash away the remaining photoresist. When the sheath forms at the surface of the substrate, ions are accelerated via the high sheath electric fields and impact the surface. This ion bombardment is effective at removing photoresist, however it causes collateral damage to any exposed wafer architecture [20, 184].

In accordance with the International Technology Roadmap for Semiconductors, the feature size available in current high end processors, such as Intel’s Skylake architecture, is on the order of 14 nm. Silicon forms a diamond structured lattice with a cubic cell length of 5.43 \AA [186], and so 14 nm features contain only just over two dozen repeating unit cells, equivalent to around just 200 atoms for features one crystal cell wide and thick. These feature sizes will continue to shrink, with the next milestone to be met set at 10 nm. Indiscriminate ion bombardment of the surface may cause irrevocable damage to the substrate architecture at these minute feature sizes containing very few atoms.

To mitigate damage through ion bombardment when the sheath forms at the substrate, “downstream” methods have been adopted [187], where the plasma produces reactive species separately from the treatment surface, and these reactive species are transported downstream in the gas flow to the treatment surface. Oxygen species react with the hydrocarbon based resist to mostly form volatile products such as carbon dioxide and water vapour [20, 184]

which are subsequently removed by the bulk gas flow. These reactive species are able to selectively etch the photoresist without physical removal of the important substrate material. Unfortunately downstream methods suffer from slower removal rates of photoresist when compared to direct plasma contact, due to the lack of synergy that normally occurs between chemical and physical removal [22]. For downstream removal of photoresist, the etch rates are on the order of Å/min to tens of nm/min [188], compared to hundreds of nm/min to $\mu\text{m}/\text{min}$ when the plasma is in contact [20].

6.1.1 Plasma ashing at atmospheric-pressure

Photoresist ashing at atmospheric-pressure removes the need for expensive vacuum equipment, and can increase the throughput rate in manufacture, the motivation behind the first RF APPJ [27, 28]. Previous investigations into utilising atmospheric plasma devices have shown they are effective at etching photoresist [35, 189–192], with high selectivity [28]. These devices show removal rates ranging from 100 nm/min to $< 1 \mu\text{m}/\text{min}$. Some of these systems, particularly with high etch rates, have an active plasma effluent or form a plasma in direct contact to the substrate surface, resulting in sheath formation and the possibility of ion bombardment taking place and damaging the substrate topology.

The μ -APPJ effluent offers high densities of reactive species, which will promote fast chemical etch rates, without direct plasma contact and the risk of ion bombardment, analogous to the low-pressure downstream case. This is twinned with the additional benefits of operating at 1 atm and reducing operating costs associated with vacuum equipment. This feasibility study will highlight any promise for removing photoresist using only the neutral radical rich effluent of an atmospheric-pressure plasma jet.

6.2 Measuring etching rate of photoresist

Positive novolac based S1813 photoresist is spin-coated onto silicon wafers to a thickness of $1.5 \mu\text{m}$ and baked as per the manufacturer's recommendations. Positive resist is commonly used in these types of investigations [35, 189–191, 193] as it mimics the hardened photoresist residue left on the surface after plasma processing. As well as ellipsometry, the thickness was verified using a surface profile analyser. The μ -APPJ is mounted on a 3-axis motorised stage with the exit of the jet facing downwards towards the treatment surface. The wafer is placed under the exit of the μ -APPJ, and the time is recorded until the optically discernible silicon wafer underneath is visible. The silicon wafer has a metallic appearance that differentiates it from the coloured photoresist. This can be seen in Figure 6.2. Using the known photoresist thickness and measured etch through time, the vertical rate of removal is calculated in nm/min. The error in measured etch rate is dominated by the human response time in measuring the etch through time, at around $\pm 2\text{s}$.

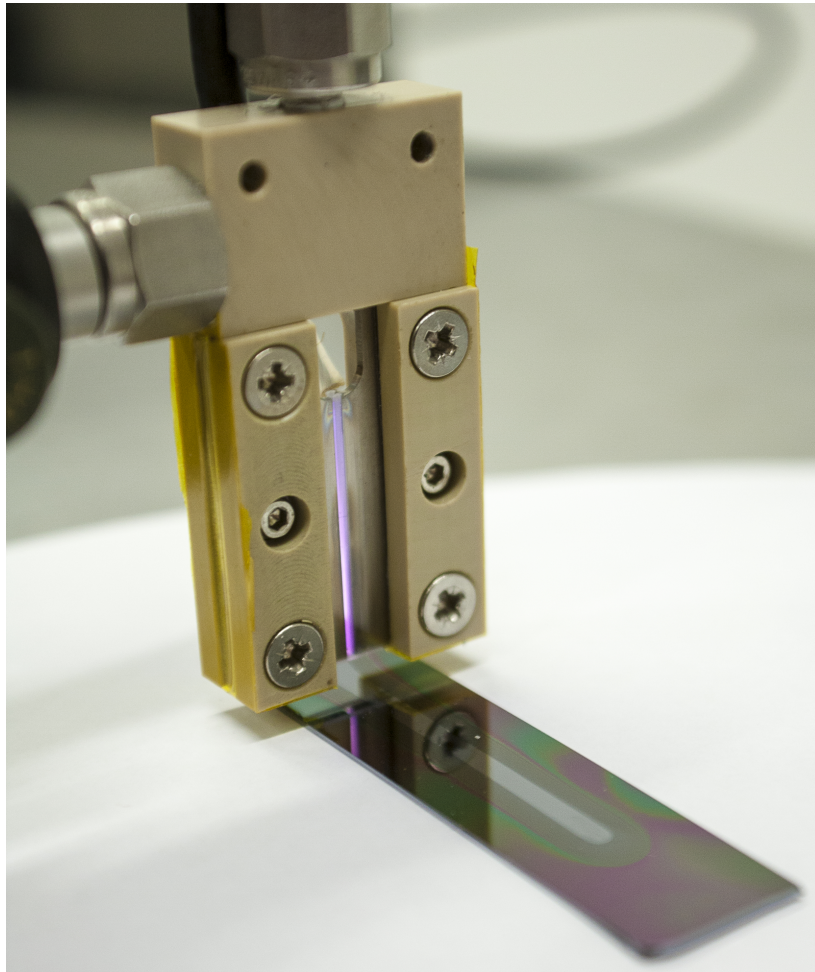


Figure 6.2: Photograph of the APPJ above a photoresist coated Si wafer sample, where the PR has been removed, the Si is visible. The jet can be moved to provide spatially defined PR removal.

6.3 Preliminary optimisation

Oxygen containing plasmas are used at low-pressure for photoresist ashing, and accordingly it makes sense for the μ -APPJ to be operated with molecular oxygen admixtures to produce the same relevant reactive species. During preliminary testing, the optimum admixture found was 0.5% O₂, and held constant throughout. It was also observed that the etch rate diminished rapidly with increased distance between the jet exit and the treatment surface, a behaviour witnessed in other investigations [194]. Using the 3-axis motorised stage, the distance could be precisely reduced to promote faster etch rates. At distances comparable to that of the interelectrode distance, the helium feed gas leaving the jet can form a discharge between the surface and powered electrode of the jet. A core motivation for using the μ -APPJ is the ability to produce reactive species without a direct plasma in contact with the treatment site, as ion bombardment can damage the substrate. The distance was kept at 3 mm to maintain high etch rates by keeping the substrate as close to the jet exit as possible, while having the assurance of not forming an unwanted discharge at the surface.

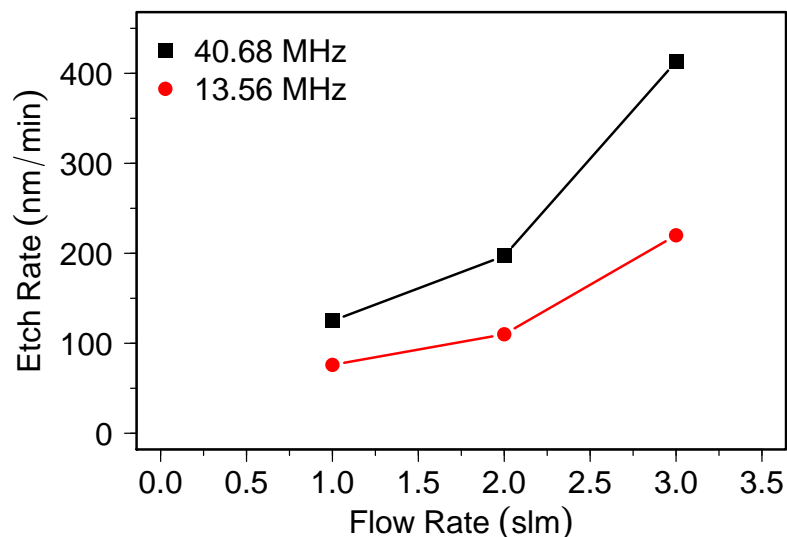


Figure 6.3: Etch rate of photoresist for 13.56 MHz and 40.68 MHz. 40.68 MHz outperforms 13.56 MHz for the same parameters of 0.5% O₂ in He, and 20 W generator input power.

Figure 6.3 shows the measured etch rate for helium with 0.5% O₂ admixture at both 13.56 MHz and 40.68 MHz. The higher driving frequency was found to always outperform 13.56 MHz for the same operating parameters of flow rate, jet to sample distance, and power. As a consequence of these preliminary findings, to maximise photoresist etch rates the frequency used was 40.68 MHz with a feed gas of helium with 0.5% O₂, and a jet exit to surface distance of 3 mm.

6.3.1 Influence of UV emission

Positive photoresist is softened in the presence of UV light between the range of 300 nm to 500 nm, requiring a dose of 120 mJ/cm^2 according to the manufacturer for a thickness of $1.5 \mu\text{m}$. The μ -APPJ produces some UV emission that could soften the resist and enhance etch rates. It should be acknowledged that during normal plasma processing the plasma may emit UV while the substrate is being etched, but the photoresist is still able to act as a sufficient barrier to allow for localised substrate etching. Previous investigations into the role of UV in biomedical treatments using the μ -APPJ have found no noticeable effects when UV is solely used [38,195], yet there may be synergistic effects when UV and reactive species are used together. Though it may not be a concern during plasma processing, UV emission could still cause positive as well as detrimental effects [20] to removal rates during ashing.

Figure 6.4 shows optical emission spectra for the μ -APPJ operating at 13.56 MHz with a helium and 0.5% O_2 admixture, using an irradiance calibrated Ocean Optics HR4000, with the optical fibre placed 2 mm from the quartz window near the jet exit, with emission encompassing the full numerical aperture. The emission is dominated by helium lines and atomic oxygen lines between 700 nm to 850 nm. There is near negligible emission in the photoresist relevant range of the spectrum. Integrating between 300 nm to 900 nm, the intensity is on the order of $< 0.05 \mu\text{W/cm}^2$. With preliminary etch rates on the order of 200 nm/min, during the full etch time the equivalent dose even with the most intense lines is around 0.02 mJ/cm^2 . Comparing this to the required 120 mJ/cm^2 , it is clear that the practically non-existent UV contribution from the μ -APPJ, and even the VUV contribution [45,196] can be disregarded in this work.

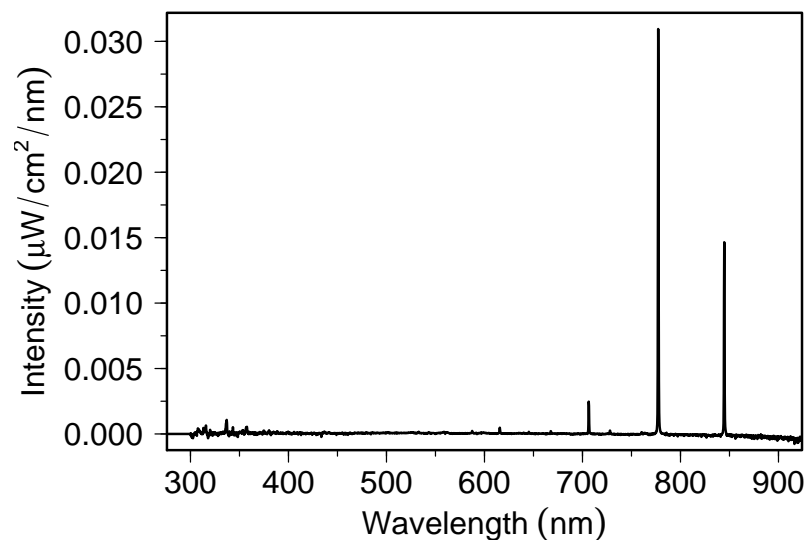


Figure 6.4: Optical emission spectra for a helium with 0.5% O_2 discharge at 13.56 MHz. Emission is present at He 706 nm, O 777 nm, and O 844 nm, however there is negligible optical plasma emission in the photoresist relevant 300 nm to 500 nm range.

6.4 Results

Figure 6.5 shows an increase in etch rate with greater applied generator power, with maximum achievable etch rates for 3slm flow rate approaching $1\ \mu\text{m}/\text{min}$. Input power can act as a control on etch rate, however issues such as thermal damage to equipment and the risk of forming an undesired arcing mode means that the power can not be continually increased to render higher etch rates. Enhancement of etch rate must be produced via other means.

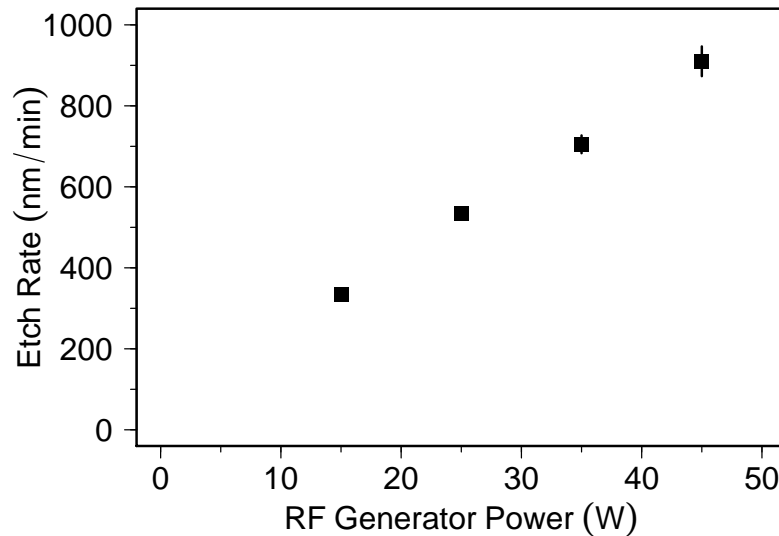


Figure 6.5: Measured etch rate at varying RF input powers at 40.68 MHz with a gas supply of 3slm He and 0.5% O_2 admixture. Etch rate increases linearly with input generator power.

Figure 6.6 demonstrates an increase in etch rate of photoresist when the flow rate is increased. At 3slm an etch rate of nearly $1\ \mu\text{m}/\text{min}$ is possible, which is doubled to almost $2\ \mu\text{m}/\text{min}$ at 7slm for the same gas mixture of helium with 0.5% molecular oxygen admixture. For flows of 10slm and above, the visible metallic silicon etch area becomes distorted, with some photoresist remaining as can be seen in Figure 6.7.

When considering the Reynolds number for a helium flow of 10slm and the $1\ \text{mm} \times 1\ \text{mm}$ square exit of the μ -APPJ, the flow of $\sim 170\ \text{m s}^{-1}$ is no longer in a laminar regime (Reynolds number of 2000). The semi-turbulent flow may be responsible for the irregular etch profile across the substrate. As uniformity and predictability are clearly important for industrial applications, the flow rate must be limited to maintain a uniform etch area, putting an effective upper limit on how far the etch rate can be improved upon by optimising flow.

A common technique in low-pressure removal of photoresist is to heat the substrate to temperatures as high as $200\ ^\circ\text{C}$ to promote surface reactivity and ashing rates [1, 184, 187]. The softbake temperature of photoresist is around $100\ ^\circ\text{C}$ to $115\ ^\circ\text{C}$, and at temperatures greater than this, the reactivity (and therefore etch rate) is expected to improve dramatically.

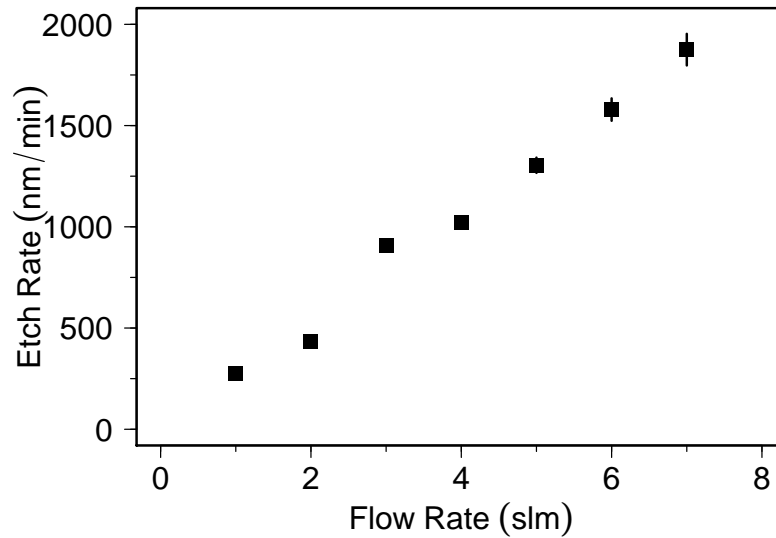


Figure 6.6: Etch rate has a positive correlation with flow rate. Input generator power was held constant at 45 W and gas composition of 0.5% O₂ in helium.

The substrate was placed on a hotplate and the etch rate assessed for a flow of 7 slm helium with 0.5% O₂ and a generator power of 45 W. At 65 °C no noticeable change was observed in the removal rate of photoresist. At 100 °C the etch rate had increased by a few tens of percent. However at 140 °C, past the softbake temperature, a significant increase was observed. The etch rate measured was 10 μm/min, a five fold increase from 2 μm/min in the no external heating case. An etch rate of 10 μm/min is around two orders of magnitude faster than the tens of nm/min expected in low-pressure downstream removal.

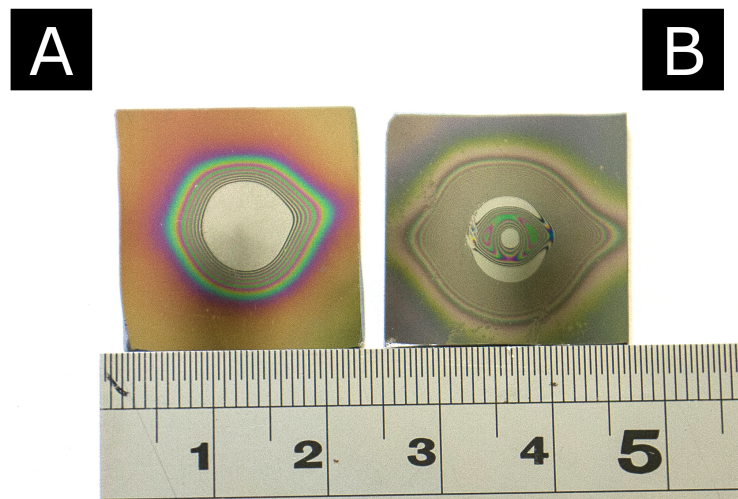


Figure 6.7: Image of etch area after treatment at (a) 7 slm and (b) 13 slm. The etch area is ~ 10 mm in diameter in (a), with a larger partially etched area visible via the Newton's rings phenomena, known in industry as *Bull's-eye* [197]. In (b) the etch area is not completely clear of photoresist, and demonstrates a slight asymmetry due to the geometry of the μ-APPJ.

6.4.1 Etch quality

The μ -APPJ is capable of removing photoresist orders of magnitude faster than in downstream low-pressure systems, but in modern semiconductor manufacture residue from photoresist is an obstacle in producing complex architectures. Though speed is an important factor in industrial processing, the quality of the final product is also of great consideration.

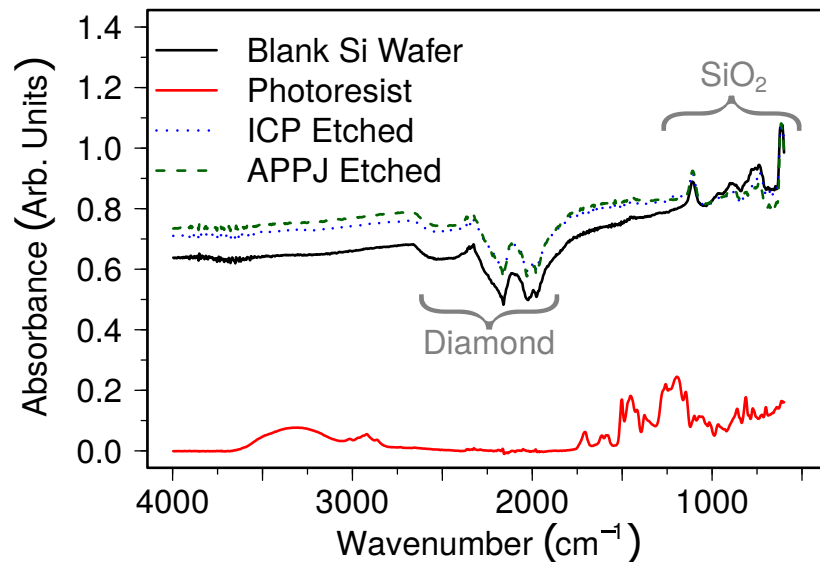


Figure 6.8: ATR-FTIR spectras for Si wafers before treatment, with photoresist, and after treatment. The ICP treated (dotted) and μ -APPJ treated (dashed) show the same surface chemistry.

Figure 6.8 shows Attenuated Total internal Reflection Fourier Transform Infra-Red (ATR-FTIR) absorption spectra (using a Bruker VERTEX 70) for a clean silicon wafer surface, a sample of silicon wafer spin-coated with photoresist, and two samples where the photoresist has been ashed away. The first is with a traditional low-pressure oxygen ICP, the second is with the μ -APPJ. ATR-FTIR is capable of measuring monolayers of photoresist and has been used previously as a diagnostic of surface chemical quality [183]. Broadband infrared radiation passes via total internal reflection through a diamond crystal which is in contact with the sample substrate, and the evanescent wave that enters the sample substrate provides a characteristic spectra.

The absorption spectra for the plasma etched cases show practically identical signatures, which match that of the pure silicon wafer. The organic signatures between 1800 cm^{-1} to 500 cm^{-1} and the broad feature at 3300 cm^{-1} that are characteristic of novolac resin based photoresist are not visible after being removed using either traditional low-pressure ICP or the effluent of the μ -APPJ. This indicates that the μ -APPJ can remove photoresist to as high a quality as is expected in industry when using traditional low-pressure ashing.

6.5 Reactive species responsible for atmospheric ashing

The rate of chemical etching R of a substrate s by species x [20] is given by

$$R_{s(x)} \propto \Gamma_x e^{-E_a/k_b T_s} \quad (6.1)$$

where E_a is the activation energy, k_b is the Boltzmann constant, T_s is the substrate temperature, and Γ_x is the convolution of reactive species density n_x and the rate they impinge the surface ν_x [198]. By increasing the reactive species density, the flow rate to the surface, or both, the rate of etching should increase. Modelling [198] and experiments [18] at low-pressure have implicated atomic oxygen as the reactive species responsible for etching photoresist. Atomic oxygen leads to random chain scission of the long hydrocarbons into volatile species [20, 183] which then leave the surface. This behaviour has also been documented at atmospheric-pressure [191, 199]. With the well characterised plasma chemistry of the μ -APPJ, it is possible to examine if atomic oxygen is the principal reactive species for photoresist removal in this investigation.

It is known from Chapter 5, as well as previous studies [2, 60], in the μ -APPJ atomic oxygen density increases with greater power for a given operating frequency. This behaviour is consistent with observed etch rate, i.e. with higher power the etch rate increases. In Chapter 5 it was also demonstrated that the atomic oxygen density is greater for higher frequencies, and greater etching is found to correlate with higher driving frequencies (see Figure 6.3). Studies using TALIF [3, 47, 59], optical emission spectroscopy [199, 200], molecular beam mass spectrometry [48], and modelling [60, 66] show that atomic oxygen density decreases rapidly with larger distances from the jet exit. This can explain the result that when the jet exit is further away from the surface the etch rate decreases, as seen during preliminary testing. This lends support to the conclusion that atomic oxygen is important for photoresist removal with strong correlation between O density and etch rate at this point.

Increasing flow rate will increase the rate at which atomic oxygen reaches the photoresist ν_x , increasing etch rate in accordance with Equation 6.1, but it also reduces the residence time in the plasma, possibly reducing the density of etchant species n_x . In the core plasma, there is a minimum required time for the plasma chemistry to equilibrate. In the μ -APPJ the equilibrium time for atomic oxygen production in a He + 0.5% O₂ gas mixture is 0.6 μ s at 1 slm [2]. Considering the gas speed at flow rates above 3 slm, this criteria is no longer met and O densities may become significantly diminished as a result. Using TALIF, the relative density of O impinging the surface can be measured to assess whether the convolution of flow rate and density predicts an increase in flux to the surface. A measured increase in flux would be consistent with the increase in etch rate observed in Figure 6.6.

Figure 6.9 shows relative densities of O measured with TALIF less than 0.5 mm above the surface as it is being etched at 13.56 MHz. The relative density does indeed decrease

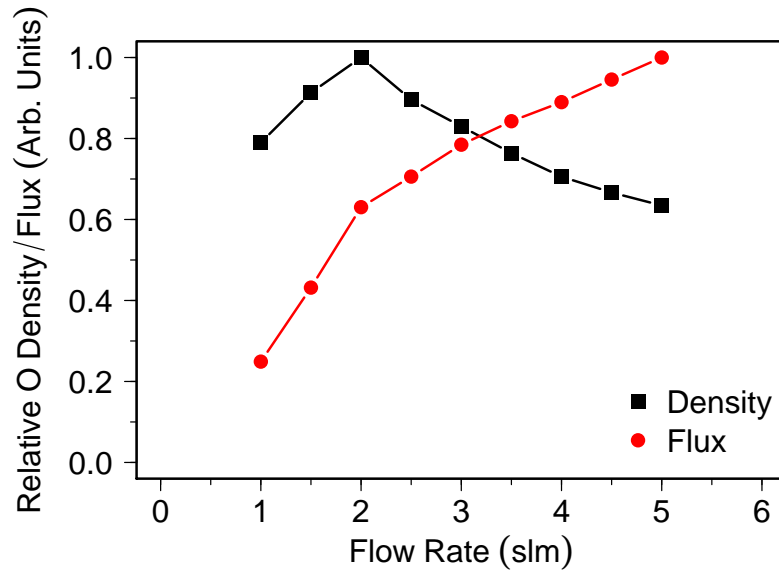


Figure 6.9: TALIF measurements of relative atomic oxygen density at 13.56 MHz less than 0.5 mm above the treatment surface as it is etched. The decrease in residence time leads to a decrease in density after 2 slm, however the overall flux of atomic oxygen to the surface increases.

after a given flow rate of 2 slm, most probably due to the decreased residence time in the core plasma. When the density is multiplied with flow rate however, the overall relative flux of atomic oxygen is still increasing despite the reduced density. This increase in reactive species flux with flow is concordant with measured etch rates, bolstering the correlation between etch rate and atomic oxygen.

Singlet delta oxygen (SDO) shares similar characteristics to atomic oxygen formation outside the plasma channel. The density is expected to decrease rapidly from the jet exit [66], and increase with applied power, and also flow rate [62], akin to what is found with atomic oxygen. SDO however is inconsistent with the optimum admixture found for etching, as small admixtures of molecular oxygen should yield the highest densities of SDO [62] and therefore highest etch rates, which was not observed. For photoresist etching using the μ -APPJ a maximum in etch rate was found at 0.5% O_2 admixture, equivalent to peak atomic oxygen production [2]. Ozone is also a possible candidate at atmospheric-pressure (the rate of three body production required is too small for it to be considered in low-pressure systems). Ozone is expected to increase in density with greater distance from the jet exit [48, 66] and also expected to be more abundant at lower power and frequencies due to less gas heating, which is contradictory to observed behaviour in etch rate. This makes O_3 an unlikely candidate as the dominant etch mechanism at atmospheric-pressure in this scenario. It can be said with confidence that atomic oxygen is the likely driver behind atmospheric etching of photoresist using the effluent of the μ -APPJ.

6.5.1 Comparison to low-pressure ashing of photoresist

Now it is understood that atomic oxygen most probably regulates etching, this can partially explain the two orders of magnitude greater etch rate with the μ -APPJ compared to low-pressure downstream etching. The atomic oxygen density in a typical low-pressure discharge is between 10^{18} m^{-3} to 10^{19} m^{-3} [18,201]. In comparison, even though molecular oxygen is a very small fraction of the working gas at atmospheric-pressure, the O density is between 10^{21} m^{-3} to 10^{22} m^{-3} as shown in Chapter 5. The atomic oxygen density is three orders of magnitude greater for the μ -APPJ, which implies the etch rate is proportional to O density.

Though plasma power measurements are not reported in this feasibility study, in Chapter 5, the measured power for 0.5 % O_2 at 40.68 MHz is on the order of 20 W, with significant losses into a broadband Pi-matching network responsible for the discrepancy between generator power and plasma power (as discussed in Chapter 4). This results in a power per unit area comparable to that of traditional low-pressure removal, however the etch rate is two orders of magnitude faster.

6.6 Summary

With etch rates up to $10 \mu\text{m}/\text{min}$ attainable, the μ -APPJ can etch photoresist much faster than downstream low-pressure systems, while still mitigating damage via ion bombardment. This is with the additional benefits that come with operating at atmospheric-pressure, such as no requirement for vacuum equipment to operate. Moreover, the μ -APPJ uses less power and less gas consumed for equivalent area than other atmospheric photoresist removal devices [35,191,192,194], despite using only chemical etching.

The etch rate can be optimised through the adjustment of atomic species densities via operating parameters such as power, gas mixture, driving frequency, and distance from the jet exit to the treatment site. The rate at which O reaches the surface can be tailored using the flow rate, further allowing for further modification of the etch rate. Finally, the substrate temperature can be used as a very sensitive control over etch rate.

The known characteristics of the μ -APPJ has allowed for a deeper understanding as to the mechanisms behind photoresist removal at atmospheric-pressure. Future devices can tailor operating parameters to maximise atomic oxygen production and therefore maximise etch rate. The use of μ -APPJ effluent may offer those in industry fast removal of photoresist while being able to preserve the small feature sizes that is demanded of them.

Though this study has revealed promising results, further investigation would be required to progress its readiness as an industrial tool. Substrate damage or roughening from other possible processes would need to be assessed, as well as efficacy at penetrating into very small features to remove all processed photoresist. Furthermore, the engineering challenge exists of treating a full wafer with one or more jets with a treatment diameter of $\sim 10 \text{ mm}$.

Chapter 7

Conclusions

The focus of this study has been to characterise previously unmeasured effluent chemistry of the μ -APPJ together with the underlying plasma dynamics that regulate the plasma chemistry through the use of optical and electrical diagnostics.

The use of picosecond TALIF has allowed for measurement of reactive atomic species in the open air effluent of the μ -APPJ for the first time. The absolute measurement of atomic nitrogen shows production responds in a similar manner to other atomic species, increasing with voltage, with greatest effluent densities found nearest to the jet exit. There is a peak in N production with N₂ admixture at $\sim 0.3\%$. At 13.56 MHz the maximum achievable N density was $(10.6 \pm 1.3) \times 10^{20} \text{ m}^{-3}$. The distribution and density of atomic nitrogen in the effluent is dictated mostly by fluid effects rather than through simple recombination.

The production of secondary reactive nitrogen species like NO correlates highly to atomic nitrogen production. This has implications for complex chemical environments such as biological media where many secondary and tertiary products are a direct result of plasma produced primary reactive species. Researchers now can draw firmer conclusions on the formation of some atomic nitrogen based chemistry.

Modification of driving frequency demonstrates how reactive species such as N and O can be generated in greater quantities using higher frequencies, something that had not been shown in the μ -APPJ in the past. For atomic nitrogen, the density could be increased seven fold using 40.68 MHz, whereas for atomic oxygen it is closer to three fold. This gives another dimension with which operators of the μ -APPJ and future devices can manage reactive species densities. This comes with the trade-off that higher frequencies result in greater gas temperatures, a side effect of greater power dissipation, restricting this capability to non-temperature sensitive applications.

By assessing and minimising the possible error that can arise through different methods of measuring plasma power, it has been feasible to measure plasma power in small radio frequency atmospheric-pressure plasma devices, without the requirement to make assumptions about the phase angle nor measure pre-matching and make assumptions over network

losses. Systematic errors from losses via the matching network are negated by measuring post-matching, and the ensuing error from measuring phase angle at near -90° is suppressed through use of the subtractive method. Small considerations in the method such as maximising sample rate and using sample averaging to minimise uncorrelated noise help to further reduce errors by a potential order of magnitude. As measuring plasma power in the μ -APPJ can be so technically demanding a shared method to estimate plasma power, such as that outlined in this study, can standardise comparisons between institutions, but also act as a foundation for improved methodologies, a key tenet of the EU COST reference jet.

This methodology not only lends confidence in the measured values of plasma power but also provides insight into changes in the plasma dynamics by examining the phase angle of the electrical system. Normally, with the assumptions that have to be made, this information becomes distorted and is therefore discarded. Using the procedures outlined in this research, the extra information gained has shown that the sheath is shrinking with greater plasma power via change in the reactive component, as well as an increase in plasma resistance. PROES confirms the sheath shrinking with greater plasma power. Without this resolution of phase, it would be impossible to distinguish between the plasma becoming more resistive or if the reactive components are changing, through electrical measurement alone. Modelling suggests that the observed sheath constriction is a consequence of higher electron densities, which is correlated to greater power dissipation. Firstly, the smaller sheath means greater bulk plasma dissipation as there is simply a larger volume of bulk available for heating, but secondly the increased electric fields in the smaller sheath leads to greater ion heating in the sheath, further increasing power deposition in the plasma.

Resolution of phase in plasma power measurements has provided evidence for the conjectured hybrid-mode in the μ -APPJ, which was later confirmed with the use of phase resolved optical emission spectroscopy. The PROES measurements display heating in the plasma originating from both the bulk and sheath at high plasma power, rather than exclusively in the α -mode and γ -mode respectively.

At higher frequencies, using helium only in the μ -APPJ, an exclusively γ -mode regime can be achieved. This operating regime is identified as a decrease in operating voltage while plasma power continues to increase. The signifier at which the transition occurs from α -mode, or hybrid-mode, to the γ -mode is this turning point in the voltage. From measurements of phase angle this is seen as a rapid increase in resistance, and a rapid decrease in the reactive component, indicating constriction of the sheath. PROES measurements confirm not only constriction of the sheath during this regime change, but also that emission is dominated by excitation inside the sheath, with comparatively little emission originating from the bulk, which describes γ -mode operation. Previously, this type of operating mode was typically limited to DBD type discharges, however it has been shown that it is possible with a capacitively coupled bare electrode discharge at atmospheric-pressure.

Measurement of plasma power implies that an increase in measured N and O density for higher frequency is in fact a result of greater electron densities in the plasma. This is the case for all frequencies that greater input power results in greater atomic species densities. Atomic nitrogen production can be increased around seven fold at 40.68 MHz, and atomic oxygen production is roughly tripled. Higher frequencies are capable of coupling more power into the plasma, producing more electrons that are available for impact dissociation, therefore producing more of the observed reactive chemistry. Electrical characterisation was once again confirmed using PROES, which both demonstrate further sheath constriction, indicating higher electron densities than 13.56 MHz.

Increase in frequency however does not result in more efficient production of plasma chemistry, with the most energy efficient production found at ~ 2.5 W using 27.12 MHz in this investigation. This has ramifications for the utilisation of the μ -APPJ in applications where efficiency versus absolute reactive species is an issue. Some bespoke treatments such as biomedical treatment rely heavily on the overall dose of reactive species, where the incorrect density of species can cause greatly undesirable consequences such as the proliferation of cancer cells. Larger scale treatments such as those in industry may benefit from more energy efficient production at the cost of longer treatment times, though as time is money and so is energy, it would require a case by case assessment.

The μ -APPJ is not only of use for characterisation, but also application. It can successfully remove photoresist on the order of $\mu\text{m}/\text{min}$. This is orders of magnitude faster than equivalent downstream low-pressure systems. At these fast etching rates, surface damage by ion bombardment is still mitigated as the effluent of the μ -APPJ does not contain an active plasma, which could form a sheath at the substrate surface, accelerating ions into the substrate and for example causing sputtering or implantation.

Using the knowledge and understanding gained by measuring the plasma dynamics and the plasma chemistry in this investigation, it has been possible to confidently assume that etching of photoresist is controlled by atomic oxygen flux to the substrate. The observed etch rate with various operating parameters correlates highly to atomic oxygen flux to the surface. Moreover, other species such as ozone or singlet delta oxygen can be ruled out, as they do not completely share this correlation. Atomic oxygen density at low-pressure compared to atmospheric-pressure explains the orders of magnitude difference in etch rates. At atmospheric-pressure, the μ -APPJ is capable of producing three orders of magnitude greater densities of atomic oxygen. This result has ramifications for industrial and research settings, where rapid atmospheric removal of photoresist is desired without ion bombardment, where previous atmospheric-pressure ashing devices have relied heavily on ion bombardment to achieve fast etch rates.

Characterisation of atomic oxygen has allowed for deeper understanding of this common industrial process, likewise measurement of atomic nitrogen clearly shows how researchers

can link reactive species to other important subsequent species and chemistries. In both these situations, tailoring of fundamental reactive species grants the ability to control the eventual process, be it biomedical or industrial.

This study has not only characterised the μ -APPJ, but also proposed operations of best practice. These best practices are of great importance to future devices such as the EU COST reference jet, as well as other researchers using the μ -APPJ, as they allow a standard framework to emerge as to effectively describe and compare behaviour between institutions. For applications and comparisons when using nitrogen admixtures in the μ -APPJ and future devices based on the same geometry, between 0.3 % to 0.4 % is the optimum for producing atomic nitrogen. When operating the μ -APPJ, the plasma power is an important parameter to record, as cues such as ignition or arcing point do not necessarily indicate the same plasma power across different parameters like molecular admixture admixture. A common practice with small atmospheric-pressure plasmas is to operate at just past the ignition point, or just before arcing as some form of repeatable point, however this study has clearly shown that is not always correct course of action to maintain repeatability across operating parameters.

If assessment of plasma power is not experimentally possible, applied voltage is useful to record, as in some cases it can be a good proxy for plasma power, or it allows reference to known plasma power measurements for given parameter set *a posteriori*. When possible, measurement of plasma power should be performed post matching, as power dissipation from the generator is much greater than the true plasma power, and it should utilise a subtractive method. Measurement using standard RF power meters designed for 50 Ω either pre or post-matching are not suitable. Strays and parasitics in the device are large enough that measuring the power when the plasma is struck and assuming that no power is dissipated when there is no plasma can result in significant underestimation or overestimation of plasma power depending on technique. The subtractive method means that parasitic losses are accounted for, but has the additional benefit that it is more robust to systematic errors in phase.

In conclusion, this work has informed the operation and optimisation of the μ -APPJ for use across different operating parameters for a variety of applications, by monitoring the plasma dynamics and plasma chemistry using novel techniques, for previously unmeasurable scenarios. The results presented are of particular importance to those investigating dual frequency and tailored waveforms in the μ -APPJ. There now exists a benchmark for which experiments and models can compare for both plasma power and plasma chemistry using sole RF driving voltages at 13.56 MHz, 27.12 MHz, and 40.68 MHz.

With regard to future work, it would be of interest to examine electron density and temperature using alternative diagnostics and modelling to understand the plasma dynamics across frequencies in more detail. Understanding the change in electron temperature and density may give insight as to why a 27.12 MHz driving frequency appears to give the best energy efficiency for the operating parameters in this study. This would need to be achieved through passive optical diagnostics such as actinometry or active laser diagnostics such as Thomson scattering, due to the restricted size of the plasma core.

It would also be of great benefit to measure the gas temperature of the effluent more reliably across the frequency range to equate how much coupled plasma power is lost to thermal heating. Simple thermocouples can act as an antenna to RF signals, and misreport induced voltage as extra heating. Careful experimental design would be required as to accurately measure the effluent temperature without inducing spurious results from stray RF fields. Considering temperature is a limitation for some applications, gas temperature as well as substrate temperature is of vital importance when considering dual or multi frequency mixing. This could be achieved many ways, for example the application of thermosensitive stickers, or infrared thermometer measurements, though the latter is fraught with possible errors. The challenge of measuring substrate temperature becomes even more challenging when considering biological media or liquids, which due to their size may have temperature gradients which aid in reactive species transport.

Finally, 2D or 3D fluid modelling of reactive nitrogen species (along with other reactive species) in the μ -APPJ effluent would be of great benefit to understand the intricacies of both fluid effects in the effluent, and chemical effects such as recombination. Modelling would better enable researchers to study the interaction between the effluent region and a target substrate. This has been performed to some extent with oxygen species, but has unfortunately been neglected for nitrogen species.

List of References

- [1] M. A. Lieberman and A. J. Lichtenberg. *Principles of Plasma Discharges and Materials Processing*. Wiley-Interscience, 2nd edition, 2005.
- [2] N. Knake, K. Niemi, S. Reuter, V. Schulz-von der Gathen, and J. Winter. Absolute atomic oxygen density profiles in the discharge core of a microscale atmospheric pressure plasma jet. *Applied Physics Letters*, 93(13):131503, 2008.
- [3] N. Knake, S. Reuter, K. Niemi, V. Schulz-Von Der Gathen, and J. Winter. Absolute atomic oxygen density distributions in the effluent of a microscale atmospheric pressure plasma jet. *Journal of Physics D: Applied Physics*, 41(19):194006, 2008.
- [4] C. Douat, S. Hübner, R. Engeln, and J. Benedikt. Production of nitric/nitrous oxide by an atmospheric pressure plasma jet. *Plasma Sources Science and Technology*, 25(2):025027, 2016.
- [5] P. J. Bruggeman, et al. Plasma–liquid interactions: a review and roadmap. *Plasma Sources Science and Technology*, 25(5):053002, 2016.
- [6] D. B. Graves. The emerging role of reactive oxygen and nitrogen species in redox biology and some implications for plasma applications to medicine and biology. *Journal of Physics D: Applied Physics*, 45(26):263001, 2012.
- [7] J. Winter, R. Brandenburg, and K.-D. Weltmann. Atmospheric pressure plasma jets: an overview of devices and new directions. *Plasma Sources Science and Technology*, 24(6):064001, 2015.
- [8] A. M. Hirst, F. M. Frame, N. J. Maitland, and D. O’Connell. Low temperature plasma: A novel focal therapy for localized prostate cancer? *BioMed Research International*, 2014:1, 2014.
- [9] S. Hübner, J. S. Sousa, V. Puech, G. M. W. Kroesen, and N. Sadeghi. Electron properties in an atmospheric helium plasma jet determined by thomson scattering. *Journal of Physics D: Applied Physics*, 47(43):432001, 2014.

- [10] P.-A. Delattre, T. Lafleur, E. Johnson, and J.-P. Booth. Radio-frequency capacitively coupled plasmas excited by tailored voltage waveforms: comparison of experiment and particle-in-cell simulations. *Journal of Physics D: Applied Physics*, 46(23):235201, 2013.
- [11] D. Marinov and N. S. J. Braithwaite. Power coupling and electrical characterization of a radio-frequency micro atmospheric pressure plasma jet. *Plasma Sources Science and Technology*, 23(6):062005, 2014.
- [12] J. Golda, et al. Concepts and characteristics of the ‘cost reference microplasma jet’. *Journal of Physics D: Applied Physics*, 49(8):084003, 2016.
- [13] R. Dendy. *Plasma Dynamics*. Oxford science publications. Clarendon Press, 1990.
- [14] M. Kivelson and C. Russell. *Introduction to Space Physics*. Cambridge atmospheric and space science series. Cambridge University Press, 1995.
- [15] A. Salabaş and R. P. Brinkmann. Non-neutral/quasi-neutral plasma edge definition for discharge models: A numerical example for dual frequency hydrogen capacitively coupled plasmas. *Japanese Journal of Applied Physics*, 45(6A):5203, 2006.
- [16] P. Chabert and N. Braithwaite. *Physics of radio-frequency plasmas*. Cambridge University Press, 2011.
- [17] A. Betts and S. Hartley. *Advance: The Full Licence Manual*. Radio Society of Great Britain, 3rd edition, 2012.
- [18] A. Schutze, J. Y. Jeong, S. E. Babayan, J. Park, G. S. Selwyn, and R. F. Hicks. The atmospheric-pressure plasma jet: a review and comparison to other plasma sources. *IEEE Transactions on Plasma Science*, 26(6):1685, 1998.
- [19] M. Boulos. Thermal plasma processing. *IEEE Transactions on Plasma Science*, 19(6):1078, 1991.
- [20] J. R. Roth. *Industrial Plasma Engineering: applications to nonthermal plasma processing*, volume 2. CRC Press, 2002.
- [21] B. N. Chapman. *Glow discharge processes: sputtering and plasma etching*. Wiley New York, 1980.
- [22] J. W. Coburn and H. F. Winters. Ion- and electron-assisted gas-surface chemistry-an important effect in plasma etching. *Journal of Applied Physics*, 50(5):3189, 1979.
- [23] K. Davies. *Ionospheric Radio*. Electromagnetics and Radar Series. Peregrinus, 1990.

- [24] A. Gibson and J. Team. Deuterium-tritium plasmas in the Joint European Torus (JET): Behavior and implications. *Physics Of Plasmas*, 5(5):1839, 1998.
- [25] M. A. Sobolewski. Electrical characterization of radio-frequency discharges in the gaseous electronics conference reference cell. *Journal Of Vacuum Science & Technology A*, 10(6):3550, 1992.
- [26] Y. P. Raizer. *Gas Discharge Physics*. Springer, 1997.
- [27] G. Selwyn. Atmospheric-pressure plasma jet, 1999. US Patent 5,961,772.
- [28] J. Jeong, S. Babayan, V. Tu, J. Park, I. Henins, R. Hicks, and G. Selwyn. Etching materials with an atmospheric-pressure plasma jet. *Plasma Sources Science and Technology*, 7(3):282, 1998.
- [29] C. H. Yi, T. W. Kim, K.-H. Kim, W. S. Kang, J. H. Kim, and S. K. Hong. Atmospheric pressure plasma ashing for display manufacturing. *Japanese Journal Of Applied Physics*, 47(8):6965, 2008.
- [30] S. Babayan, G. Ding, and R. Hicks. Determination of the nitrogen atom density in the afterglow of a nitrogen and helium, nonequilibrium, atmospheric pressure plasma. *Plasma Chemistry and Plasma Processing*, 21(4):505, 2001.
- [31] R. A. Wolf. *Atmospheric Pressure Plasma for Surface Modification*. Wiley, 2012.
- [32] M. Thomas and K. Mittal. *Atmospheric Pressure Plasma Treatment of Polymers: Relevance to Adhesion*. Adhesion and Adhesives: Fundamental and Applied Aspects. Wiley, 2013.
- [33] S. E. Babayan, J. Y. Jeong, V. J. Tu, J. Park, G. S. Selwyn, and R. F. Hicks. Deposition of silicon dioxide films with an atmospheric-pressure plasma jet. *Plasma Sources Science and Technology*, 7(3):286, 1998.
- [34] J. Benedikt, V. Raballand, A. Yanguas-Gil, K. Focke, and A. von Keudell. Thin film deposition by means of atmospheric pressure microplasma jet. *Plasma Physics and Controlled Fusion*, 49(12B):B419, 2007.
- [35] L. Haijiang, W. Shouguo, Z. Lingli, and Y. Tianchun. Study on an atmospheric pressure plasma jet and its application in etching photo-resistant materials. *Plasma Science and Technology*, 6(5):2481, 2004.
- [36] K. Fricke, I. Koban, H. Tresp, L. Jablonowski, K. Schröder, A. Kramer, K.-D. Weltmann, T. von Woedtke, and T. Kocher. Atmospheric pressure plasma: A high-performance tool for the efficient removal of biofilms. *PLoS ONE*, 7(8):e42539, 2012.

- [37] A. R. Gibson, H. O. McCarthy, A. A. Ali, D. O'Connell, and W. G. Graham. Interactions of a non-thermal atmospheric pressure plasma effluent with PC-3 prostate cancer cells. *Plasma Processes and Polymers*, 11(12):1142, 2014.
- [38] D. O'Connell, L. J. Cox, W. B. Hyland, S. J. McMahon, S. Reuter, W. G. Graham, T. Gans, and F. J. Currell. Cold atmospheric pressure plasma jet interactions with plasmid DNA. *Applied Physics Letters*, 98(4):043701, 2011.
- [39] B. Haertel, T. v. Woedtke, K.-D. Weltmann, and U. Lindequist. Non-thermal atmospheric-pressure plasma possible application in wound healing. *Biomolecules & Therapeutics*, 22(6):477, 2014.
- [40] S. Bekeschus, A. Schmidt, K.-D. Weltmann, and T. von Woedtke. The plasma jet kinpen - a powerful tool for wound healing. *Clinical Plasma Medicine*, 2016.
- [41] V. Schulz-von der Gathen, L. Schaper, N. Knake, S. Reuter, K. Niemi, T. Gans, and J. Winter. Spatially resolved diagnostics on a microscale atmospheric pressure plasma jet. *Journal of Physics D: Applied Physics*, 41(19):194004, 2008.
- [42] V. Schulz-von der Gathen, V. Buck, T. Gans, N. Knake, K. Niemi, S. Reuter, L. Schaper, and J. Winter. Optical diagnostics of micro discharge jets. *Contributions to Plasma Physics*, 47(7):510, 2007.
- [43] J. Waskoenig. *Numerical simulations of the electron dynamics in single and dual radio-frequency driven atmospheric pressure plasmas and associated plasma chemistry in electro-negative He-O₂ mixtures*. Ph.D. thesis, Queen's University Belfast, 2011.
- [44] A. M. Hirst, M. S. Simms, V. M. Mann, N. J. Maitland, D. O'Connell, and F. M. Frame. Low-temperature plasma treatment induces DNA damage leading to necrotic cell death in primary prostate epithelial cells. *British Journal of Cancer*, 112(9):1536, 2015.
- [45] S. Schneider, J.-W. Lackmann, F. Narberhaus, J. E. Bandow, B. Denis, and J. Benedikt. Separation of VUV/UV photons and reactive particles in the effluent of a He/O₂ atmospheric pressure plasma jet. *Journal of Physics D: Applied Physics*, 44(29):295201, 2011.
- [46] S. Reuter, K. Niemi, V. Schulz-von der Gathen, and H. F. Döbele. Generation of atomic oxygen in the effluent of an atmospheric pressure plasma jet. *Plasma Sources Science and Technology*, 18(1):015006, 2008.
- [47] D. Schröder, H. Bahre, N. Knake, J. Winter, T. de los Arcos, and V. Schulz-von der Gathen. Influence of target surfaces on the atomic oxygen distribution in the efflu-

- ent of a micro-scaled atmospheric pressure plasma jet. *Plasma Sources Science and Technology*, 21(2):024007, 2012.
- [48] D. Ellerweg, A. von Keudell, and J. Benedikt. Unexpected O and O₃ production in the effluent of He/O₂ microplasma jets emanating into ambient air. *Plasma Sources Science and Technology*, 21(3):034019, 2012.
- [49] A. West, M. van der Schans, C. Xu, M. Cooke, and E. Wagenaars. Fast, downstream removal of photoresist using reactive oxygen species from the effluent of an atmospheric pressure plasma jet. *Plasma Sources Science and Technology*, 25(2):02LT01, 2016.
- [50] International Telecommunications Union. *Radio Regulations*, volume 1. ITU Publications, 2012.
- [51] W. A. Davis and K. Agarwal. *Radio frequency circuit design*, volume 162 of *Wiley Series in Microwave and Optical Engineering*. Wiley, 2003.
- [52] S. C. Brown. *Basic Data of Plasma Physics*. M.I.T Press, 1959.
- [53] P. J. Hargis, et al. The gaseous electronics conference radio-frequency reference cell: A defined parallel-plate radio-frequency system for experimental and theoretical studies of plasma-processing discharges. *Review of Scientific Instruments*, 65(1):140, 1994.
- [54] S. Kelly, J. Golda, M. M. Turner, and V. Schulz-von der Gathen. Gas and heat dynamics of a micro-scaled atmospheric pressure plasma reference jet. *Journal of Physics D: Applied Physics*, 48(44):444002, 2015.
- [55] S. Schneider, F. Jarzina, J.-W. Lackmann, J. Golda, V. Layes, V. Schulz-von der Gathen, J. E. Bandow, and J. Benedikt. Summarizing results on the performance of a selective set of atmospheric plasma jets for separation of photons and reactive particles. *Journal of Physics D: Applied Physics*, 48(44):444001, 2015.
- [56] P. A. C. Beijer, A. Sobota, E. M. van Veldhuizen, and G. M. W. Kroesen. Multiplying probe for accurate power measurements on an RF driven atmospheric pressure plasma jet applied to the cost reference microplasma jet. *Journal of Physics D: Applied Physics*, 49(10):104001, 2016.
- [57] T. Murakami, K. Niemi, T. Gans, D. O'Connell, and W. G. Graham. Afterglow chemistry of atmospheric-pressure helium-oxygen plasmas with humid air impurity. *Plasma Sources Science and Technology*, 23(2):025005, 2014.
- [58] K. Niemi, D. O'Connell, N. de Oliveira, D. Joyeux, L. Nahon, J. P. Booth, and T. Gans. Absolute atomic oxygen and nitrogen densities in radio-frequency driven atmospheric pressure cold plasmas: Synchrotron vacuum ultra-violet high-resolution

- Fourier-transform absorption measurements. *Applied Physics Letters*, 103(3):034102, 2013.
- [59] K. Niemi, V. Schulz-Von Der Gathen, and H. Döbele. Absolute atomic oxygen density measurements by two-photon absorption laser-induced fluorescence spectroscopy in an RF-excited atmospheric pressure plasma jet. *Plasma Sources Science and Technology*, 14(2):375, 2005.
- [60] J. Waskoenig, K. Niemi, N. Knake, L. Graham, S. Reuter, V. Schulz-von der Gathen, and T. Gans. Atomic oxygen formation in a radio-frequency driven micro-atmospheric pressure plasma jet. *Plasma Sources Science and Technology*, 19(4):045018, 2010.
- [61] A. Greb, K. Niemi, D. O’Connell, and T. Gans. Energy resolved actinometry for simultaneous measurement of atomic oxygen densities and local mean electron energies in radio-frequency driven plasmas. *Applied Physics Letters*, 105(23):234105, 2014.
- [62] J. Sousa, K. Niemi, L. Cox, Q. T. Algwari, T. Gans, and D. O’Connell. Cold atmospheric pressure plasma jets as sources of singlet delta oxygen for biomedical applications. *Journal of Applied Physics*, 109(12):123302, 2011.
- [63] T. Murakami, K. Niemi, T. Gans, D. O’Connell, and W. G. Graham. Chemical kinetics and reactive species in atmospheric pressure helium-oxygen plasmas with humid-air impurities. *Plasma Sources Science and Technology*, 22(1):015003, 2013.
- [64] T. Murakami, K. Niemi, T. Gans, D. O’Connell, and W. G. Graham. Interacting kinetics of neutral and ionic species in an atmospheric-pressure helium-oxygen plasma with humid air impurities. *Plasma Sources Science and Technology*, 22(4):045010, 2013.
- [65] K. Niemi, T. Gans, and D. O’Connell. Comparison of a global model to semi-kinetic fluid simulations for atmospheric pressure radio-frequency plasmas. *Plasma Sources Science and Technology*, 22(3):032001, 2013.
- [66] S. Kelly and M. M. Turner. Generation of reactive species by an atmospheric pressure plasma jet. *Plasma Sources Science and Technology*, 23(6):065013, 2014.
- [67] E. Wagenaars, T. Gans, D. O’Connell, and K. Niemi. Two-photon absorption laser-induced fluorescence measurements of atomic nitrogen in a radio-frequency atmospheric-pressure plasma jet. *Plasma Sources Science and Technology*, 21(4):042002, 2012.
- [68] S. Schneider, M. Dünnebier, S. Hübner, S. Reuter, and J. Benedikt. Atomic nitrogen: a parameter study of a micro-scale atmospheric pressure plasma jet by means of molec-

- ular beam mass spectrometry. *Journal of Physics D: Applied Physics*, 47(50):505203, 2014.
- [69] S. Guimond and M. R. Wertheimer. Surface degradation and hydrophobic recovery of polyolefins treated by air corona and nitrogen atmospheric pressure glow discharge. *Journal of applied polymer science*, 94(3):1291, 2004.
- [70] S. Mazouffre, I. Bakker, P. Vankan, R. Engeln, and D. C. Schram. Two-photon laser induced fluorescence spectroscopy performed on free nitrogen plasma jets. *Plasma Sources Science and Technology*, 11(4):439, 2002.
- [71] M. Sato. Plasma-assisted mpcvd growth of GaAs/GaN/GaAs thin-layer structures by N-As replacement using N-radicals. *Japanese Journal of Applied Physics*, 34(Part 1, No. 2B):1080, 1995.
- [72] S. Nakamura, T. Mukai, and M. Senoh. High-brightness InGaN/AlGaN double-heterostructure blue-green-light-emitting diodes. *Journal of Applied Physics*, 76(12):8189, 1994.
- [73] F. A. Ponce and D. P. Bour. Nitride-based semiconductors for blue and green light-emitting devices. *Nature*, 386(6623):351, 1997.
- [74] M. G. Kong, G. Kroesen, G. Morfill, T. Nosenko, T. Shimizu, J. van Dijk, and J. L. Zimmermann. Plasma medicine: an introductory review. *New Journal of Physics*, 11(11):115012, 2009.
- [75] P. Pacher, J. S. Beckman, and L. Liaudet. Nitric oxide and peroxynitrite in health and disease. *Physiological reviews*, 87(1):315, 2007.
- [76] D. D. Thomas, et al. The chemical biology of nitric oxide: implications in cellular signaling. *Free Radical Biology and Medicine*, 45(1):18, 2008.
- [77] M. B. Witte and A. Barbul. Role of nitric oxide in wound repair. *The American Journal of Surgery*, 183(4):406, 2002.
- [78] C. C. Miller, M. K. Miller, A. Ghaffari, and B. Kunimoto. Treatment of chronic nonhealing leg ulceration with gaseous nitric oxide: A case study. *Journal of Cutaneous Medicine and Surgery*, 8(4):233, 2004.
- [79] A. F. Chen and J. Luo. Nitric oxide: a newly discovered function on wound healing. *Acta Pharmacologica Sinica*, 26(3):259, 2005.
- [80] D. Hirst and T. Robson. Targeting nitric oxide for cancer therapy. *Journal of Pharmacy and Pharmacology*, 59(1):3, 2007.

- [81] Q. Xiong, A. Y. Nikiforov, L. Li, P. Vanraes, N. Britun, R. Snyders, X. P. Lu, and C. Leys. Absolute OH density determination by laser induced fluorescence spectroscopy in an atmospheric pressure RF plasma jet. *European Physical Journal D: Atomic, Molecular and Optical Physics*, 66(11), 2012.
- [82] T. Verreycken, R. Mensink, R. v. d. Horst, N. Sadeghi, and P. J. Bruggeman. Absolute OH density measurements in the effluent of a cold atmospheric-pressure Ar-H₂O RF plasma jet in air. *Plasma Sources Science and Technology*, 22(5):055014, 2013.
- [83] D. Riès, G. Dilecce, E. Robert, P. F. Ambrico, S. Dozias, and J.-M. Pouvesle. LIF and fast imaging plasma jet characterization relevant for NTP biomedical applications. *Journal of Physics D: Applied Physics*, 47(27):275401, 2014.
- [84] A. F. H. van Gessel, B. Hrycak, M. Jasiński, J. Mizeraczyk, J. J. A. M. van der Mullen, and P. J. Bruggeman. Temperature and NO density measurements by LIF and OES on an atmospheric pressure plasma jet. *Journal of Physics D: Applied Physics*, 46(9):095201, 2013.
- [85] K. Ono. Measurements of the Cl atom concentration in radio-frequency and microwave plasmas by two-photon laser-induced fluorescence: Relation to the etching of Si. *Journal Of Vacuum Science & Technology A*, 10(4):1071, 1992.
- [86] J. P. Booth, Y. Azamoum, N. Sirse, and P. Chabert. Absolute atomic chlorine densities in a Cl₂ inductively coupled plasma determined by two-photon laser-induced fluorescence with a new calibration method. *Journal of Physics D: Applied Physics*, 45(19):195201, 2012.
- [87] A. Francis. *Spektroskopische Untersuchungen zur Struktur und Dynamik der Radikale in einer reaktiven Flour-Kohlenstoff-Entladung*. Ph.D. thesis, Universität Duisburg-Essen, 2003.
- [88] K. Niemi, V. Schulz-Von Der Gathen, and H. Döbele. Absolute calibration of atomic density measurements by laser-induced fluorescence spectroscopy with two-photon excitation. *Journal of Physics D: Applied Physics*, 34(15):2330, 2001.
- [89] S. Mazouffre, C. Foissac, P. Supiot, P. Vankan, R. Engeln, D. Schram, and N. Sadeghi. Density and temperature of N atoms in the afterglow of a microwave discharge measured by a two-photon laser-induced fluorescence technique. *Plasma Sources Science and Technology*, 10(2):168, 2001.
- [90] E. Es-sebbar, Y. Benilan, A. Jolly, and M.-C. Gazeau. Characterization of an N₂ flowing microwave post-discharge by OES spectroscopy and determination of absolute

- ground-state nitrogen atom densities by TALIF. *Journal of Physics D: Applied Physics*, 42(13):135206, 2009.
- [91] W. K. Bischel, B. E. Perry, and D. R. Crosley. Two-photon laser-induced fluorescence in oxygen and nitrogen atoms. *Chemical Physics Letters*, 82(1):85, 1981.
- [92] W. Demtröder. *Laser spectroscopy. Vol. 1, Basic principles*. Springer, 2008.
- [93] R. Loudon. *The quantum theory of light*. Oxford university press, 3rd edition, 2000.
- [94] M. Payne, C. Chen, G. Hurst, and G. Foltz. Applications of resonance ionization spectroscopy in atomic and molecular physics. *Advances in atomic and molecular physics*, 17:229, 1981.
- [95] A. Goehlich, T. Kawetzki, and H. Döbele. On absolute calibration with xenon of laser diagnostic methods based on two-photon absorption. *The Journal of chemical physics*, 108(22):9362, 1998.
- [96] S. F. Adams and T. A. Miller. Two-photon absorption laser-induced fluorescence of atomic nitrogen by an alternative excitation scheme. *Chemical physics letters*, 295(4):305, 1998.
- [97] R. S. F. Chang, H. Horiguchi, and D. W. Setser. Radiative lifetimes and two-body collisional deactivation rate constants in argon for $\text{kr}(4p^5 5p)$ and $\text{kr}(4p^5 5p')$ states. *Journal of Chemical Physics*, 73(2):778, 1980.
- [98] H. Horiguchi, R. S. F. Chang, and D. W. Setser. Radiative lifetimes and two-body collisional deactivation rate constants in Ar for $\text{Xe}(5p^5 6p)$, $\text{Xe}(5p^5 6p')$, and $\text{Xe}(5p^5 7p)$ states. *Journal of Chemical Physics*, 75(3):1207, 1981.
- [99] A. Kramida, Y. Ralchenko, J. Reader, and N. A. Team. *NIST Atomic Spectra Database*. National Institute of Standards and Technology, 5th edition, 2015. Available: <http://physics.nist.gov/asd>.
- [100] G. J. Bengtsson, J. Larsson, S. Svanberg, and D. D. Wang. Natural lifetimes of excited states of neutral nitrogen determined by time-resolved laser spectroscopy. *Physical Review A*, 45(5):2712, 1992.
- [101] D. W. Setser. *Reactive intermediates in the gas phase: generation and monitoring*. New York: Academic Press, 1979.
- [102] K. Niemi, T. Mosbach, and H. Döbele. Is the flow tube reactor with NO_2 titration a reliable absolute source for atomic hydrogen? *Chemical physics letters*, 367(5):549, 2003.

- [103] H. F. Döbele, T. Mosbach, K. Niemi, , and V. Schulz-von der Gathen. Laser-induced fluorescence measurements of absolute atomic densities: concepts and limitations. *Plasma Sources Science and Technology*, 14(2):S31, 2005.
- [104] E. Es-sebbar, M. C-Gazeau, Y. Benilan, A. Jolly, and C. D. Pintassilgo. Absolute ground-state nitrogen atom density in a N_2/CH_4 late afterglow: TALIF experiments and modelling studies. *Journal of Physics D: Applied Physics*, 43(33):335203, 2010.
- [105] J. B. Schmidt, B. L. Sands, W. D. Kulatilaka, S. Roy, J. Scofield, and J. R. Gord. Femtosecond, two-photon laser-induced-fluorescence imaging of atomic oxygen in an atmospheric-pressure plasma jet. *Plasma Sources Science and Technology*, 24(3):032004, 2015.
- [106] F. Gaboriau, U. Cvelbar, M. Mozetic, A. Erradi, and B. Rouffet. Comparison of TALIF and catalytic probes for the determination of nitrogen atom density in a nitrogen plasma afterglow. *Journal of Physics D: Applied Physics*, 42(5):055204, 2009.
- [107] A. Hibbert, E. Biemont, M. Godefroid, and N. Vaeck. New accurate transition probabilities for astrophysically important spectral lines of neutral nitrogen. *Astronomy & Astrophysics Supplement Series*, 88:505, 1991.
- [108] V. Alekseev and D. W. Setser. Quenching rate constants and product assignments for reactions of $Xe(7p[3/2]_2, 7p[5/2]_2, \text{ and } 6p[3/2]_2)$ atoms with rare gases, CO , H_2 , N_2O , CH_4 , and halogen-containing molecules. *Journal of Physical Chemistry*, 100(14):5766, 1996.
- [109] M. G. H. Boogaarts, S. Mazouffre, G. J. Brinkman, H. W. P. van der Heijden, P. Vankan, J. A. M. van der Mullen, D. C. Schram, and H. F. Döbele. Quantitative two-photon laser-induced fluorescence measurements of atomic hydrogen densities, temperatures, and velocities in an expanding thermal plasma. *Review of Scientific Instruments*, 73(1):73, 2002.
- [110] V. A. Alekseev and D. W. Setser. A pulsed source for $Xe(6s[3/2]_1)$ and $Xe(6s'[1/2]_1)$ resonance state atoms using two-photon driven amplified spontaneous emission from the $Xe(6p)$ and $Xe(6p')$ states. *Journal Of Chemical Physics*, 105(11):4613, 1996.
- [111] V. A. Alekseev and D. W. Setser. A pulsed source for $Kr(5s[3/2]_2)$ resonance state atoms using two-photon-driven amplified spontaneous emission: Measurement of quenching rate constants. *The Journal of Physical Chemistry A*, 103(20):4016, 1999.
- [112] J. Amorim, G. Baravian, and J. Jolly. Laser-induced resonance fluorescence as a diagnostic technique in non-thermal equilibrium plasmas. *Journal of Physics D: Applied Physics*, 33(9):R51, 2000.

- [113] J. C. Miller. Two-photon resonant multiphoton ionization and stimulated emission in krypton and xenon. *Physical Review A*, 40(12):6969, 1989.
- [114] A. Hsu, V. Narayanaswamy, N. Clemens, and J. Frank. Mixture fraction imaging in turbulent non-premixed flames with two-photon LIF of krypton. *Proceedings of the Combustion Institute*, 33(1):759, 2011.
- [115] J. Amorim, G. Baravian, M. Touzeau, and J. Jolly. Two-photon laser induced fluorescence and amplified spontaneous emission atom concentration measurements in O_2 and H_2 discharges. *Journal of Applied Physics*, 76(3):1487, 1994.
- [116] K. Niemi. *Nachweis leichter Atome in reaktiven Plasmen mittels Zweiphotonen laserinduzierter Fluoreszenzspektroskopie unter besonderer Berücksichtigung der Absolutkalibrierung*. Cuvillier Verlag, 2003.
- [117] K. Omidvar. Two-photon excitation cross section in light and intermediate atoms in frozen-core ls-coupling approximation. *Physical Review A*, 22(4):1576, 1980.
- [118] K. Omidvar. Erratum: Two-photon excitation cross section in light and intermediate atoms in frozen-core ls-coupling approximation. *Physical Review A*, 30(5):2805, 1984.
- [119] M. S. Pindzola. Two-photon excitation of atomic oxygen. *Physical Review A*, 17(3):1021, 1978.
- [120] Y. Gontier and M. Trahin. On the multiphoton absorption in atomic hydrogen. *Physics Letters A*, 36(6):463, 1971.
- [121] D. J. Bamford, L. E. Jusinski, and W. K. Bischel. Absolute two-photon absorption and three-photon ionization cross sections for atomic oxygen. *Physical Review A*, 34(1):185, 1986.
- [122] R. Wells. Rapid approximation to the voigt/faddeeva function and its derivatives. *Journal of Quantitative Spectroscopy and Radiative Transfer*, 62(1):29, 1999.
- [123] B. Armstrong. Spectrum line profiles: The voigt function. *Journal of Quantitative Spectroscopy and Radiative Transfer*, 7(1):61, 1967.
- [124] S. Devinderjit. *Data analysis: a Bayesian tutorial*. Oxford University Press, 2006.
- [125] J. Kruschke. *Doing Bayesian data analysis: A tutorial with R, JAGS, and Stan*. Academic Press, 2014.
- [126] H. R. Griem. *Principles of plasma spectroscopy*, volume 2. Cambridge University Press, 2005.

- [127] I. H. Hutchinson. *Principles of Plasma Diagnostics*. Cambridge University Press, 2005.
- [128] A. Fridman. *Plasma Chemistry*. Cambridge University Press, 2008.
- [129] E. Robert, V. Sarron, T. Darny, D. Riès, S. Dozias, J. Fontane, L. Joly, and J.-M. Pouvesle. Rare gas flow structuration in plasma jet experiments. *Plasma Sources Science and Technology*, 23(1):012003, 2014.
- [130] A. R. Gibson, A. Greb, W. G. Graham, and T. Gans. Tailoring the nonlinear frequency coupling between odd harmonics for the optimisation of charged particle dynamics in capacitively coupled oxygen plasmas. *Applied Physics Letters*, 106(5):054102, 2015.
- [131] T. Lafleur, P. Chabert, and J. P. Booth. Electron heating in capacitively coupled plasmas revisited. *Plasma Sources Science and Technology*, 23(3):035010, 2014.
- [132] A. Greb, A. Robert Gibson, K. Niemi, D. O’Connell, and T. Gans. Influence of surface conditions on plasma dynamics and electron heating in a radio-frequency driven capacitively coupled oxygen plasma. *Plasma Sources Science and Technology*, 24(4):044003, 2015.
- [133] T. Hemke, D. Eremin, T. Mussenbrock, A. Derzsi, Z. Donkó, K. Dittmann, J. Meichsner, and J. Schulze. Ionization by bulk heating of electrons in capacitive radio frequency atmospheric pressure microplasmas. *Plasma Sources Science and Technology*, 22(1):015012, 2012.
- [134] W. M. Haynes. *CRC handbook of chemistry and physics*. CRC press, 94th edition, 2013.
- [135] V. A. Godyak. In situ simultaneous radio frequency discharge power measurements. *Journal Of Vacuum Science & Technology A*, 8(5):3833, 1990.
- [136] S. Hofmann, A. Van Gessel, T. Verreycken, and P. Bruggeman. Power dissipation, gas temperatures and electron densities of cold atmospheric pressure helium and argon RF plasma jets. *Plasma Sources Science and Technology*, 20(6):065010, 2011.
- [137] C. M. Horwitz. Radio frequency sputtering - the significance of power input. *Journal Of Vacuum Science & Technology A*, 1(4):1795, 1983.
- [138] V. A. Godyak, R. B. Piejak, and B. M. Alexandrovich. Electrical characteristics of parallel-plate RF discharges in argon. *IEEE Transactions on Plasma Science*, 19(4):660, 1991.
- [139] J. Laimer and H. Störi. Glow discharges observed in capacitive radio-frequency atmospheric-pressure plasma jets. *Plasma Processes and Polymers*, 3(8):573, 2006.

- [140] T. Lafleur, P. Delattre, J. Booth, E. Johnson, and S. Dine. Radio frequency current-voltage probe for impedance and power measurements in multi-frequency unmatched loads. *Review of Scientific Instruments*, 84(1):015001, 2013.
- [141] A. Papoulis and S. U. Pillai. *Probability, random variables, and stochastic processes*. Tata McGraw-Hill Education, 2002.
- [142] B. P. Lathi. *Modern Digital and Analog Communication Systems*. Oxford university press, 3rd edition, 1998.
- [143] W.-C. Zhu, B.-R. Wang, Z.-X. Yao, and Y.-K. Pu. Discharge characteristics of an atmospheric pressure radio-frequency plasma jet. *Journal of Physics D: Applied Physics*, 38(9):1396, 2005.
- [144] S. Wan-Li, W. De-Zhen, and M. G. Kong. Simulation of radio-frequency atmospheric pressure glow discharge in γ mode. *Chinese Physics*, 16(2):485, 2007.
- [145] J. Shi and M. Kong. Mode characteristics of radio-frequency atmospheric glow discharges. *IEEE Transactions on Plasma Science*, 33(2):624, 2005.
- [146] J. J. Shi and M. G. Kong. Mechanisms of the α and γ modes in radio-frequency atmospheric glow discharges. *Journal of Applied Physics*, 97(2):023306, 2005.
- [147] H.-P. Li, W.-T. Sun, H.-B. Wang, G. Li, and C.-Y. Bao. Electrical features of radio-frequency, atmospheric-pressure, bare-metallic-electrode glow discharges. *Plasma Chemistry and Plasma Processing*, 27(5):529, 2007.
- [148] J. Waskoenig and T. Gans. Nonlinear frequency coupling in dual radio-frequency driven atmospheric pressure plasmas. *Applied Physics Letters*, 96(18):181501, 2010.
- [149] K. McKay, F. Iza, and M. G. Kong. Excitation frequency effects on atmospheric-pressure helium RF microplasmas: plasma density, electron energy and plasma impedance. *European Physical Journal D: Atomic, Molecular and Optical Physics*, 60(3):497, 2010.
- [150] E. Kawamura, M. A. Lieberman, A. J. Lichtenberg, P. Chabert, and C. Lazzaroni. Particle-in-cell and global simulations of α to γ transition in atmospheric pressure penning-dominated capacitive discharges. *Plasma Sources Science and Technology*, 23(3):035014, 2014.
- [151] V. J. Law, S. Daniels, J. L. Walsh, M. G. Kong, L. M. Graham, and T. Gans. Non-invasive VHF monitoring of low-temperature atmospheric pressure plasma. *Plasma Sources Science and Technology*, 19(3):034008, 2010.

- [152] J. Park, I. Henins, H. W. Herrmann, and G. S. Selwyn. Gas breakdown in an atmospheric pressure radio-frequency capacitive plasma source. *Journal of Applied Physics*, 89(1):15, 2001.
- [153] V. A. Lisovskii. Features of the $\alpha - \gamma$ transition in a low-pressure RF argon discharge. *Technical Physics*, 43(5):526, 1998.
- [154] D. W. Liu, F. Iza, and M. G. Kong. Electron heating in radio-frequency capacitively coupled atmospheric-pressure plasmas. *Applied Physics Letters*, 93(26):261503, 2008.
- [155] L. Schaper, S. Reuter, J. Waskoenig, K. Niemi, V. S.-v. d. Gathen, and T. Gans. The dynamics of radio-frequency driven atmospheric pressure plasma jets. *Journal of Physics: Conference Series*, 162:012013, 2009.
- [156] L. Schaper, J. Waskoenig, M. G. Kong, V. Schulz-von der Gathen, and T. Gans. Electron dynamics in a radio-frequency-driven microatmospheric pressure plasma jet. *IEEE Transactions on Plasma Science*, 39(11):2370, 2011.
- [157] J. Waskoenig, K. Niemi, N. Knake, L. M. Graham, S. Reuter, V. Schulz-von der Gathen, and T. Gans. Diagnostic-based modeling on a micro-scale atmospheric-pressure plasma jet. *Pure and Applied Chemistry*, 82(6), 2010.
- [158] D. W. Liu, F. Iza, and M. G. Kong. Evolution of atmospheric-pressure RF plasmas as the excitation frequency increases. *Plasma Processes and Polymers*, 6(6-7):446, 2009.
- [159] C. O'Neill, J. Waskoenig, and T. Gans. Electron heating in dual-radio-frequency-driven atmospheric-pressure plasmas. *IEEE Transactions on Plasma Science*, 39(11):2588, 2011.
- [160] J. Laimer, A. Puchhammer, and H. Störi. Plasma sheath dynamics in dielectric barrier-free atmospheric pressure radio-frequency glow discharges. *Plasma Processes and Polymers*, 6(S1):S253, 2009.
- [161] J. Park, I. Henins, H. W. Herrmann, G. S. Selwyn, and R. F. Hicks. Discharge phenomena of an atmospheric pressure radio-frequency capacitive plasma source. *Journal of Applied Physics*, 89(1):20, 2001.
- [162] J. J. Shi, X. T. Deng, R. Hall, J. D. Punnett, and M. G. Kong. Three modes in a radio frequency atmospheric pressure glow discharge. *Journal of Applied Physics*, 94(10):6303, 2003.
- [163] J. J. Shi, D. W. Liu, and M. G. Kong. Mitigating plasma constriction using dielectric barriers in radio-frequency atmospheric pressure glow discharges. *Applied Physics Letters*, 90(3):031505, 2007.

- [164] A. Chirokov, S. N. Khot, S. P. Gangoli, A. Fridman, P. Henderson, A. F. Gutsol, and A. Dolgopolsky. Numerical and experimental investigation of the stability of radio-frequency (RF) discharges at atmospheric pressure. *Plasma Sources Science and Technology*, 18(2):025025, 2009.
- [165] X. Yang, M. Moravej, G. R. Nowling, S. E. Babayan, J. Panelon, J. P. Chang, and R. F. Hicks. Comparison of an atmospheric pressure, radio-frequency discharge operating in the α and γ modes. *Plasma Sources Science and Technology*, 14(2):314, 2005.
- [166] T. Gans, V. Schulz-von der Gathen, and H. Döbele. Prospects of phase resolved optical emission spectroscopy as a powerful diagnostic tool for RF-discharges. *Contributions to Plasma Physics*, 44(56):523, 2004.
- [167] T. Gans, D. O'Connell, V. Schulz-von der Gathen, and J. Waskoenig. The challenge of revealing and tailoring the dynamics of radio-frequency plasmas. *Plasma Sources Science and Technology*, 19(3):034010, 2010.
- [168] J. Schulze, E. Schüngel, Z. Donkó, D. Luggenhölscher, and U. Czarnetzki. Phase resolved optical emission spectroscopy: a non-intrusive diagnostic to study electron dynamics in capacitive radio frequency discharges. *J. Phys. D: Appl. Phys.*, 43(12):124016, 2010.
- [169] J. Schulze, T. Gans, D. O'Connell, U. Czarnetzki, A. R. Ellingboe, and M. M. Turner. Space and phase resolved plasma parameters in an industrial dual-frequency capacitively coupled radio-frequency discharge. *J. Phys. D: Appl. Phys.*, 40(22):7008, 2007.
- [170] A. Perret, P. Chabert, J. Jolly, and J.-P. Booth. Ion energy uniformity in high-frequency capacitive discharges. *Applied Physics Letters*, 86(2):021501, 2005.
- [171] C. O'Neill, J. Waskoenig, and T. Gans. Tailoring electron energy distribution functions through energy confinement in dual radio-frequency driven atmospheric pressure plasmas. *Applied Physics Letters*, 101(15):154107, 2012.
- [172] B. Bruneau, T. Gans, D. O'Connell, A. Greb, E. V. Johnson, and J.-P. Booth. Strong ionization asymmetry in a geometrically symmetric radio frequency capacitively coupled plasma induced by sawtooth voltage waveforms. *Physical Review Letters*, 114(12), 2015.
- [173] T. Lafleur. Tailored-waveform excitation of capacitively coupled plasmas and the electrical asymmetry effect. *Plasma Sources Science and Technology*, 25(1):013001, 2015.
- [174] J. J. Shi and M. G. Kong. Expansion of the plasma stability range in radio-frequency atmospheric-pressure glow discharges. *Applied Physics Letters*, 87(20):201501, 2005.

- [175] Y. P. Raizer, M. N. Shneider, and N. A. Yatsenko. *Radio-frequency capacitive discharges*. CRC Press, 1995.
- [176] W. G. Townsend and G. C. Williams. The electrical breakdown of gases in uniform high frequency fields at low pressure. *Proceedings of the Physical Society*, 72(5):823, 1958.
- [177] V. Lisovski, J.-P. Booth, K. Landry, D. Douai, V. Cassagne, and V. Yegorenkov. Similarity law for RF breakdown. *Europhysics Letters*, 82(1):15001, 2008.
- [178] J. L. Walsh, F. Iza, and M. G. Kong. Atmospheric glow discharges from the high-frequency to very high-frequency bands. *Applied Physics Letters*, 93(25):251502, 2008.
- [179] J. J. Shi, D. W. Liu, and M. G. Kong. Effects of dielectric barriers in radio-frequency atmospheric glow discharges. *IEEE Transactions on Plasma Science*, 35(2):137, 2007.
- [180] Y. T. Zhang and W. Shang. Frequency scaling laws of plasma bulk in atmospheric radio frequency discharges. *Plasma Processes and Polymers*, 9(5):513, 2012.
- [181] C. Beneking. Power dissipation in capacitively coupled rf discharges. *Journal of Applied Physics*, 68(9):4461, 1990.
- [182] D. S. Stafford and M. J. Kushner. $O_2(^1\Delta)$ production in He/ O_2 mixtures in flowing low pressure plasmas. *Journal of Applied Physics*, 96(5):2451, 2004.
- [183] D. M. Manos and D. L. Flamm. *Plasma etching: an introduction*. Academic Press, 1989.
- [184] S. J. Pearton and D. P. Norton. Dry etching of electronic oxides, polymers, and semiconductors. *Plasma Processes and Polymers*, 2(1):16, 2005.
- [185] H. Hughes, W. Hunter, and K. Ritchie. Residues remaining after RF plasma photoresist removal. *J. Electrochem. Soc.*, 120(1):99, 1973.
- [186] C. Kittel. *Introduction to solid state physics*. Wiley, 7th edition, 1996.
- [187] V. M. Donnelly and A. Kornblit. Plasma etching: Yesterday, today, and tomorrow. *Journal Of Vacuum Science & Technology A*, 31(5):050825, 2013.
- [188] B. Thedjoisworo, D. Cheung, and V. Crist. Comparison of the effects of downstream H_2 - and O_2 -based plasmas on the removal of photoresist, silicon, and silicon nitride. *Journal Of Vacuum Science & Technology B*, 31(2):021206, 2013.
- [189] S. X. Jia, L. L. Zhao, J. H. Yang, C. Zhang, and S. G. Wang. Stripping photo-resist with RF dielectric barrier atmospheric pressure plasma. *Applied Mechanics and Materials*, 260:114, 2013.

- [190] S. Wang, X. Xu, L. Zhao, and T. Ye. Photoresist etching by atmospheric pressure uniform-glow plasma. *Japanese Journal Of Applied Physics*, 46(8A):5294, 2007.
- [191] H. Chen, C. Weng, J.-D. Liao, K. Chen, and B. Hsu. Photo-resist stripping process using atmospheric micro-plasma system. *Journal of Physics D: Applied Physics*, 42(13):135201, 2009.
- [192] K. H. Han, J. G. Kang, H. S. Uhm, and B. K. Kang. Photo-resist ashing by atmospheric pressure glow discharge. *Current Applied Physics*, 7(2):211, 2007.
- [193] H. Yoshiki, K. Taniguchi, and Y. Horiike. Localized removal of a photoresist by atmospheric pressure micro-plasma jet using RF corona discharge. *Japanese Journal Of Applied Physics*, 41(Part 1, No. 9):5797, 2002.
- [194] K. Fricke, H. Steffen, T. von Woedtke, K. Schröder, and K.-D. Weltmann. High rate etching of polymers by means of an atmospheric pressure plasma jet. *Plasma Processes and Polymers*, 8(1):51, 2010.
- [195] J.-W. Lackmann, S. Schneider, E. Edengeiser, F. Jarzina, S. Brinckmann, E. Steinborn, M. Havenith, J. Benedikt, and J. E. Bandow. Photons and particles emitted from cold atmospheric-pressure plasma inactivate bacteria and biomolecules independently and synergistically. *Journal of The Royal Society Interface*, 10(89):20130591, 2013.
- [196] H. Bahre, H. Lange, V. Schulz-von der Gathen, and R. Foest. Vacuum ultraviolet (VUV) emission of an atmospheric pressure plasma jet (μ -APPJ) operated in helium-oxygen mixtures in ambient air. *Acta Technica*, 56:T199, 2011.
- [197] M. Madou. *Fundamentals of Microfabrication: The Science of Miniaturization*. Taylor & Francis, 2nd edition, 2002.
- [198] J. Metselaar, V. Kuznetsov, and A. Zhidkov. Photoresist stripping in afterglow of Ar-O₂ microwave plasma. *Journal of applied physics*, 75(10):4910, 1994.
- [199] J. Jeong, S. Babayan, A. Schutze, V. Tu, J. Park, I. Henins, G. Selwyn, and R. Hicks. Etching polyimide with a nonequilibrium atmospheric-pressure plasma jet. *Journal Of Vacuum Science & Technology A*, 17(5):2581, 1999.
- [200] N. Bibinov, N. Knake, H. Bahre, P. Awakowicz, and V. Schulz-von der Gathen. Spectroscopic characterization of an atmospheric pressure μ -jet plasma source. *Journal of Physics D: Applied Physics*, 44(34):345204, 2011.
- [201] H. M. Katsch, A. Tewes, E. Quandt, A. Goehlich, T. Kawetzki, and H. F. Döbele. Detection of atomic oxygen: Improvement of actinometry and comparison with laser spectroscopy. *Journal of Applied Physics*, 88(11):6232, 2000.